Institut für Theoretische Physik

Justus-Liebig-Universität Gießen

Zur Erlangung des Grades

eines Doktors der Naturwissenschaften

(Dr. rer. nat.)

vorgelegt von

M.Sc. Christopher Jung

Gießen, 2019

Spectral Functions of Vector Mesons from the Functional Renormalization Group

Referent: Prof. Dr. Lorenz von Smekal
Koreferent: Prof. Dr. Christian Fischer

Abstract

Understanding the phase structure of Quantum Chromodynamics (QCD) is still one of the major goals in the theoretical and experimental research of matter under extreme conditions. In this context, realistic spectral functions of vector and axial-vector mesons are crucial for identifying signatures of possible phase transitions and critical endpoints in the measured dilepton spectra.

In this thesis we calculate the spectral functions of the ρ and a_1 meson within the Functional Renormalization Group (FRG) approach by using a recently proposed analytic continuation procedure on the level of the flow equations. This is done by employing low-energy effective two-flavor models for QCD in different extensions in which we develop a new formalism to describe fluctuations due to massive (axial-)vector mesons within the FRG. In particular, we study in-medium modifications of these spectral functions in different regions of the phase diagram within the corresponding model where we focus on signatures for a chiral critical endpoint and the restoration of chiral symmetry. Additionally, we calculate temperature- and chemical-potential dependent electromagnetic spectral functions and present a new procedure of solving analytically continued flow equations self-consistently. The feasibility of this procedure is shown by calculating self-consistent spectral functions in the $O(4)$ model.

Zusammenfassung

Das Verständnis der Phasenstruktur der Quantenchromodynamik (QCD) ist immernoch eines der Hauptziele in der theoretischen und experimentellen Erforschung von Materie unter extremen Bedingungen. In diesem Zusammenhang sind realistische Spektralfunktionen von Vektor- und Axial-Vektormesonen entscheidend für das Identifizieren möglicher Phasenübergänge und kritischer Endpunkte in den gemessenen Dileptonspektren.

In dieser Arbeit berechnen wir die Spektralfunktionen des ρ und a_1 Mesons innerhalb der Funktionalen Renormierungsgruppe (FRG) mit Hilfe einer kürzlich vorgestellten Prozedur zur analytischen Fortsetzung auf Ebene der Flussgleichungen. Hierbei benutzen wir effektive Niederenergie-Modelle für Zwei-Flavor-QCD innerhalb verschiedener Erweiterungen, in welchen wir einen neuen Formalismus zur Beschreibung von Fluktuationen durch massive (Axial-)Vektormesonen innerhalb der FRG entwickeln. Insbesondere studieren wir mögliche Modifikationen in diesen Spektralfunktionen in verschiedenen Bereichen des Phasendiagramms für das entsprechende Modell, wobei wir unseren Fokus auf Signaturen für einen chiral-kritischen Endpunkt und die Wiederherstellung chiraler Symmetrie legen. Zusätzlich berechnen wir elektromagnetische Spektralfunktionen in Abhängigkeit von der Temperatur und dem chemischen Potential und präsentieren eine neue Prozedur, um analytisch fortgesetzte Flussgleichungen selbstkonsistent zu lösen. Die Machbarkeit dieser Prozedure wird anhand der Berechnung selbstkonsistenter Spektralfunktionen im $O(4)$ Modell gezeigt.

Contents

1 Introduction

With nowadays state of knowledge, nature can be described by three fundamental forces: the gravitational, the electroweak and the strong force. The latter two form the widely accepted Standard Model of particle physics where it is the strong force which is crucial for the description of matter under extreme conditions as observed in compact stellar objects or expected in the early universe microseconds after the Big Bang. Also the matter produced and studied in man-made relativistic heavy-ion collision experiments can be described by the strong interaction.

The quantum field theoretical description of the strong force is called *Quantum Chromodynamics* (QCD) and basically goes back to the 1950s and 1960s when it was Gell-Mann [1, 2] and Zweig [3] who proposed that baryons are bound states built out of three constituents, called *quarks*. In order to describe the entire observed hadron spectrum, e.g. the Δ^{++}, an additional quantum number was introduced, the *color charge* [4], according to which quarks appear in three different possible states. In analogy to quantum electrodynamics (QED), the interaction of quarks was then described within a $SU(3)$ gauge theory [5] where the associated gauge boson which mediates this interaction was called *gluon*. Since the $SU(3)$ gauge group is non-Abelian one direct consequence is that gluons also carry color charge and thus interact among themselves.

It is the variety of theoretical features and consequences that makes QCD fascinating and difficult to treat at the same time, from a theoretical as well as from an experimental point of view. Here, one of the main features is the absence of color charged objects in nature, called *confinement*. Consequently, quarks and gluons only appear as colorless bound states at low energies, like in form of mesons or baryons. The discovery of *asymptotic freedom* in 1973 by Gross, Wilczek [6] and Politzer [7] revealed the second main feature of QCD. According to that, the interaction strength of quarks and gluons becomes arbitrarily weak at high energies resulting in essentially free particles. The scale-dependence of the QCD coupling α_s reveals exactly these effects [8].

The understanding of a fundamental interaction also includes the knowledge of its

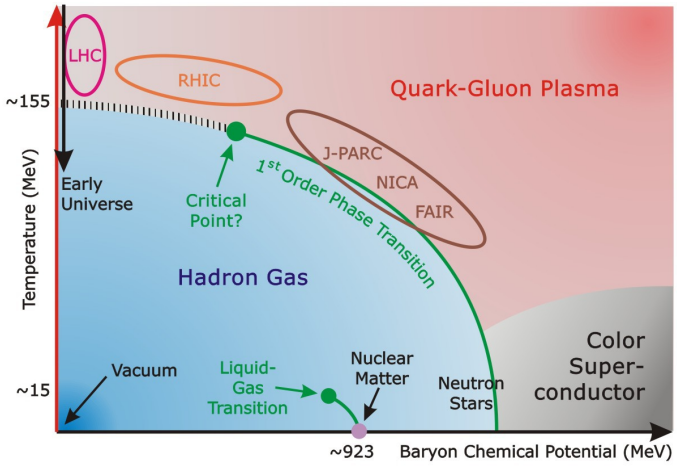

Figure 1.1: Phase diagram of QCD in the plane of temperature and chemical potential. Figure by courtesy of D. Rischke.

behaviour at finite temperature and density. For the strong interaction the different phases and properties expected from strong-interaction matter are usually illustrated as a function of temperature and chemical potential in the *QCD phase diagram*, a sketch of which is depicted in Fig. 1.1. Given its precise contours and features would allow to understand many phenomena like the evolution of the early Universe which would then correspond to trajectories through the phase diagram. Unfortunately, due to the infamous sign problem the applicability of the non-perturbative ab-initio approach of lattice QCD [9] is basically limited to the region of small chemical potentials [10,11]. Along the axis of vanishing chemical potential, lattice calculations show a crossover transition from a hadron gas to the quark-gluon plasma (QGP) phase with a crossover temperature of $T \approx 157$ MeV [12]. The hadronic phase is characterized by broken chiral symmetry and confined color states, whereas in the quark-gluon plasma phase quarks and gluons are deconfined and chiral symmetry is approximately restored in the light quark sector.

At intermediate and large densities various features and phases have been conjectured so far [13–15]. At vanishing temperature and intermediate densities we have the *liquid-gas* phase transition towards bound nuclear matter which represents a first-order phase transition that ends in a second-order critical point at a temperature of approximately 15 MeV. At larger densities the chiral crossover transition is expected to turn into a phase transition of first order where both transitions meet in a chiral critical endpoint (CEP). Currently, a lot of effort is put into finding experimental evidence of this predicted endpoint. In the vicinity of this first-order line there is also the conjecture of spatially modulated condensates, i.e. the existence of inhomogeneous phases [16]. At very large densities one expects more exotic features like color-superconducting phases characterized by Cooper pairing of quarks in analogy to ordinary superconductivity [17, 18].

As lattice QCD is not applicable in these regions, the detailed theoretical exploration of the QCD phase diagram at finite chemical potential requires different non-perturbative methods and a detailed understanding of the mechanisms of chiral

symmetry breaking and confinement. Here, very promising are functional methods such as *Dyson-Schwinger equations* (DSE) [19–25] or the *Functional Renormalization Group* (FRG) (see Chapter 2) which both are in principle applicable to the full QCD phase diagram. Since tackling full QCD is very complicated, one often uses effective models incorporating symmetries of QCD to get qualitative and also quantitative insights. Throughout this work we will employ the Functional Renormalization Group to mainly chiral symmetric two-flavor models for QCD (see Chapter 3).

The experimental investigation of the QCD phase diagram requires very high temperatures and/or densities and is therefore quite challenging. An overview of the most important heavy-ion collision experiments aiming to probe the phase diagram in specific regions is given in Fig. 1.1. Experiments at low densities and large temperatures are performed at the Lagre Hadron Colloder (LHC) at CERN and at the Relativistic Heavy Ion Collider (RHIC) at Brookhaven National Laboratory (BNL). Since in this region one has approximately the same number of particles and antiparticles, these experiments are relevant for studying the QCD epoch of the early Universe. Other experiments in the region at intermediate temperatures and large densities are performed at the Japan Proton Accelerator Research Complex (J-PARC), the Nuclotron-based Ion Collider fAcility (NICA) in Dubna and the Facility for Antiproton and Ion Research (FAIR) in Darmstadt. Here the questions of the existence and location of a possible chiral critical endpoint become relevant.

In such collision experiments, electromagnetic probes like lepton pairs are the ideal information carrier for the strong interaction as they escape the inner core of the collision process almost untouched once they are produced. In this context, it is the electromagnetic spectral function which links between the measured dilepton yields and the theoretical access to understand and interpret the physical mechanisms. Since vector mesons directly couple to these lepton pairs, the correct modelling of in-medium (axial-)vector meson spectral functions, primary of the ρ meson, is crucial for finding signatures for the restoration of chiral symmetry or a possible critical endpoint in the measured spectra (see Chapter 5 for a more detailed introduction on this topic).

The computation of real-time quantities like spectral functions or transport coefficients within Euclidean approaches to quantum field theory in general is very difficult since one somehow has to perform an analytic continuation from Euclidean space-time to the real-time framework. In practise, this analytic continuation procedure is usually performed numerically on the basis of numerical, Euclidean datasets using the maximum entropy method (MEM) [26–28], Padé approximants [29] or other numerical reconstruction methods [30]. As all these approaches rely to a high degree on the quality of the numerical input data, a non-perturbative framework to directly perform calculations in the real-time system would be very desirable. Here, the Functional Renormalization Group provides an alternative and very promising tool to carry out the analytic continuation in an analytic way without the necessity of numerical reconstruction methods [31–33]. The applicability of this method has been demonstrated in various recent studies [34–39], where mesonic and quark spectral functions were calculated within low-energy effective models, recently even self-consistently [40].

In this work, we follow the idea of these studies and aim at calculating ρ and a_1 meson spectral functions within effective low-energy models for QCD. Therefore we

derive and solve flow equations for retarded (axial-)vector meson two-point functions which are obtained by applying the FRG framework to an effective theory inspired by the gauged linear sigma model (gLSM) and an analytic continuation procedure on the level of the flow equations. Here we consider different model extensions and especially concentrate on the FRG formulation of fluctuations due to massive (axial-)vector mesons. The related issue of defining covariant time-ordered products for vector or in general tensor fields is known for a long time already and will be resolved as part of the used effective theory by implementing the Stueckelberg formalism for massive vector mesons. This ansatz is modelled in a way that at the physical IR scale the associated modified Ward identity (mWI) is fulfilled and we end up with a manifestly covariant and transverse vector meson Green function. In order to investigate possible signatures for the restoration of chiral symmetry or a chiral critical endpoint, we study the resulting ρ and a_1 meson spectral functions as well as electromagnetic spectral functions at finite temperature and finite chemical potential along the phase diagram of the corresponding effective model.

In an additional study, we present a numerical procedure of solving analytic continued flow equations self-consistently, even at finite temperature. This represents an important technical step to resolve non-trivial structures in spectral functions since in the usual truncation only the single-particle contributions of the particular propagators contribute to the flow equations. To demonstrate the applicability of this procedure we calculate the pion and sigma spectral functions in the $O(4)$ model.

This thesis is organized as follows. In Chapter 2 we start by introducing the Functional Renormalization Group as a non-perturbative method. Beginning with a recapitulation of generating functionals and the derivation of the Wetterich equation, we will concentrate on flow equations for two-point functions including their analytic continuation to real energies. We will also discuss numerical procedures of solving flow equations. Basics of QCD and the quark-meson model as well as the parity-doublet model as effective low-energy models will be discussed and introduced in Chapter 3. Here we already present first results on the phase structure of these models. In Chapter 4 we will then focus on the theoretical description of (axial-)vector mesons by fundamental fields within effective theories and possible extensions. After a glimpse on the historic development we will introduce the gauged linear sigma model with quarks where in particular we will discuss its treatment within the FRG including the FRG formulation of fluctuating (axial-)vector mesons. Results for temperature- and chemical-potential dependent ρ and a_1 meson spectral functions as well as for electromagnetic spectral functions obtained within different model settings will be presented and discussed in Chapter 5. In Chapter 6 we then introduce a numercial procedure for calculating spectral functions self-consistently. As an example we will present results for mesonic spectral functions within the $O(4)$ model. We close this thesis by giving a summary and an outlook in Chapter 7. The used notations and conventions are listed in App. A. In App. B we give further details on the derivation of flow equations including explicit expressions. Finally, in App. C we discuss further important properties of retarded two-point functions and spectral functions.

As supplemental material we submit Mathematica notebooks in which all objects and equations used within this dissertation are listed.

While all results presented in this thesis are the original work of the author, most of the results were achieved in collaboration with other authors. Results for (axial-)vector meson spectral functions in Sec. 5.2.1 were obtained in collaboration with Fabian Rennecke, Ralf-Arno Tripolt, Lorenz von Smekal and Jochen Wambach, published in [41, 42]. Results for the parity-doublet model in Chapter 3, the formalism of fluctuating (axial-)vector mesons in Sec. 4.2.2 as well as spectral functions presented in Sec. 5.2.2 and Sec. 5.2.3 were obtained in collaboration with Lorenz von Smekal, results for electromagnetic spectral functions in Sec. 5.3 together with Ralf-Arno Tripolt, Naoto Tanji, Lorenz von Smekal and Jochen Wambach, published in [43]. Finally, Chapter 6 is based on the collaboration with Nils Strodhoff and Lorenz von Smekal.

2

The Functional Renormalization Group

The Functional Renormalization Group (FRG) provides a powerful tool addressing in particular non-perturbative effects in statistical physics and quantum field theory, see [31,44–50] for general reviews. The basic aim in this framework is to understand and calculate macroscopic properties of physical systems from a given microscopic theory where the applicability ranges from condensed matter physics [51] and quantum gravity [52–56] to QCD [57–60].

As central object, Wetterich, the pioneer of this approach, introduced the so-called *effective average action* Γ_k as generalization of the quantum effective action Γ [61]. With the introduction of the scale parameter k, this effective average action Γ_k interpolates between a chosen bare classical action $S_{\rm cl} \equiv \Gamma_\Lambda$ given at a cutoff scale Λ and the full quantum effective action $\Gamma \equiv \Gamma_{k\to 0}$ where all quantum and thermal fluctuations are included. Technically this procedure follows the Wilsonian approach to renormalization where quantum effects are included by integrating out fluctuations momentum-shell by momentum-shell. This is achieved by introducing the so-called *regulator function* R_k which suppresses low-momentum fluctuations such that Γ_k only includes fluctuations with momenta larger than k.

The change of Γ_k when changing the scale k is described by the *Wetterich equation*, an exact flow equation which, together with the specification of the bare action at the UV scale, can be used as definition of a quantum field theory. Since this equation cannot be solved analytically in a closed form, one has to use truncations to approximate the full solution numerically. Here, one advantage of the FRG framework is the versatility of truncation schemes which can be constructed in a systematic way guided by the concrete physical setup and the numerical stability.

We start this chapter by recapitulating the concept of generating functionals in quantum field theory and by deriving the Wetterich equation in Sec. 2.1. In Sec. 2.2 we will focus on two-point functions where we first discuss the Euclidean flow and afterwards present the analytic continuation procedure towards flow equations for retarded two-point functions. We close this chapter by discussing the numercial procedure for solving flow equations including possible truncation schemes in Sec. 2.3.

2.1 The Effective Average Action

2.1.1 Generating Functionals and Statistical Physics

We start this section by recapitulating the concept of generating functionals in Euclidean quantum field theory, for simplicity we only consider a real scalar field theory [46].

An efficient way of storing all information about a given quantum field theory is to calculate the generating functional of all correlation functions

$$Z[J] = \int \mathcal{D}\varphi \; \mathrm{e}^{-S[\varphi]+\int J\varphi} \,, \tag{2.1}$$

with $S[\varphi]$ being the classical action and J a so-called *source term*. The integral is performed over all field configurations. By functional differentiation with respect to the source term one has access to all correlation functions which are then defined as

$$\langle \varphi(x_1) \dots \varphi(x_n) \rangle = \frac{1}{Z[J=0]} \left. \frac{\delta^n Z[J]}{\delta J(x_1) \dots \delta J(x_n)} \right|_{J=0} . \tag{2.2}$$

In order to get rid of the disconnected Feynman diagrams one introduces the so-called *Schwinger functional* $W[J]$ which is the generating functional providing all connected Feynman diagrams, given by the logarithm of $Z[J]$,

$$W[J] = \ln Z[J] = \ln \left(\int \mathcal{D}\varphi \; \mathrm{e}^{-S[\varphi]+\int J\varphi} \right) . \tag{2.3}$$

An even more suited way of encoding the same information is to perform a Legendre transformation of the Schwinger functional which is then called *effective action* Γ, generating only one-particle irreducible Feynman diagrams,

$$\Gamma[\phi] = \int_x J\phi - W[J] \,, \tag{2.4}$$

where ϕ now represents the classical field given by the field-expectation value in the presence of a source term,

$$\phi(x) = \langle \varphi(x) \rangle_J = \frac{\delta W}{\delta J} \,. \tag{2.5}$$

The strength of a description in terms of generating functionals is the apparent analogy to statistical physics [62]. In this analogy, the generating functional $Z[J]$ plays the role of the partition function describing a macroscopic system in statistical mechanics, the Schwinger functional $W[J]$ corresponds to the Helmholtz free energy. The effective action as Legendre transform of $W[J]$ can finally be identified with the Gibbs free energy. Evaluating the effective action at a constant field ϕ_{const} (independent of x) and using that Γ is an extensive quantity in a thermodynamic sense gives

$$\Gamma[\phi_{\text{const}}] = \mathcal{U} \cdot U_{\text{eff}}(\phi_{\text{const}}) \,. \tag{2.6}$$

The effective action is up to a volume factor $\mathcal{U}$ proportional to the so-called *effective potential* U_{eff}. Evaluated at its minimum, U_{eff} can in the language of statistical mechanics be identified with the grand potential per volume sometimes also called the Landau free-energy density. From this, many thermodynamic quantities of the theory like pressure, entropy density or particle densities can be read off.

2.1.2 The Wetterich Equation

The basic objects of the FRG are the effective average action Γ_k as generalization of the effective action introduced in the last section, Sec. 2.1.1, and its exact flow equation, the Wetterich equation which will be derived in the following. For clarity and simplicity we make this discussion with real, scalar bosonic fields, the generalization to general (non-scalar) bosonic and fermionic fields is in principle straightforward and will be addressed at the end of this section. As a last remark, from now on the trace is always meant to be a trace over all internal indices together with an integration over the internal momentum.

In order to construct Γ_k one first requires that at the UV cutoff scale $k = \Lambda$ it corresponds to the bare classical action and at the IR scale $k \to 0$ one recovers the full quantum effective action,

$$\Gamma_{k=\Lambda} = S_{cl}\,, \qquad\qquad \Gamma_{k\to 0} = \Gamma\,. \tag{2.7}$$

Technically this can be achieved by inserting a k-dependent term into the definition of the generating functionals,

$$Z_k[J] = \mathrm{e}^{W_k[J]} \equiv \int \mathcal{D}\varphi\, \exp\left(-S[\varphi] - \Delta S_k[\varphi] + \int J\varphi\right), \tag{2.8}$$

where the extra IR cutoff term is quadratic in the field and can be interpreted as momentum and k-dependent mass term, more explicitly given as

$$\Delta S_k[\varphi] = \frac{1}{2}\int \frac{d^D q}{(2\pi)^D}\, \varphi(-q) R_k(q) \varphi(q)\,. \tag{2.9}$$

The regulator function $R_k(q)$, which in general is matrix-valued, can in principle be chosen arbitrarily but has to obey the following three properties such that the requirements in Eq. (2.7) are fulfilled:

1. For $q^2/k^2 \to 0$ the regulator stays finite, implementing an IR regularization.
2. For $k^2/q^2 \to 0$ the regulator vanishes such that for $k \to 0$ one recovers the full quantum effective action Γ.
3. For $k \to \Lambda \to \infty$ the regulator diverges. In this case one can use the saddle-point approximation and Γ_k reduces to the classical action S_{cl}.

Typical regulators fulfilling these requirements are exponential ones or the one proposed by Litim [63] called *Litim regulator*,

$$R_k^{\mathrm{Exp}}(q) \sim \frac{q^2}{\exp q^2/k^2 - 1}\,, \qquad R_k^{\mathrm{Litim}}(q) \sim (k^2 - q^2)\,\Theta(k^2 - q^2)\,. \tag{2.10}$$

In Fig. 2.1 it is illustrated how the regulator and its derivative implement the properties discussed above.

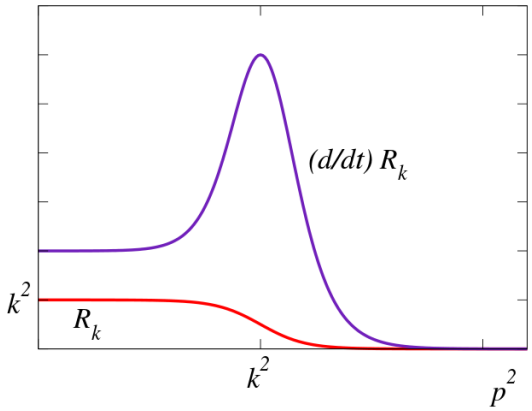

Figure 2.1: Plot of a typical regulator function R_k serving as additional mass for fluctuations with momentum smaller than k, and of the peaked regulator derivative $\partial_t R_k = k\partial_k R_k$ implementing the momentum-shell integration (from [64]).

We can now study the k-trajectory of the generating functionals. For the modified Schwinger functional $W_k[J]$ we obtain

$$\begin{aligned}\partial_k W_k[J] &= -\frac{1}{Z_k[J]} \int \mathcal{D}\varphi \; (\partial_k \Delta S_k[\varphi]) \exp\left(-S[\varphi] - \Delta S_k[\varphi] + \int J\varphi\right) \\ &= -\left\langle \partial_k \Delta S_k[\varphi] \right\rangle_J \\ &= -\left\langle \frac{1}{2} \int \frac{d^D q}{(2\pi)^D} \varphi(-q) \partial_k R_k(q) \varphi(q) \right\rangle_J , \end{aligned} \tag{2.11}$$

where the expectation value of a functional $A[\varphi]$ in the presence of a source term J is defined by

$$\left\langle A[\varphi] \right\rangle_J = \frac{1}{Z[J]} \mathrm{Tr}(A[\varphi]\, Z[J]) \,. \tag{2.12}$$

With the definition of the connected propagator

$$\begin{aligned} G_k(p) \equiv \left(\frac{\delta^2 W_k}{\delta J \delta J}\right)(p) &= \left\langle \varphi(-p)\varphi(p) \right\rangle_J - \left\langle \varphi(-p) \right\rangle_J \left\langle \varphi(p) \right\rangle_J \\ &\overset{(2.5)}{=} \left\langle \varphi(-p)\varphi(p) \right\rangle_J - \phi(-p)\phi(p) \,, \end{aligned} \tag{2.13}$$

we can express Eq. (2.11) in terms of this propagator which leads to

$$\begin{aligned}\partial_k W_k[J] &= -\frac{1}{2} \int \frac{d^D q}{(2\pi)^D} \left(\partial_k R_k(q) G_k(q) + \phi(-q) \partial_k R_k \phi(q)\right) \\ &= -\frac{1}{2} \int \frac{d^D q}{(2\pi)^D} \left(\partial_k R_k(q) G_k(q) + \partial_k \Delta S_k[\phi]\right) \,. \end{aligned} \tag{2.14}$$

At this point we come back to the scale-dependent version of the effective action, defined via a modified Legendre transformation

$$\Gamma_k[\phi] = \int_x J\phi - W_k[J] - \Delta S_k[\phi]\,. \tag{2.15}$$

From the functional derivative of Γ_k with respect to the field

$$\frac{\delta\Gamma_k[\phi]}{\delta\phi(x)} = J(x) - (R_k\phi)(x)\,, \tag{2.16}$$

the functional derivative of the source is obtained by

$$\frac{\delta J(x)}{\delta\phi(y)} = \frac{\delta^2\Gamma_k[\phi]}{\delta\phi(y)\delta\phi(x)} + R_k(x,y) = \left(\Gamma_k^{(2)}[\phi] + R_k\right)(x,y)\,. \tag{2.17}$$

Here we introduced the notation for the scale-dependent 1PI n-point functions,

$$\Gamma_k^{(n)}(x_1\dots x_n) \equiv \frac{\delta^n\Gamma_k[\phi]}{\delta\phi(x_n)\dots\delta\phi(x_1)}\,. \tag{2.18}$$

Performing the functional derivative of the field with respect to the source and exploiting Eq. (2.5) yields

$$\frac{\delta\phi(x)}{\delta J(y)} = \frac{\delta^2 W_k[J]}{\delta J(y)\delta J(x)} = G_k(x-y')\,, \tag{2.19}$$

which is the above defined connected propagator in position space. Finally we can compare Eq. (2.17) and Eq. (2.19) to find the following,

$$\begin{aligned}\delta(x-y) = \frac{\delta J(x)}{\delta J(y)} &= \int d^Dx'\,\frac{\delta J(x)}{\delta\phi(x')}\frac{\delta\phi(x')}{\delta J(y)} \\ &= \int d^Dx'\,(\Gamma_k^{(2)}[\phi] + R_k)(x,x')\,G_k(x'-y) \qquad (2.20)\\ \Rightarrow G_k^{-1} &= (\Gamma_k^{(2)}[\phi] + R_k)\,. \qquad (2.21)\end{aligned}$$

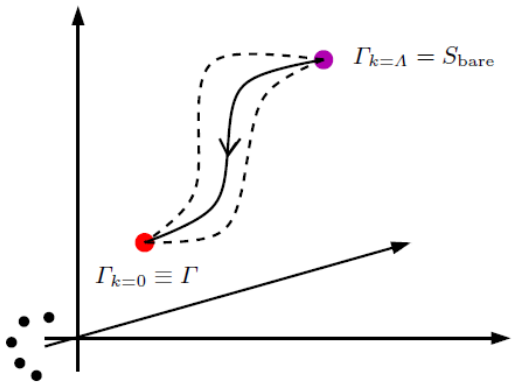

Figure 2.2: Schematic plot of the flow of the effective average action in theory space. After specifying the initial form of Γ_Λ, the resulting effective action Γ is unique whereas the precise k-trajectory depends on the choice of the regulator R_k (from [64]).

The inverse of the k-dependent propagator G_k is just given as the sum of the two-point function $\Gamma_k^{(2)}$ and the regulator function R_k.

We can now put all considerations together to finally obtain the flow equation for the effective average action,

$$\begin{aligned}\partial_k\Gamma_k[\phi] &= \int_x (\partial_k J)\phi - \partial_k W_k[J] - \partial_k \Delta S_k[\phi] \\ &= -\partial_k W_k[J] - \partial_k \Delta S_k[\phi] \\ &\overset{(2.14)}{=} \frac{1}{2}\int \frac{d^D q}{(2\pi)^D}\,\partial_k R_k(q)\,G_k(q) \\ &\overset{(2.21)}{=} \frac{1}{2}\,\mathrm{Tr}\left[\partial_k R_k\left(\Gamma_k^{(2)}[\phi] + R_k\right)^{-1}\right]. \end{aligned} \tag{2.22}$$

A schematic plot of the flow of Γ_k described by Eq. (2.22) is illustrated in Fig. 2.2. In general, the field $\phi(q)$ represents bosonic and fermionic Grassmann valued fields with arbitrary substructures, generically indicated by $\phi(q) = \left(B(q), F(q), \bar{F}(-q)\right)^\top$. The corresponding two-point function and regulator in field space then look like

$$\Gamma_k^{(2)}(q,p) = \begin{pmatrix} \Gamma^{(2)}_{k,BB} & 0 & 0 \\ 0 & 0 & \Gamma^{(2)}_{k,F\bar{F}} \\ 0 & \Gamma^{(2)}_{k,\bar{F}F} & 0 \end{pmatrix}, R_k(q) = \begin{pmatrix} R_{k,BB}(q) & 0 & 0 \\ 0 & 0 & R_{k,F\bar{F}}(q) \\ 0 & R_{k,\bar{F}F}(q) & 0 \end{pmatrix}.$$

Since the bosonic and the fermionic elements do not mix, the Wetterich equation, Eq. (2.22), decomposes into a bosonic and a fermionic part. With the relation $\Gamma^{(2)}_{k,F\bar{F}} = -(\Gamma^{(2)}_{k,\bar{F}F})^\top$ we can rewrite Eq. (2.22) as

$$\begin{aligned}\partial_k\Gamma_k &= \frac{1}{2}\,\mathrm{Tr}\left[\partial_k R_{k,B}\left(\Gamma^{(2)}_{k,B} + R_{k,B}\right)^{-1}\right] - \mathrm{Tr}\left[\partial_k R_{k,F}\left(\Gamma^{(2)}_{k,F} + R_{k,F}\right)^{-1}\right] \\ &= \frac{1}{2}\,\mathrm{STr}\left[\partial_k R_k\left(\Gamma^{(2)}_k + R_k\right)^{-1}\right]. \end{aligned} \tag{2.23}$$

Here one sometimes uses the notation STr which means a trace together with the fermion factor -2. The usual diagrammatic representation of this equation is shown in Fig. 2.3. Formally this equation has a one-loop structure but it is an exact equation with fully dressed propagators in the loops.

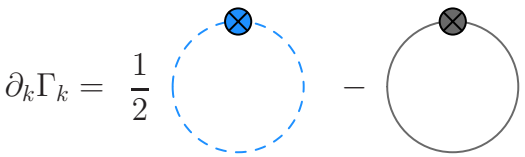

Figure 2.3: Diagrammatic form of the flow equation for the effective average action, Eq. (2.23). The dashed blue line is associated with bosonic propagators, the solid black line with fermionic propagators, the crossed circles represent regulator insertions $\partial_k R_k$.

2.2 Flow Equations for Two-Point Functions

2.2.1 Euclidean Flow and Particle Masses

As already mentioned, all information about a quantum field theory is encoded in the effective action Γ or equivalently in its functional derivatives, the n-point vertex functions $\Gamma^{(n)}$. Flow equations for these n-point functions can be derived by taking n functional derivatives of the Wetterich equation, Eq. (2.23), with respect to specific fields. As our main goal is to compute spectral functions we will in the following focus on flow equations for two-point functions.

Taking two functional derivatives of the Wetterich equation with respect to the fields ϕ_i and ϕ_j we find the following general structure,

$$\begin{aligned}\frac{\delta^2}{\delta\phi_i(-p)\delta\phi_j(p)}\partial_k\Gamma_k[\phi] &\equiv \partial_k\Gamma^{(2)}_{\phi_i\phi_j,k}(p)\\ &= \mathrm{STr}\left\{D_{ab,k}(q)\,\Gamma^{(3)}_{bci,k}(p,q)\,D_{cd,k}(q\pm p)\,\Gamma^{(3)}_{dej,k}(p,q)\,D_{ef,k}(q)\right\}\\ &\quad -\frac{1}{2}\mathrm{STr}\left\{D_{ab,k}(q)\,\Gamma^{(4)}_{bcji,k}(q)\,D_{cd,k}(q)\right\}. \end{aligned} \tag{2.24}$$

In this expression we applied momentum conservation such that $\Gamma^{(3)}_k$ and $\Gamma^{(4)}_k$ only depend on the loop momentum q and on the in- (and out-) going momentum p, the momentum-dependent contribution is meant to be symmetrized in $\pm p$. Furthermore, we used collection indices for particle species and internal structures like color or isospin. The scale-dependent regulated Euclidean propagator in general is defined by

$$D_{k,ij}(q) \equiv \left(\Gamma^{(2)}_k(q) + R_k(q)\right)^{-1}_{ij}. \tag{2.25}$$

The structure of Eq. (2.24) is shown in the usual diagrammatic form in Fig. 2.4. The explicit form of the involved objects depends on the employed model, see App. B for explicit expressions used in this work.

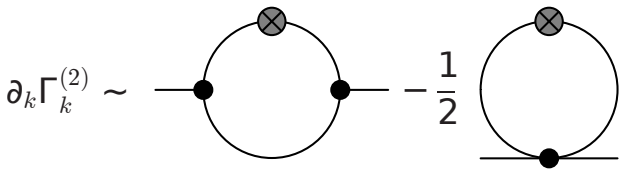

Figure 2.4: Diagrammatic form of the structure of flow equations for two-point functions. The left momentum-dependent loop involves three propagators (solid internal lines) and two three-point vertices (black dots). The right momentum-independent tadpole involves two propagators and one four-point vertex.

Euclidean masses and pole masses

From the Euclidean two-point function we can straightforwardly define the Euclidean (curvature) mass as the momentum independent part of it, evaluated at the physical point in field space $\phi = \phi_0$,

$$(m_k^2)^E \equiv \Gamma_k^{(2),E}(p = 0; \phi = \phi_0)\,. \tag{2.26}$$

This is the only mass definition which is accessible within the Euclidean framework and can be seen as physical model-parameter rather than as physical mass. In a simple $O(4)$ symmetric model we have for example,

$$m_{\pi,k}^2 = \Gamma_{k,\pi\pi}^{(2),E}(0) = 2\,U_k'\,, \tag{2.27}$$

$$m_{\sigma,k}^2 = \Gamma_{k,\sigma\sigma}^{(2),E}(0) = 2\,U_k' + 4\,\phi^2\,U_k''\,, \tag{2.28}$$

with U_k' and U_k'' being derivatives of the effective potential with respect to ϕ^2. This relation of the zero-momentum limit of the Euclidean two-point functions to field-derivatives of the effective potential is a non-trivial statement following from our truncation scheme and reflects the thermodynamic consistency of the used ansatz, cf. Sec. 2.3.1.

The *pole mass* as physical mass is defined as the zero of the analytically continued two-point function,

$$\Gamma_k^{(2),E}(\mathrm{i}m^p, \vec{p} = 0) \equiv 0\,. \tag{2.29}$$

While for stable particles this zero is located on the Minkowski axis corresponding to a real mass m^p, for resonances it lies on the unphysical or second Riemann sheet and is consequently in general complex-valued.

Throughout this work we define the pole mass as zero crossing of the real part of the retarded two-point function $\Gamma_k^{(2),\mathrm{R}}$, which for stable particles agrees with the physical pole mass and for unstable particles is a good approximation if the width of the resonance, i.e. the imaginary part of $\Gamma_k^{(2),\mathrm{R}}$, is sufficiently small. In this case the pole mass locates the position of the peak of the resonance, at least approximately, whose width is given by the imaginary part of the zero of the retarded two-point function $\Gamma_k^{(2),\mathrm{R}}$ on the second Riemann sheet.

2.2.2 Analytic Continuation of Flow Equations

To extract physically valuable information like pole masses, decay widths or in general real-time observables like spectral functions and transport coefficients from the Euclidean FRG framework one has to perform an analytic continuation to Minkowski space-time. This analytic continuation is a very general problem in mathematics and theoretical physics and describes in its very general definition the extension of some holomorphic function to a larger subset in the following way [65].

Let U and V be two open, arcwise connected sets in the complex plane with $U \subset V$ and $f : U \to \mathbb{C}$, $F : V \to \mathbb{C}$ being holomorphic functions. If $f(z) = F(z)\ \forall z \in U$ then F is called *analytic continuation* of f and is uniquely defined.

In Euclidean approaches to quantum field theory one usually computes Euclidean correlators on discrete, imaginary Euclidean frequencies $\mathrm{i}p_{0,n}$. In this case, an analytic continuation is in general not well defined since one only knows the function at discrete points and the function usually is not unique such that there seem to be infinite possibilities for a continuation. However, if the function is analytic off the real axis and goes to zero if the argument approaches infinity it can be shown that there exists a well-defined, unique analytic continuation (Baym-Mermin boundary conditions) [66]. In practical calculations one usually performs this analytic continuation procedure towards real frequencies numerically, for example with the maximum entropy method (MEM) [26–28] or Padé approximants [29].

In the FRG framework, however, it is possible to perform this analytic continuation procedure with the correct boundary conditions analytically, on the level of the flow equations. In the present case we want to allow the Euclidean two-point function $\Gamma^{(2),E}(\mathrm{i}p_{0,n})$ to be evaluated at real continuous frequencies ω in order to obtain the retarded two-point function in Minkowski space-time, $\Gamma^{(2),R}(\omega)$. Here we can use the simple one-loop structure of the FRG flow equations and let us guide by finite temperature perturbation theory where this can be done well-defined and on the level of the equations [67]. Transferred to FRG flow equations for two-point functions these steps read [33, 34]:

1. Exploit the periodicity of bosonic and fermionic occupation numbers with respect to external imaginary bosonic or fermionic Matsubara frequencies,

$$n_B(E \pm \mathrm{i}p_{0,n}) \to n_B(E)\,, \qquad n_F(E \pm \mathrm{i}p_{0,n}) \to n_F(E)\,. \tag{2.30}$$

2. Replace the discrete Euclidean frequency by a real, continuous frequency ω,

$$\partial_k \Gamma_k^{(2),R}(\omega, \vec{p}) = -\lim_{\epsilon \to 0} \partial_k \Gamma_k^{(2),E}(p_0 = -\mathrm{i}(\omega + \mathrm{i}\epsilon), \vec{p})\,. \tag{2.31}$$

In this way we obtain flow equations for retarded two-point functions out of the corresponding Euclidean ones discussed in Sec. 2.2.1. For the retarded propagator $D^{\mathrm{R}}(\omega)$ given as the inverse of the retarded two-point function one can then define the so-called *spectral density* or *spectral function* $\rho(\omega, \vec{p})$ as imaginary part of it [68],

$$\rho(\omega, \vec{p}) = -\frac{1}{\pi} \operatorname{Im} D^{\mathrm{R}}(\omega, \vec{p})\,, \tag{2.32}$$

or equivalently in terms of the real and imaginary part of the retarded two-point function,

$$\rho(\omega, \vec{p}) = \frac{1}{\pi} \frac{\operatorname{Im} \Gamma^{(2),\mathrm{R}}(\omega, \vec{p})}{\left(\operatorname{Re} \Gamma^{(2),\mathrm{R}}(\omega, \vec{p})\right)^2 + \left(\operatorname{Im} \Gamma^{(2),\mathrm{R}}(\omega, \vec{p})\right)^2}\,. \tag{2.33}$$

This spectral function will be the basic object in this work. It contains the whole spectrum of a given theory including information like pole masses, decay widths and possible decay channels and is therefore important for the calculation of various observables like the shear-viscosity or other transport coefficients [69, 70]. Using

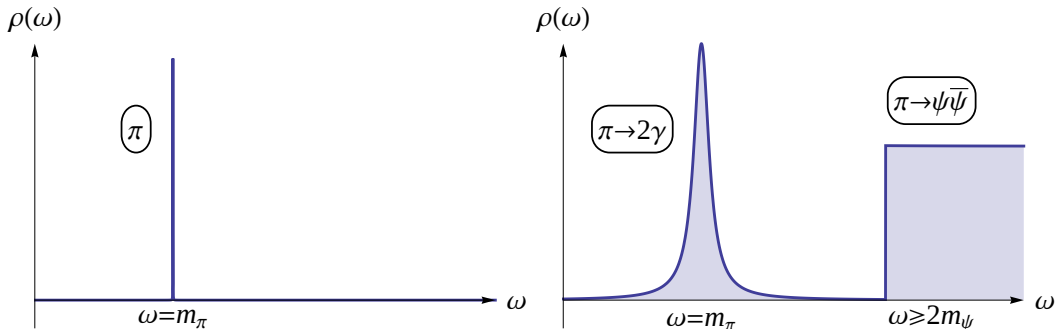

Figure 2.5: Schematic spectral functions of a neutral pion: The spectral function of a stable pion is given by a delta function concentrated at the pole mass (left). For unstable pions the sharp delta peak gets a finite width and height (right). Possible decays in other particles give rise to contributions at larger frequencies.

the *Lehmann spectral representation* one also has access to all types of propagators (retarded, advanced and Euclidean),

$$D^R(\omega,\vec{p}) = -\int_{-\infty}^{\infty} \frac{d\omega'}{\omega'-\omega-\mathrm{i}\epsilon}\,\rho(\omega',\vec{p})\,, \tag{2.34}$$

$$D^A(\omega,\vec{p}) = -\int_{-\infty}^{\infty} \frac{d\omega'}{\omega'-\omega+\mathrm{i}\epsilon}\,\rho(\omega',\vec{p})\,, \tag{2.35}$$

$$D^E(p_0,\vec{p}) = \int_{-\infty}^{\infty} \frac{d\omega'}{\omega'+\mathrm{i}p_0}\,\rho(\omega',\vec{k})\,. \tag{2.36}$$

The spectral function has some important properties. It is antisymmetric in ω and symmetric in $\vec{p}$,

$$\rho(\omega,-\vec{p}) = \rho(\omega,\vec{p})\,, \qquad \rho(-\omega,\vec{p}) = -\rho(\omega,\vec{p})\,, \tag{2.37}$$

for physical particles it obeys the positivity condition

$$\mathrm{sgn}(\omega)\,\rho(\omega,\vec{p}) \geq 0\,, \tag{2.38}$$

and it is normalized to one

$$\int_{-\infty}^{\infty} d\omega'\;\omega'\,\rho(\omega',\vec{p}) = 1\,. \tag{2.39}$$

In Fig. 2.5 a schematic representation of typical spectral functions is depicted. While in a free theory the total spectral weight is concentrated on the pole mass of the particle (left picture), interactions can modify the shape, leaving the integrated weight constant (right picture). The spectral function of a free particle is thus given by a delta peak concentrated on the pole mass of the particle,

$$\rho(\omega,\vec{p}) = \mathrm{sgn}(\omega)\,Z\,\delta(\omega^2-\vec{p}^{\,2}-m^2)\,, \tag{2.40}$$

with wavefunction renormalization Z. While in a free theory we have $Z=1$, interactions lead to a decrease of Z in favor of additional terms in the spectral function, for example decay thresholds, which then receive fractions of the total spectral weight.

2.3 Truncation Schemes and Numerics

2.3.1 The Derivative Expansion

In practice, the flow equation for the effective average action Eq. (2.23) and its functional derivatives Eq. (2.24) can neither be solved analytically nor numerically in a closed form. In the following we will discuss truncation schemes and numerical methods towards an approximate solution. The first step is to make an ansatz for the structure of the effective average action Γ_k. Here, one possibility is an expansion in terms of 1PI vertex functions $\Gamma^{(n)}$, the so-called *vertex expansion*,

$$\Gamma_k[\phi] = \sum_{n=0}^{\infty} \frac{1}{n!} \int d^D x_1 \dots d^D x_n \, \Gamma_k^{(n)}(x_1, \dots, x_n) \, \phi(x_1) \dots \phi(x_n) \,. \tag{2.41}$$

Inserting this ansatz into the Wetterich equation, Eq. (2.23), one obtains flow equations for the vertex functions $\Gamma_k^{(n)}$ resulting in an infinite tower of equations which thus has to be truncated at finite order. This scheme is used for example in [71, 72], where an error estimate is possible by increasing the expansion order and look for apparent convergence.

Another systematic truncation scheme is the so-called *derivative expansion* as expansion in powers of derivatives or momenta in momentum space. For a scalar field ϕ this ansatz has the form

$$\Gamma_k[\phi] = \int d^D x \left\{ U_k(\phi) + \frac{1}{2} Z_k(\phi) \, (\partial_\mu \phi)^2 + \frac{1}{8} Y_k(\phi) \left(\partial_\mu \phi^2 \right)^2 + \mathcal{O}(\partial^4) \right\} . \tag{2.42}$$

To lowest order of this ansatz, which is referred to as *local potential approximation* (LPA), only the scale-dependent effective potential U_k and the kinetic term is taken into account while the wave function renormalization Z_k is set to one and Y_k is set to zero. An extension of this simple truncation, for example by including field independent Z_k's to dress the momentum dependent part, is called LPA$'$ in the literature. The derivative expansion is suitable for describing critical phenomena as usually the order parameters explicitly show up as variables. Considering the $O(n)$ model for example, already the LPA ansatz gives rather accurate results e.g. for critical exponents [73]. Via model extensions towards the quark-meson model, this LPA ansatz also provides first qualitative insights into the phase structure of QCD [74, 75]. For this reason we will mainly use the LPA approximation in this work.

Using the derivative expansion also results in an infinite tower of equations since in the flow equation for $\Gamma_k^{(n)}$ there always appear vertices up to $\Gamma_k^{(n+2)}$. In order to render this system of equations finite we will extract the k-dependent two-point functions $\Gamma_k^{(2)}$ as well as the vertex functions $\Gamma_k^{(3)}$ and $\Gamma_k^{(4)}$ from the LPA ansatz in Eq. (2.42) which gives a closed system of equations. More involved truncation schemes are the expansion of vertex functions in external momenta [76, 77] or back-coupled self-consistent solutions of Euclidean flow equations [78] and of analytic continued flow equations towards the computation of self-consistent spectral functions [40]. Here we refer to Chapter 6 where we come back to this issue and present an alternative framework to calculate self-consistent spectral functions at finite temperature.

2.3.2 Numerical Procedure

With a given ansatz for the effective average action, the Wetterich equation provides a set of complicated, coupled differential equations which cannot be solved analytically and hence requires numerical methods. Inserting the LPA ansatz for the effective average action into the Wetterich equation gives a partial differential equation for the effective potential as it depends on the momentum scale k, the field invariant $\phi^2 \equiv \rho$ and respective derivatives of the effective potential with respect to ρ,

$$\partial_k U_k(\rho) = \text{Flow}\left[k, \rho, U_k'(\rho), U_k''(\rho)\right] . \tag{2.43}$$

In the following we present two common techniques in order to solve these types of equations, namely via a Taylor expansion or with the so-called *grid method*.

Taylor expansion

One possibility of solving Eq. (2.43) is to first make a Taylor expansion of the effective potential in powers of the invariant ρ around an, in general k-dependent, expansion point $\bar{\rho}_k$ up to order N,

$$U_k(\rho) = \sum_{n=0}^{N} \frac{\lambda_{k,n}}{n!} (\rho - \bar{\rho}_k)^n , \tag{2.44}$$

with scale-dependent expansion coefficients $\lambda_{k,n}$. With the constraint that the expansion point $\bar{\rho}_k$ is the physical minimum, defined via

$$\frac{\partial}{\partial \phi} \left(U_k(\rho) - c\sigma\right)\Big|_{\rho=\bar{\rho}_k} \stackrel{!}{=} 0 , \tag{2.45}$$

we find for the first expansion coefficient $\lambda_{1,k} = c/(2\,\bar{\rho}_k^{1/2})$. Here $c\sigma$ accounts for the explicit symmetry breaking in the case of a scalar field in the $O(4)$ notation $\phi = (\sigma, \vec{\pi})^\top$. We now can make an expansion also for the flow of U_k in the same manner,

$$\partial_k U_k(\rho) = \sum_{n=0}^{N} \frac{\partial_k U_k^{(n)}(\bar{\rho}_k)}{n!} (\rho - \bar{\rho}_k)^n , \tag{2.46}$$

and insert the ansatz from Eq. (2.44) to obtain flow equations for the expansion coefficients $\lambda_{k,n}$, given by

$$\partial_k \lambda_{n,k} = \partial_k U_k^{(n)}(\bar{\rho}_k) + \lambda_{n+1,k}\, \partial_k \bar{\rho}_k . \tag{2.47}$$

In this expression, $\partial_k U^{(n)}(\bar{\rho}_k)$ denotes the n-th derivative of the Wetterich equation with respect to ρ evaluated at $\bar{\rho}_k$, which for a large expansion order gets increasingly complicated. However, one advantage of the Taylor method is the comparatively small number of equations and the resulting numerical efficiency. On the other hand, phenomena like first-order phase transitions are difficult to dissolve in this approach as the order in the field is limited by the expansion order.

The Taylor expansion method is widely used in the FRG community [47, 61] and can of course also be applied to other scale dependent objects like wave function renormalization factors Z_k, two-point functions or vertex functions $\Gamma_k^{(n)}$ [38].

Grid method

Another common method of solving partial differential equations like Eq. (2.43) is to discretize specific dependencies such that the original differential equation turns into a set of coupled, ordinary differential equations, one for every discretization point. The derivatives in these directions can then be performed numerically by finite differences. In our case we discretize the effective potential $U_k(\rho)$ in field direction so that we obtain the following system of coupled differential equations, each on a fixed field value ρ_i,

$$\begin{aligned}
\partial_k U_k(\rho_1) &= \text{Flow}\left[k, \rho_1, U_k'(\rho_1), U_k''(\rho_1)\right] \\
\partial_k U_k(\rho_2) &= \text{Flow}\left[k, \rho_2, U_k'(\rho_1), U_k''(\rho_2)\right] \\
&\vdots \\
\partial_k U_k(\rho_N) &= \text{Flow}\left[k, \rho_N, U_k'(\rho_N), U_k''(\rho_N)\right] \ .
\end{aligned} \tag{2.48}$$

Since in this method the full field-dependence of the effective potential is taken into account, it is usually numerically more expensive in comparison to the Taylor method where only the scale-dependent minimum $\bar{\rho}_k$ is considered. This general field-dependence is also the strength of the grid method as in principle interaction terms of arbitrary high orders in the fields can be generated during the flow, in contrast to a finite expansion order in the Taylor expansion scheme. Because for this reason it is better suited to describe for example first order phase transitions we will employ the grid method in this work.

Having set up a grid for U_k with usually 60-100 gridpoints, one can gradually solve the resulting coupled system of equations in k with standard methods. Here one should ensure that the flat region of U_k including the k-dependent physical minimum $\rho_{0,k}$ lies always within the covered grid domain, $\rho_1 < \rho_{0,k} < \rho_N$. After adding the explicit symmetry breaking term $c\sigma$ at the IR scale, the physical minimum ρ_0 and the Euclidean particle masses can be directly read off.

Flow equations for retarded two-point functions can then, after the analytic continuation procedure of their Euclidean counterparts (as described in Sec. 2.2.2), be solved on the k-solution of the effective potential and possible other scale-dependent objects like vector meson masses and wave-function renormalization factors. Here we also use the grid method for solving the real and imaginary part of the retarded two-point functions separately on fixed field values, typically the IR minimum $\rho_{0,k\to 0}$. From that, temperature- and chemical-potential dependent spectral functions can be computed with Eq. (2.33). For more details concerning explicit flow equations, the numerical procedure or parameter choices we refer to App. B.

3

QCD and QCD-Effective Models

To gain insights into non-perturbative phenomena like chiral symmetry breaking or the confinement-deconfinement transition, the construction of effective models resembling symmetries and properties of QCD has a long tradition. Common to all these models is to impose specific symmetries present in QCD and to restrict the degrees of freedom in a certain way. The latter can be done e.g. by limiting the number of quark flavors or by introducing effective degrees of freedom, for example meson or baryon fields.

There are several models on the market which have also been investigated within the FRG approach. The underlying model used in this work is the so-called *quark-meson model*, a chirally symmetric low-energy model of QCD with two flavors including the sigma meson and the pions as scalar mesons and quark-antiquark fields as fermions which enables to study spontaneous chiral symmetry breaking, see [74,79–81] for previous FRG studies on this model. To describe the confinement-deconfinement transition, the quark-meson model can be extended by means of introducing a gauge field and a Polyakov loop potential, then called *Polyakov-quark-meson model*, see [75, 82, 83].

A chirally invariant way of describing nucleons in such two-flavor models leads to the concept of parity-doubling and the so-called *parity-doublet model*, see [84] for a general review and [85] for a first FRG study. Here the difficulty is to ensure the nucleons to have a finite mass in the chirally symmetric phase, in contrast to fermions described by quark-meson-type models.

After recapitulating basics of QCD in Sec. 3.1 we will introduce the quark-meson model as well as the Polyakov extension and show first FRG results in Sec. 3.2. In section Sec. 3.3 we will then focus on the parity-doublet model. Here we will discuss the idea of parity doubling and present FRG results also for this model.

3.1 Basics of QCD

Quantum Chromodynamics (QCD) is the field theoretical description of quarks and gluons, the fundamental degrees of freedom of the strong interaction. The corresponding Lagrangian consists of a matter sector with N_f quark flavors with current quark mass m_f, which is coupled to a gauge sector with non-Abelian gauge group $SU(3)$, related to $N_c = 3$, the number of color charges,

$$\mathcal{L}_{\mathrm{QCD}} = \sum_f \bar{\psi}_f \left(\mathrm{i}\not{D} - m_{\mathrm{f}}\right) \psi_f - \frac{1}{4} F^a_{\mu\nu} F^{a\mu\nu} \,. \tag{3.1}$$

Here, we introduced the covariant derivative $D_\mu = \partial_\mu - \mathrm{i}gT^a A^a_\mu$ and the gluon field strength tensor $F^a_{\mu\nu} = \partial_\mu A^a_\nu - \partial_\nu A^a_\mu + g f^{abc} A^b_\mu A^c_\nu$, with gauge coupling g, the generators of the gauge group T^a, the gluon fields A^a_μ being in the adjoint representation of $SU(3)$, and the $SU(3)$ structure constants f^{abc}.

As QCD is a gauge theory, its Lagrangian is invariant under local gauge transformations $U(x) \in SU(3)$,

$$\psi(x) \to U(x)\psi(x) \,, \qquad A_\mu(x) \to U(x) \left(A_\mu(x) + \frac{\mathrm{i}}{g} \partial_\mu \right) U^\dagger(x) \,. \tag{3.2}$$

The non-Abelian character of this gauge group also allow for gluonic self-interactions, see for example [86] for a detailed introduction to Quantum Chromodynamics.

In the low-energy regime of QCD there are two prominent non-perturbative effects on which we will focus in the following: chiral symmetry and confinement.

Chiral symmetry

For vanishing quark masses $m_f \to 0$, also called *chiral limit*, the QCD Lagrangian in Eq. (3.1) is invariant under the independent transformation of left- and right-handed quark fields $\psi_{L/R} = \frac{1}{2}(1 \pm \gamma_5)\psi$ of the form $U_{L/R}\,\psi_{L/R}$ with $U_{L/R} \in U(N_f)$. The resulting flavor symmetry $U(N_f)_L \times U(N_f)_R$ can be decomposed in the form

$$U(N_f)_L \times U(N_f)_R = U(1)_V \times SU(N_f)_V \times SU(N_f)_A \times U(1)_A \,, \tag{3.3}$$

where the indices V and A refer to *vector* and *axial-vector*, relating to the Lorentz transformation properties of the associated conserved currents.

The exact global symmetry $U(1)_V$ implies the conservation of baryon number and is also realized for finite quark masses, the axial symmetry $U(1)_A$ is broken by quantization, referred to as *axial anomaly* [87]. The remaining chiral symmetry $SU(N_f)_V \times SU(N_f)_A$ is in the ground state spontaneously broken to $SU(N_f)_V$ signaled by a non-vanishing *chiral condensate* $\langle\bar{\psi}\psi\rangle$. The latter also gives rise to $N_f^2 - 1$ massless Goldstone bosons. One direct consequence of this spontaneous chiral symmetry breaking is the absence of degenerate masses of parity partners in the vacuum. Spontaneous chiral symmetry breaking also generates the largest part of the hadron masses as the current quark masses, especially of up and down quarks, are much smaller than their constituent ones.

Due to these finite current quark masses in QCD, chiral symmetry is also explicitly broken. Here it can only be treated as approximative symmetry for $N_f = 2$, where

the mass differences and the masses of up and down quarks itself are small compared to the typical QCD scale Λ_{QCD} (cf. *partially conserved axial current* [88]). The pions as associated Goldstone bosons are no longer massless and are therefore often called *pseudo*-Goldstone bosons. The pion mass and its decay constant can be related with the bare quark masses and the chiral condensate by the Gell-Mann-Oakes-Renner relation [89].

Confinement

Another prominent phenomenon is the absence of colored states in the low-energy regime of QCD, known as *confinement*. The emerging symmetry in the gauge sector for static, thus infinitely heavy quarks is the so-called *center symmetry*. It describes the invariance of the gauge sector of the QCD action with respect to transformations of the form $U(t + 1/T, \vec{x}) = h\, U(t, \vec{x})$, with $h \in Z_3$ being in the center of the gauge group $SU(3)$. In contrast, the so-called *Polyakov loop* defined by

$$\Phi(x) = \frac{1}{N_c} \mathrm{Tr}_c \left[\mathcal{P} \exp \left(\mathrm{i} \int_0^\beta d\tau A_0(x) \right) \right] , \tag{3.4}$$

with $\mathcal{P}$ denoting the path ordering of the exponential, transforms non-trivially under these Z_3 transformation, namely $\Phi'(x) = h\, \Phi(x)$. It can further be shown that the thermal expectation value of the Polyakov loop provides a connection to the free energy of a static test quark,

$$\Phi_0 \equiv \langle \Phi(x) \rangle \propto \exp\left(-\beta F_{\mathrm{q}}\right) . \tag{3.5}$$

If color is confined and hence the free energy of a static test quark is infinitely large we have $\Phi_0 = 0$, whereas for deconfined color sources with a finite free energy we have $\Phi_0 > 0$. The expectation value of the Polaykov loop defined in Eq. (3.5) thus serves as an order parameter for the confinement-deconfinement phase transition. The same arguments hold for an antiquark where in this case the order parameter is usually denoted by Φ_0^*.

As dynamical quarks break center symmetry explicitly, this symmetry as well as the connection to confinement is only well-defined in the limit of infinitely heavy quarks, analogously to the explicit chiral symmetry breaking discussed above. Consequently, the phase transitions for finite temperature turn into smooth crossover transitions in both cases.

3.2 Quark-Meson Model

3.2.1 Model Construction

The quark-meson model represents a bosonized low-energy effective model for QCD with two quark flavors incorporating the chiral aspects of full QCD. As linear realization of chiral symmetry it has its origin in the so-called *linear sigma model* [90–92]. Since the chiral phase transition of QCD with two flavors of massless quarks is expected to lie in the $O(4)$ universality class as long as $U(1)_A$ remains anomalously broken at the transition in this limit [93, 94], these types of models can provide qualitative insights into the corresponding critical phenomena also of full QCD.

For $N_f = 2$ we have the up and down quark as fermions and the sigma meson and three pions as scalar mesons with $\sigma \equiv \bar{\psi}\psi$ being the scalar iso-singlet and $\vec{\pi} \equiv \mathrm{i}\bar{\psi}\vec{\tau}\gamma_5\psi$ being the pseudo-scalar iso-triplet state usually denoted in the $O(4)$ notation $\phi = (\sigma, \vec{\pi})^\top$. By applying the chiral transformations

$$SU(2)_V : \psi \to \mathrm{e}^{\mathrm{i}\tau_i\theta_i}\psi\,, \qquad SU(2)_A : \psi \to \mathrm{e}^{\mathrm{i}\gamma_5\tau_i\theta_i}\psi\,, \tag{3.6}$$

to these states, it turns out that only the combination $\rho \equiv \phi^2 = \sigma^2 + \vec{\pi}^2$ is chirally invariant. From that one can construct the following chirally invariant Lagrangian of the quark-meson model (in Euclidean space-time)

$$\mathcal{L}_{\mathrm{QM}} = \bar{\psi}\left(\partial\!\!\!/ + h\left(\sigma + \mathrm{i}\vec{\tau}\vec{\pi}\gamma_5\right)\right)\psi + \frac{1}{2}(\partial_\mu\phi)^2 + U(\phi^2)\,. \tag{3.7}$$

The first part contains the kinetic term for the quark-antiquark fields as well as the coupling to the mesons via the Yukawa coupling h. Since the sigma meson is coupled to a scalar combination of the quark-antiquark fields and the pions to a pseudo-scalar one, this interaction term is also chirally invariant. Here, a finite expectation value of the sigma field $\sigma_0 \equiv \langle\sigma\rangle$ serves as quark mass term, i.e. $m_\psi = h\sigma_0$, where from the Goldberger-Treiman relation it follows that the vacuum value of σ_0 coincides with the pion decay constant f_π [88] (in the LPA truncation). We note that σ_0 as an order parameter for spontaneous chiral symmetry breaking in these types of models is proportional to the chiral condensate $\langle\bar{\psi}\psi\rangle$ introduced in Sec. 3.1.

The second part of Eq. (3.7) consists of the usual kinetic term for bosonic fields and an effective potential $U(\phi^2)$ containing mesonic self-interaction terms of in principle arbitrary order in the chirally invariant ρ. To exhibit spontaneous symmetry breaking, this polynomial potential has to have its minimum at $\sigma_0 = f_\pi$ in the vacuum, cf. the so-called *mexican hat potential* [88]. In order to also account for a finite current quark mass one adds an explicitly symmetry breaking term $c\sigma$ to the Lagrangian in Eq. (3.7) which is a bosonized version of the current quark mass term $m_\psi\bar{\psi}\psi$ in the QCD Lagrangian. This also results in a finite mass for the pions as pseudo-Goldstone bosons where the parameter c is usually chosen to reproduce the physical pion mass.

Flow equation for the effective potential

To employ the quark-meson model within the FRG framework, we perform a derivative expansion to lowest order as an ansatz for the effective average action and include the terms which are consistent with chiral symmetry. It follows that

$$\Gamma_k = \int d^4x \left\{\bar{\psi}\left(\partial\!\!\!/ - \mu\gamma_0 + h\left(\sigma + \mathrm{i}\vec{\tau}\vec{\pi}\gamma_5\right)\right)\psi + \frac{1}{2}(\partial_\mu\phi)^2 + U_k(\phi^2)\right\}, \tag{3.8}$$

where we introduced the quark chemical potential μ in the standard way, temperature is included via the Matsubara formalism, cf. App. A. In this simple LPA ansatz, the effective potential is the only scale-dependent quantity, see Sec. 2.3.1. By inserting this ansatz into the Wetterich equation, Eq. (2.23), in combination with a three-dimensional version of the Litim regulator, cf. App. B.1, one obtains the

flow equation for the effective potential,

$$\partial_k U_k = \frac{k^4}{12\pi^2}\Big\{\frac{1+2\,n_B(E_{\sigma,k})}{E_{\sigma,k}} + \frac{3\,(1+2\,n_B(E_{\pi,k}))}{E_{\pi,k}} - \frac{4N_f N_c}{E_{\psi,k}}\left(1-n_F(E_{\psi,k}-\mu)-n_F(E_{\psi,k}+\mu)\right)\Big\}, \tag{3.9}$$

where n_B and n_F are bosonic and fermionic occupation numbers. The minus sign in front of the fermionic part is crucial for generating a non-vanishing expectation value σ_0 at intermediate scales.

In the numerical calculation we start with the following initial form of the effective potential at the UV scale $\Lambda = 1500$ MeV,

$$U_{k=\Lambda}(\phi) = b_1\,\phi^2 + b_2\,\phi^4\,. \tag{3.10}$$

The explicitly symmetry breaking term $c\sigma$ does not contribute to the flow of U_k and is therefore only added at the IR scale $k_{\mathrm{IR}} = 40$ MeV, after solving the flow equation. Here one can also read off the energies and the Euclidean masses of the sigma meson, the pions, and the quark-antiquarks, which are defined as follows

$$E^2_{\sigma,k} = m^2_{\sigma,k} + k^2 = 2\,U'_k(\rho) + 4\,\rho\,U''_k(\rho) + k^2, \tag{3.11}$$

$$E^2_{\pi,k} = m^2_{\pi,k} + k^2 = 2\,U'_k(\rho) + k^2, \tag{3.12}$$

$$E^2_{\psi,k} = m^2_{\psi,k} + k^2 = h^2\rho + k^2. \tag{3.13}$$

We note that these masses are in principle only meaningful as such when evaluated at the physical minimum in field space $\rho = \sigma_0^2$.

The parameters listed in Tab. 3.1 are chosen such that in the vacuum we have a constituent quark mass of $m_\psi = 300$ MeV and phenomenologically reasonable values for the pion and sigma masses and the pion decay constant, identified with the global minimum of the effective potential: $m_\pi = 140$ MeV, $m_\sigma = 557$ MeV and $f_\pi = \sigma_0 = 93.0$ MeV [41].

3.2.2 Phase Structure: FRG Results

By solving the flow equation for the effective potential given in Eq. (3.9) one can compute the phase diagram of the quark-meson model within the LPA ansatz by means of the temperature- and quark chemical-potential dependent chiral order parameter, determined by the global minimum of the effective potential at the IR scale, $\sigma_0 = \sigma_0(T,\mu)$. The phase diagram within this truncation is a well-known result and basis for the calculation of spectral functions in later chapters.

In Fig. 3.1a we see a contour plot of the chiral order parameter σ_0 as a function of temperature T and quark chemical potential μ. Once the vacuum value is

Λ [GeV]	b_1 [GeV^2]	b_2	c [GeV^3]	h
1.5	0.8573	0.2	$1.8228{\cdot}10^{-3}$	3.226

Table 3.1: Parameter set.

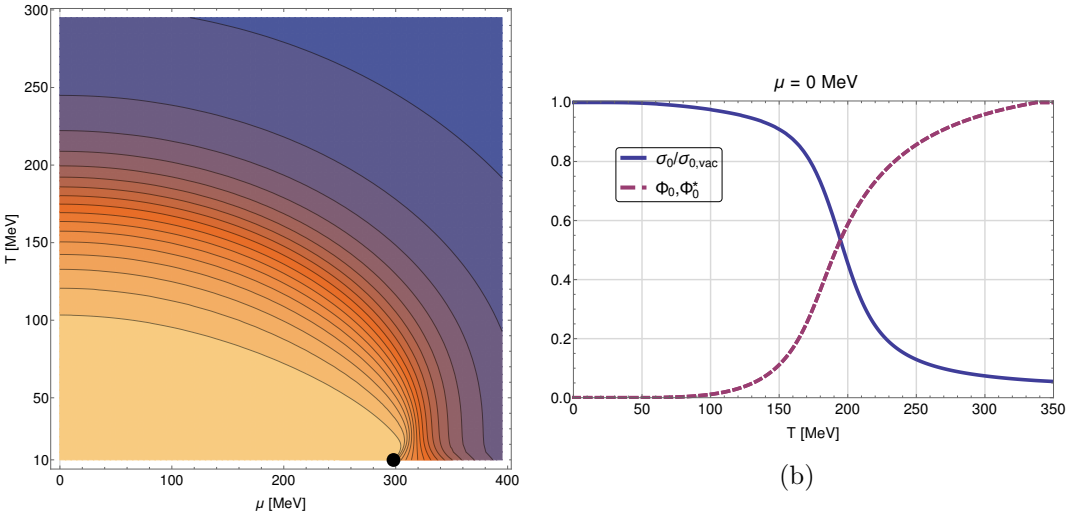

(a) (b)

Figure 3.1: Phase diagram of the quark-meson model as contour plot of the chiral order parameter $\sigma_0(T, \mu)$ (a) and σ_0 together with the Polyakov loops Φ and Φ^*, the order parameters for the confinement-deconfinement transition along the T-axis at $\mu = 0$ MeV [95] (b).

fixed to $\sigma_{0,\text{vac}} = 93$ MeV (Goldberger-Treiman relation), chiral symmetry gets gradually restored by increasing the temperature and/or the chemical potential which is signaled by a decreasing value of $\sigma_0(T, \mu)$ (darker color in Fig. 3.1a). At low temperature and large chemical potential, $(T_{\text{CEP}}; \mu_{\text{CEP}}) \approx (10; 298)$ MeV, we find a critical endpoint (CEP) which represents a second-order phase transition (black dot) dividing the broad crossover region from a first-order phase transition for even lower temperatures $T < 10$ MeV.

For the analysis with spectral functions in later chapters we will mainly focus on signatures for the restoration of chiral symmetry and for the CEP, i.e. we will study spectral functions along the temperature-axis at vanishing chemical potential and along the axis of the CEP as a function of chemical potential and fixed temperature, here at $T = 10$ MeV.

As a last point, we mention that the slope $dT/d\mu$ of the first-order line in these type of calculations is very different to the one obtained by mean-field calculations, cf. [96]. This leads to unphysical results for example for the entropy density in the regime to the right of this first-order line, see [81] for further discussions on this problem. However, there is evidence that an enhanced truncation scheme towards LPA′ could resolve this issue [97].

3.2.3 Polyakov-Quark-Meson Model

Since the quark-meson model does not contain gluonic degrees of freedom it is not able to describe the confinement phenomenon. The quark-meson model extended by means of including a mean-field gluon field and a so-called Polyakov loop potential $\mathcal{U}(\Phi, \Phi^*)$ leads to the Polayakov-quark-meson model. The ansatz for the effective

action is similar to Eq. (3.8) and reads

$$\Gamma_k = \int d^4x \left\{ \bar{\psi} \left(\not{\partial} - \mu\gamma_0 + h \left(\sigma + \mathrm{i}\vec{\tau}\vec{\pi}\gamma_5 \right) \right) \psi + \frac{1}{2}(\partial_\mu \phi)^2 + \Omega_k(\phi^2, \Phi, \Phi^*) \right\}, \quad (3.14)$$

with $\Omega_\Lambda(\phi^2, \Phi, \Phi^*) = U_\Lambda(\phi^2) + \mathcal{U}_\Lambda(\Phi, \Phi^*)$. Taking merely the constant time component of the gluon field into account and using the fact that we only have two degrees of freedom, given by the Polyakov loops, we can always rotate in group space in a way that only the diagonal Gell-Mann matrices λ_3 and λ_8 contribute. We therefore have for the covariant derivative $D_\mu = \partial_\mu - \mathrm{i}gT^a A^a_\mu \delta^\mu_0$ with T^a being the Gell-Mann matrices and $a = 3, 8$ [98]. The minimum of the polynomial [99, 100] or logarithmic [101] Polyakov loop potential $\mathcal{U}_\Lambda(\Phi, \Phi^*)$ then defines the order parameters Φ and Φ^*.

The flow equation of the effective potential Ω_k looks the same as in Eq. (3.9) except that the fermionic occupation numbers $n_F(E_{\psi,k} \mp \mu)$ are replaced by generalized ones containing the Polyakov loops,

$$N_\mathrm{F}(E_{\psi,k} \mp \mu) \equiv \frac{1 + \mathrm{e}^{2(E_{\psi,k} \mp \mu)/T}\Phi + 2\mathrm{e}^{(E_{\psi,k} \mp \mu)/T}\Phi^*}{1 + \mathrm{e}^{3(E_{\psi,k} \mp \mu)/T} + 3\mathrm{e}^{2(E_{\psi,k} \mp \mu)/T}\Phi + 3\mathrm{e}^{(E_{\psi,k} \mp \mu)/T}\Phi^*}\,. \quad (3.15)$$

In the limit of vanishing gluon fields and deconfined quarks/antiquarks $\Phi, \Phi^* \to 1$ these generalized fermionic occupation numbers reduce to the usual ones and we recover the quark-meson model. The order parameters $\chi_0 = (\sigma_0, \Phi_0, \Phi_0^*)$ in the Polyakov-quark-meson model are then determined by solving the following equations of motion,

$$\left.\frac{\partial \Omega_{k\to 0}}{\partial \sigma}\right|_{\chi_0} = \left.\frac{\partial \Omega_{k\to 0}}{\partial \Phi}\right|_{\chi_0} = \left.\frac{\partial \Omega_{k\to 0}}{\partial \Phi^*}\right|_{\chi_0} \stackrel{!}{=} 0\,. \quad (3.16)$$

In Fig. 3.1b we see the normalised chiral order parameter and Φ, Φ^* as a function of temperature for vanishing chemical potential. At $\mu = 0$ MeV the Polyakov loop and its conjugate are degenerate, as expected. As σ_0 decreases strongly between $T = 150$ MeV and $T = 250$ MeV, the Polyakov loops do just the opposite, increasing strongly in this region until arriving in the deconfined phase for $T \gtrsim 330$ MeV. The crossover transition in both cases happens approximately at the same temperature, defined by the first temperature-derivative peak, $T_\chi \approx 195$ MeV and $T_\mathrm{d} \approx 183$ MeV.

As it turned out, although the Polyakov-quark-meson model works well as statistical model describing confinement in thermodynamics, it is unable to describe confinement in the sense of suppressing quark-antiquark thresholds in the deconfined phase of the phase diagram of the model, apparent for example in mesonic spectral functions [95]. For that reason we will in this work partly stick with the quark-meson model and later overcome the issue of unphysical quark thresholds by replacing the quarks with nucleons within the parity-doublet model.

3.3 Modeling Nucleons: Parity-Doublet Model

3.3.1 Model Construction and the Idea of Parity Doubling

The question of how to describe baryons within effective models incorporating the principle of chiral symmetry has a long history. Here, important work was done by

Walecka who introduced a hadronic model consisting of nucleons, scalar mesons and vector mesons [102] and by Lee and Wick who reformulated the model of Walecka into a chirally invariant version [103]. The latter model is called chiral Walecka model and basically equals the quark-meson model introduced in Sec. 3.2.1 with nucleon instead of quark fields. The problem here is that the baryonic degrees of freedom become massless in the chirally restored phase as in these models their mass is entirely generated by spontaneous chiral symmetry breaking in the chiral limit.

This issue can be resolved by including the parity partners of the nucleons in a chirally invariant way, leading to parity-doublet models. Before introducing the Lagrangian of such a model we discuss the chiral representations of quarks and baryons [84, 104, 105].

Chiral representations for baryons

Let (I_R, I_L) be a representation of the chiral group $SU(2)_R \otimes SU(2)_L$ with I_R and I_L being the value of the isospin. The quark field with right- and left-handed components in this notation is a direct sum of the fundamental representation, namely $\psi \sim (\frac{1}{2}, 0) \oplus (0, \frac{1}{2})$. The representation of a single baryon is given by a direct product of three quarks and can be decomposed as [106]

$$\psi \otimes \psi \otimes \psi \sim 5[(\tfrac{1}{2}, 0) \oplus (0, \tfrac{1}{2})] \oplus 3[(1, \tfrac{1}{2}) \oplus (\tfrac{1}{2}, 1)] \oplus [(\tfrac{3}{2}, 0) \oplus (0, \tfrac{3}{2})]\,. \tag{3.17}$$

The most natural choice for the representation of a nucleon is $(\frac{1}{2}, 0) \oplus (0, \frac{1}{2})$ as this transforms in the same way as a quark field.

If we now consider two baryon species with right- and left- handed components $\psi_{1,r/l}$ and $\psi_{2,r/l}$, both in the $(\frac{1}{2}, 0) \oplus (0, \frac{1}{2})$ representation, there are two possible assignments of the chiral transformations. In the *naive* assignment both baryons transform in the exactly same way, in the *mirror* assignment, however, the second baryon transforms in the opposite way, namely $\psi_{2,r} \to U_L \psi_{2,r}$ and $\psi_{2,l} \to U_R \psi_{2,l}$ with $U_{L/R} \in SU(2)_{L/R}$. In this mirror assignment, first introduced in [107], it is possible to introduce a chirally invariant bare mass term to the Lagrangian giving the baryons a mass, also in the chirally restored phase. This invariant mass term reads

$$\begin{aligned} \mathcal{L}_{\mathrm{M}} &= m_{0,B} \left(\bar{\psi}_1 \psi_2 + \bar{\psi}_2 \psi_1 \right) \\ &= m_{0,B} \left(\psi_{1,r}^\dagger \psi_{2,l} + \psi_{2,l}^\dagger \psi_{1,r} + \psi_{2,r}^\dagger \psi_{1,l} + \psi_{1,l}^\dagger \psi_{2,r} \right) . \end{aligned} \tag{3.18}$$

FRG treatment of the parity-doublet model

The Lagrangian of the parity-doublet model consists of a mesonic part, which is the same as in the quark-meson model, cf. Eq. (3.7), and a fermionic part with two species of mirror-assigned baryons $N_1 \equiv \psi_1$ and $N_2 \equiv \gamma_5 \psi_2$ as degrees of freedom. These baryonic fields are iso-doublets representing the nucleons (p, n) and their

parity partners. The LPA ansatz for the effective average action then reads

$$\begin{aligned}\Gamma_k = \int d^4x \Big\{ &\bar{N}_1 \left(\partial\!\!\!/ - \mu_B\gamma_0 + h_1\left(\sigma + \mathrm{i}\vec{\tau}\vec{\pi}\gamma_5\right)\right) N_1 + \\ &\bar{N}_2 \left(\partial\!\!\!/ - \mu_B\gamma_0 + h_2\left(\sigma - \mathrm{i}\vec{\tau}\vec{\pi}\gamma_5\right)\right) N_2 + \\ &m_{0,B}\left(\bar{N}_1\gamma_5 N_2 - \bar{N}_2\gamma_5 N_1\right) + \frac{1}{2}(\partial_\mu\phi)^2 + U_k(\phi^2)\Big\}\,. \end{aligned} \tag{3.19}$$

The first two parts of this ansatz represent the standard fermionic part including a kinetic term, the baryon chemical potential μ_B and the coupling to the mesonic degrees of freedom where we note that the parity partner N_2 has a minus sign in the coupling to the pions. The third part is a chirally invariant mass term, giving the nucleons the bare mass $m_{0,B}$, cf. Eq. (3.18). The remaining mesonic parts are the same as in Eq. (3.8).

For the flow equation of the effective potential U_k we then obtain

$$\partial_k U_k = \frac{k^4}{12\pi^2}\Big\{ \frac{1 + 2\,n_B(E_{\sigma,k})}{E_{\sigma,k}} + \frac{3\,(1 + 2\,n_B(E_{\pi,k}))}{E_{\pi,k}} + \tag{3.20}$$

$$\frac{4N_f}{E_{B_1,k}\,E_{B_2,k}}\big(- (E_{B_1,k} + E_{B_2,k}) + \tag{3.21}$$

$$E_{B_2,k}\,n_F(E_{B_1,k} - \mu_B) + E_{B_1,k}\,n_F(E_{B_2,k} - \mu_B) + \tag{3.22}$$

$$E_{B_2,k}\,n_F(E_{B_1,k} + \mu_B) + E_{B_1,k}\,n_F(E_{B_2,k} + \mu_B)\big)\Big\}\,.$$

As expected, the mesonic part is the same as in the pure quark-meson model, cf. Eq. (3.9). For the fermionic part we introduced k-dependent particle energies for the nucleon and its parity partner, given by

$$\begin{aligned} E^2_{B_1,k} &= \frac{1}{2}\left(2k^2 + 2m^2_{0,B} + h_1^2\sigma_0^2 + h_2^2\sigma_0^2 + \sigma_0(h_1 - h_2)\sqrt{\sigma_0^2(h_1 + h_2)^2 + 4m^2_{0,B}}\right)\,, \\ E^2_{B_2,k} &= \frac{1}{2}\left(2k^2 + 2m^2_{0,B} + h_1^2\sigma_0^2 + h_2^2\sigma_0^2 - \sigma_0(h_1 - h_2)\sqrt{\sigma_0^2(h_1 + h_2)^2 + 4m^2_{0,B}}\right)\,. \end{aligned} \tag{3.23}$$

For the initial form of the effective potential at the UV scale $\Lambda = 2500$ MeV we chose the same ansatz as for the quark-meson model, Eq. (3.10).

The masses of the nucleon and its parity partner are given by the Eigenvalues of the mass matrix

$$M = \begin{pmatrix} h_1\sigma_0\mathbb{1} & m_{0,B}\gamma_5 \\ -m_{0,B}\gamma_5 & h_2\sigma_0\mathbb{1} \end{pmatrix}\,, \tag{3.24}$$

and are explicitly given by

$$m_{B_1} = \frac{1}{2}\left(+(h_1 - h_2)\sigma_0 + \sqrt{4m^2_{0,B} + (h_1 + h_2)^2\sigma_0^2}\right)\,, \tag{3.25}$$

$$m_{B_2} = \frac{1}{2}\left(-(h_1 - h_2)\sigma_0 + \sqrt{4m^2_{0,B} + (h_1 + h_2)^2\sigma_0^2}\right)\,. \tag{3.26}$$

As expected for chiral partners, for $\sigma \to 0$ the two masses become degenerate to the bare value $m_{0,B}$. We also note that for $m_{0,B} = 0$ the model reduces to a sum of

Λ [GeV]	b_1 [GeV^2]	b_2	c [GeV^3]	h_1	h_2	$m_{0,B}$ [GeV]
2.5	6.016	0.2	$1.8028{\cdot}10^{-3}$	7.75033	14.1697	0.7

Table 3.2: Parameter set.

two quark-meson models with masses $m_1 = h_1\sigma_0$ and $m_2 = h_2\sigma_0$ where the particle energies in Eq. (3.23) reduce to $E_{1,k}^2 = k^2 + m_1^2$ and $E_{2,k}^2 = k^2 + m_2^2$.

The parameters in this model, shown in Tab. 3.2, were also chosen to reproduce physically reasonable values for the particular Euclidean particle masses as well as for the pion decay constant in the vacuum: $m_{B,1} = 938.3$ MeV, $m_{B,2} = 1535.6$ MeV, $m_\sigma = 633.5$ MeV, $m_\pi = 140.9$ MeV and $\sigma_0 = 93.0$ MeV.

3.3.2 Phase Structure: FRG Results

As discussed for the quark-meson model in Sec. 3.2.2, we can also calculate a phase diagram for the parity-doublet model by means of the temperature- and baryon chemical-potential dependent chiral order parameter $\sigma_0 = \sigma_0(T, \mu)$ identified with the global minimum of the effective potential at the IR scale. The resulting phase diagram is shown in Fig. 3.2a where we again fixed the vacuum value to $\sigma_{0,\text{vac}} = 93$ MeV. In addition to a chiral first-order line ending in a CEP, the parity doublet model shows a second first-order line which ends in a CEP representing the liquid-gas phase transition of nuclear matter.

Phenomenologically, the value of the in-medium condensate right to the liquid-gas first-order line can be determined by relating the Feynman-Hellmann theorem [108] and the Gell-Mann-Oakes-Renner relation resulting in a relation between the in-medium condensate $\bar{\sigma}(n_0)$ and the saturation density of nuclear matter n_0. With $n_0 \simeq 0.16$ fm^{-3} this gives an in-medium condensate of $\bar{\sigma}(n_0) \simeq 69$ MeV [109, 110]. The phenomenologically correct location of the liquid-gas first-order line is fixed by reproducing the binding energy of $E_b \simeq 16$ MeV per nucleon in symmetric nuclear matter. It is given by the difference between the nucleon mass and the location of the first-order line, for the latter we hence obtain $\mu_B^c = 939$ MeV $- 16$ MeV $= 923$ MeV.

In our FRG results, the position and the magnitude of this liquid-gas transition as a function of baryon chemical potential at low temperatures strongly depend on the scale-independent bare nucleon mass $m_{0,B}$. The chiral order parameter σ_0 as a function of baryon chemical potential at $T = 1$ MeV for different values of $m_{0,B}$ is shown in Fig. 3.2b. The larger the value of $m_{0,B}$ the more does the location of the discontinuity move towards larger μ_B, at the same time the magnitude of the transition gets weaker resulting in a larger in-medium condensate. For $m_{0,B} = 900$ MeV the transition even disappears completely. In this calculation we fixed the masses of the nucleon and its parity partner in the vacuum to $m_{B_1} = 939$ MeV and $m_{B_2} = 1535$ MeV for all values of $m_{0,B}$ (as in [85] we chose the $N(1535)$ and not the $N(1640)$ to be the chiral partner), cf. App. B for further details concerning the numerical procedure.

Even with the inclusion of a repulsive mean-field ω meson, which basically shifts the liquid-gas transition to larger μ_B but also lowers its magnitude (as described in [85]), it was not possible to fix the correct binding energy and the correct in-medium condensate simultaneously in the present LPA truncation. We therefore chose $m_{0,B} = 700$ MeV to be the best trade-off regarding the magnitude and loca-

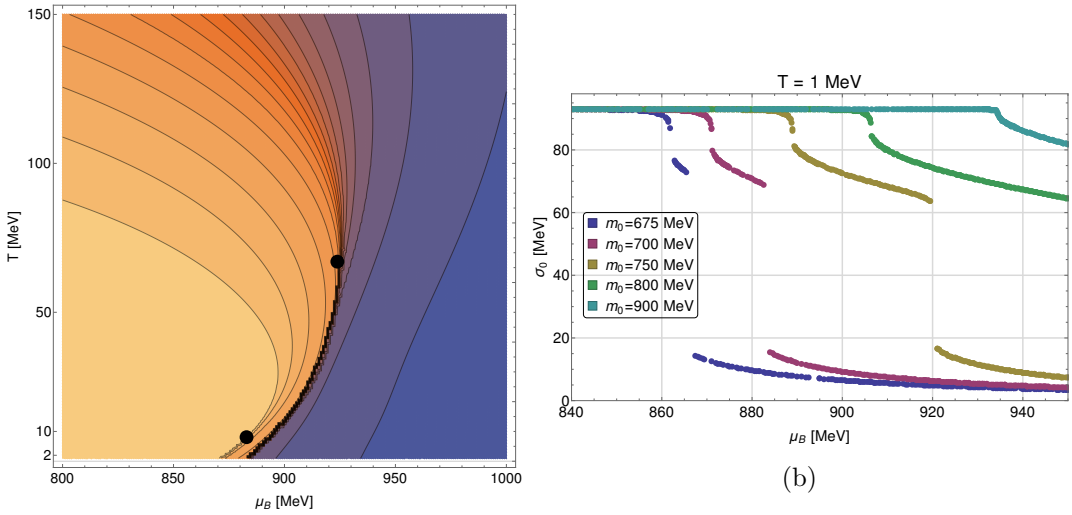

(a) (b)

Figure 3.2: Phase diagram of the parity-doublet model as contour plot of the chiral order parameter $\sigma_0(T, \mu)$ (a) and σ_0 as a function of baryon chemical potential μ_B at $T = 1$ MeV for different values of the bare baryon mass $m_{0,B}$ (b).

tion of the first-order transition and consider the parity-doublet model as a purely qualitative description of nuclear matter improving the phenomenology of spectral functions, as will be discussed in later chapters.

With this setting (and without the mean-field ω meson) we find the CEP for the liquid-gas transition and the chiral transition at

$$(T^{lg}; \mu_{\mathrm{B}}^{lg}) \approx (8; 883)\ \mathrm{MeV}\,, \qquad (T^{\chi}; \mu_{\mathrm{B}}^{\chi}) \approx (67; 924)\ \mathrm{MeV}\,, \tag{3.27}$$

indicated as black dots in Fig. 3.2a. As for the phase diagram of the quark-meson model, the critical endpoints separate a broad crossover transition from a first order phase transition for lower temperatures. With increasing temperature and/or baryon chemical potential chiral symmetry gets successively restored, indicated by a lowering of $\sigma_0(T, \mu)$ and a darker color in Fig. 3.2a. As already discussed in Sec. 3.2.2, we mention the issue of the curvature of the chiral first-order line which seems to be inconsistent with the Clausius-Clapeyron relation

$$\frac{dT_{\mathrm{c}}}{d\mu_{\mathrm{c}}} = -\frac{\Delta n}{\Delta s}\,. \tag{3.28}$$

Here, the change of the particle density Δn as well as of the entropy density (per volume) Δs is expected to be positive since the entropy per particle increases in such a transition. In contrast, from a gaseous to a liquid phase the entropy per particle is expected to decrease and it therefore depends on the magnitude of the change in the number density if the entropy density s decreases or increases. However, a possible negative change Δs (seen in Fig. 3.2a) should not be larger than the entropy density on the gaseous side which would then lead to regions of negative entropy density beyond the critical line.

4

Describing Vector Mesons

A phenomenologically important extension of the effective models introduced in Chapter 3 is the inclusion of spin-1-mesons, the vector and axial-vector mesons. From an experimental point of view, vector mesons are interesting as they carry the same quantum numbers as the photon and lepton pairs and therefore provide detectable information about the inner structure of strong-interaction matter.

The history of vector mesons began along two different paths in physics, a theoretical one pioneered by Sakurai [111] and an experimental one driven by discrepancies in form-factor measurements [112,113], see [114–116] for general reviews. These two seemingly different concepts could then be unified in terms of the concept of *vector meson dominance* (VMD) [117, 118]. According to Sakurai, vector mesons are introduced as gauge bosons arising from a local gauge symmetry, which later was extended to the full chiral symmetry group [119].

Apart from first studies of vector mesons within such effective models with the FRG [41, 120, 121], an accepted theoretical description especially of fluctuations due to (axial-)vector mesons is, up to now, still missing. To describe massive vectors as fundamental fields in such effective models is known to be problematic [122, 123], if not impossible without the Higgs mechanism. However, in this chapter we propose a formulation of fluctuating (axial-)vector mesons by means of the FRG approach based on covariance and transversality of the single-particle contribution to its propagator [123].

We begin by reviewing the history of vector mesons and the emerged concept of vector meson dominance in Sec. 4.1. In Sec. 4.2 we present the gauged linear sigma model with quarks as an effective model including vector and axial-vector mesons in the spirit of VMD and discuss its treatment within the FRG. Here we also present the formulation of massive vector mesons within the FRG framework and show first results for the RG-flow of the Euclidean masses of the model. This model will then be extended by including the electromagnetic field and by introducing baryon degrees of freedom, as discussed in Sec. 4.3

4.1 History and Vector Meson Dominance

The existence of vector mesons in experiments became first apparent during electromagnetic form factor measurements of the nucleon in electron-scattering experiments in the 1950ies. Here, in 1957 Nambu introduced an iso-scalar vector meson ρ^0, later identified with the ω-meson, as a three-pion resonance to explain the discrepancy in the proton an neutron charge radii [112]. A few years later, in 1959, Frazer and Fulco resolved the inconsistency of simultaneously explaining the value of the magnetic moments and the charge and momentum radii distributions by including a strong pion-pion interaction in their dispersion-relation analysis [113]. This pion-pion resonance was then identified with an iso-triplet vector meson, the ρ meson.

From the theoretical side it was Sakurai in 1960 who changed the point of view in the theoretical description of the strong interaction [111]. Guided from the success of quantum electrodynamics (QED) and the generalization to local $SU(2)$ gauge invariance by Yang and Mills [124], he proposed to apply this local gauge principle also in hadron physics. In this way, he introduced vector mesons as arising gauge bosons by adopting a local $SU(2)$ flavor symmetry, the issue of a vector meson mass term breaking this gauge invariance was ignored at that time. This work from Sakurai also was an important step in the development of the quark model in 1964 [2, 125] in which vector mesons are now identified as bound states of a quark-antiquark pair with spin one. However, in effective low-energy models for QCD, vector mesons are frequently still seen as gauge bosons quite in the spirit of Sakurai.

By generalizing the experimental findings described above and adopting the idea of local quantum field theory, the concept of vector meson dominance (VMD) was born [117, 118]. Phenomenologically, this concept means that the photon interacts with a target hadron mainly via the exchange of a vector meson, i.e. the hadronic contributions to the photon propagator consist of propagating vector mesons, illustrated in Fig. 4.1.

On a formal level, VMD can be imprinted in a so-called *current-field identity* (CFI) which basically says that within this concept the electromagnetic current is given as linear combination of the vector meson fields, for the iso-vector component

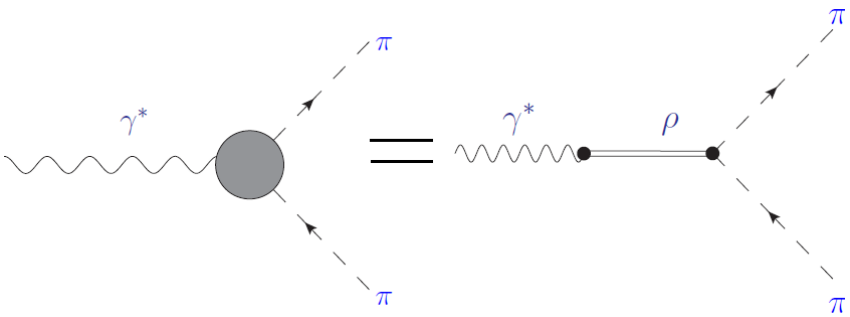

Figure 4.1: Illustration of the decay of an off-shell photon into a pion pair in the sense of VMD. The interaction between the photon and the pions is mediated by a ρ meson as intermediate state of the propagating photon (from [126]).

given by [127]

$$\left(j_\mu^{\text{em}}\right)_{\text{iso-vector}} = -\frac{m_\rho^2}{g_\rho}\,\rho_\mu\,, \tag{4.1}$$

with m_ρ being the ρ meson mass and g_ρ the coupling constant. The conservation of the electromagnetic current then requires $\partial_\mu \rho^\mu = 0$, which is the Proca condition and leads to a Lagrangian for massive spin-1 particles. The problem of loosing gauge invariance and thus transversality of the associated Green function by a finite bare mass in this formalism was ignored at that time as the focus was put on the application of the gauge principle.

In order to construct an effective low-energy model for QCD including vector and axial-vector mesons, the idea of local gauge invariance from Sakurai was extended to the full chiral group $SU(2)_\text{V} \times SU(2)_\text{A}$ [119] to also include the chiral partner of the ρ meson, the $a_1(1260)$ meson. To construct a chiral Lagrangian within this setting there are different approaches on the market. In a non-linear realization of chiral symmetry there is the so-called *Massive Yang-Mills Approach* (MYM) [128] and the formalism of *Hidden Local Symmetry* (HLS) [129,130]. A third variant is to impose a local chiral symmetry within the linear sigma model introduced in Sec. 3.2.1, which is then called *gauged linear sigma model* (gLSM). As the formalism of local gauge invariance does not include all interaction terms which are consistent with global chiral symmetry and the same gauge coupling appears in all interaction terms, there is also the possibility to relax the constraint of a local invariance and to only insist on global chiral symmetry, as done for example in [120, 121, 131, 132].

In this work, however, we will follow the idea of VMD and impose a local chiral symmetry on the linear sigma model with quarks and later with nucleons. As shown for example in [121], the assumption of VMD to basically only have one coupling for all interaction terms is a good first approximation. The issue of unphysical degrees of freedom arising from a bare vector meson mass term in the Lagrangian will be resolved by proposing an ansatz for the vector meson propagator within the FRG framework in Sec. 4.2.2.

4.2 Gauged Linear Sigma Model with Quarks: FRG Treatment

4.2.1 Model Construction and Effective Average Action

Mesonic part of the Lagrangian

Starting point in constructing the mesonic part of the Lagrangian of the gauged linear sigma model is the $O(4)$ symmetric model with the mesonic field $\phi = (\sigma, \vec{\pi})^\top$ being in the fundamental representation of $O(4)$. Its Lagrangian simply reads

$$\mathcal{L}_\phi = \frac{1}{2}(\partial_\mu \phi)^2 + U(\phi^2)\,, \tag{4.2}$$

and is invariant under global $O(4)$-transformations of the form

$$\phi \to U\phi\,, \qquad \text{with} \qquad U = \mathrm{e}^{\mathrm{i}\vec{\alpha}\,\vec{T} + \mathrm{i}\vec{\beta}\,\vec{T}^5}\,. \tag{4.3}$$

As the Lie-algebra of $O(4)$ has six dimensions we need six generators, i.e. six anti-symmetric 4×4 matrices $\vec{T}$ and $\vec{T}^{\,5}$. Here one usually chooses $\vec{T}$ as internal rotations of the pion field and $\vec{T}^{\,5}$ as axial transformations rotating pions and the sigma field into each other. Their explicit form is given by

$$(T_i)_{jk} = \begin{pmatrix} -\mathrm{i}\epsilon_{ijk} & \vec{0} \\ \vec{0}^{\,\top} & 0 \end{pmatrix}, \qquad (T_i^5)_{jk} = \begin{pmatrix} 0_{3\times3} & -\mathrm{i}\vec{e}_i \\ \mathrm{i}\vec{e}_i^{\,\top} & 0 \end{pmatrix}. \tag{4.4}$$

These matrices obey the following commutation relations

$$[T_i, T_j] = \mathrm{i}\epsilon_{ijk}T_k\,, \quad [T_i^5, T_j^5] = \mathrm{i}\epsilon_{ijk}T_k\,, \quad [T_i, T_j^5] = \mathrm{i}\epsilon_{ijk}T_k^5\,, \tag{4.5}$$

and their traces are given by

$$\mathrm{Tr}(T_aT_b) = 2\delta_{ab}\,, \quad \mathrm{Tr}(T_a^5T_b^5) = 2\delta_{ab}\,, \quad \mathrm{Tr}(T_aT_b^5) = 0\,. \tag{4.6}$$

In order to see the equivalence of these transformations to the chiral transformations one can use the isomorphism of $O(4) \cong SU(2) \times SU(2)$ and define new generators as linear combination of the $O(4)$ ones, given by

$$T_i^L = \frac{1}{2}(T_i - T_i^5)\,, \qquad T_i^R = \frac{1}{2}(T_i + T_i^5)\,. \tag{4.7}$$

With this redefinition we now have two copies of $SU(2)$ where the matrices $\vec{T}^L$ and $\vec{T}^R$ satisfy the $SU(2)$ commutation relation separately,

$$[T_i^L, T_j^L] = \mathrm{i}\epsilon_{ijk}T_k^L\,, \qquad [T_i^L, T_j^R] = 0\,, \qquad [T_i^R, T_j^R] = \mathrm{i}\epsilon_{ijk}T_k^R\,. \tag{4.8}$$

In the spirit of Sakurai and the concept of vector meson dominance, the next step is to promote this chiral $SU(2)_\mathrm{L} \times SU(2)_\mathrm{R}$ symmetry to a gauge symmetry. The transformation U in Eq. (4.3) thus becomes a local one, $U \to U(x)$ with position-dependent coefficients $\vec{\alpha} = \vec{\alpha}(x)$ and $\vec{\beta} = \vec{\beta}(x)$. To ensure the Lagrangian to be invariant under this transformation we have to replace the standard derivative in Eq. (4.2) with a covariant one,

$$\partial_\mu\phi \to D_\mu\phi \equiv (\partial_\mu - \mathrm{i}gV_\mu)\,\phi\,, \tag{4.9}$$

where g is the gauge coupling and V_μ an element of the Lie-algebra given as linear combination of the generators $V_\mu = \vec{\rho}_\mu\vec{T} + \vec{a}_{1\mu}\vec{T}^{\,5}$. Here, the prefactors can be identified with the vector and axial-vector iso-triplets $\vec{\rho}_\mu$ and $\vec{a}_{1,\mu}$ as gauge bosons. As usual in gauge theories, we also have to introduce a field-strength tensor which in the present case reads

$$V_{\mu\nu} = \frac{\mathrm{i}}{g}\,[D_\mu, D_\nu] = \partial_\mu V_\nu - \partial_\nu V_\mu - \mathrm{i}g[V_\mu, V_\nu]\,. \tag{4.10}$$

The mesonic part of the Lagrangian for the gauged linear sigma model finally consists of the following parts

$$\mathcal{L}_\mathrm{gLSM}^\mathrm{mes} = \mathcal{L}_{\phi,\partial_\mu\to D_\mu} + \mathcal{L}_{m_V} + \mathcal{L}_\mathrm{YM}. \tag{4.11}$$

The first one basically equals Eq. (4.2) with the covariant derivative generating interaction terms of the vector mesons to the scalar mesons. With explicitly symmetry breaking term we obtain

$$\begin{aligned}\mathcal{L}_{\phi,\partial_\mu\to D_\mu} &= \frac{1}{2}(D_\mu\phi)^2 + U(\phi^2) - c\sigma \\ &= \frac{1}{2}(\partial_\mu\phi)^2 - \mathrm{i}gV_\mu\phi\partial_\mu\phi - \frac{1}{2}g^2V_\mu\phi V_\mu\phi + U(\phi^2) - c\sigma\,. \end{aligned} \tag{4.12}$$

The second part represents a bare mass term for the vector meson fields within the Proca formalism, m_V, and reads

$$\mathcal{L}_{m_V} = \frac{1}{4}m_V^2\,\mathrm{Tr}\,(V_\mu V^\mu)\ . \tag{4.13}$$

As this term leads to a vector propagator where transversality is obtained only on-shell and one therefore suffers from non-vanishing unphysical longitudinal contributions in the loops, we will modify this ansatz in Sec. 4.2.2 such that transversality is recovered for $k \to 0$. Finally, the Yang-Mills part of the Lagrangian reads

$$\begin{aligned}\mathcal{L}_{\mathrm{YM}} &= \frac{1}{8}\mathrm{Tr}\,\{V_{\mu\nu}V^{\mu\nu}\} \\ &= \mathrm{Tr}\left\{\frac{1}{8}(\partial_\mu V_\nu - \partial_\nu V_\mu)^2 - \frac{1}{4}g^2V_\mu V_\nu[V_\mu, V_\nu] - \frac{1}{2}\mathrm{i}g\partial_\mu V_\nu[V_\mu, V_\nu]\right\}\ . \end{aligned} \tag{4.14}$$

Here, the first term represents the standard kinetic term for gauge fields, the latter terms represent self-interactions of the vector mesons and are non-vanishing due to the non-Abelian gauge group.

These contributions expressed in terms of the physical fields $\vec{\rho}_\mu$ and $\vec{a}_{1,\mu}$ can be found in App. B.2.

Fermionic part of the Lagrangian

From the perspective of QCD, for decreasing energy scales the increasing strength of the strong coupling α_s leads to strong two-quark-two-antiquark correlations of the form $\lambda_i(\bar{\psi}T_i\psi)^2$ with effective coupling $\lambda_i \propto \alpha_\mathrm{s}^2$ and tensor structure T_i, cf. the *Nambu–Jona-Lasinio model* (NJL). Here, divergent couplings λ_i signal the formation of bound states or resonances in these quark-antiquark scattering channels.

Within this low-energy model we explicitly introduce the mesons as effective degrees of freedom which can be done by means of a Hubbard-Stratonovich transformation, and identifiy the scale of this bosonization to be the UV cutoff Λ in our FRG framework. To describe the dynamical formation of mesons starting from QCD, one can use the method of dynamical hadronization, done for example in [71, 121, 133].

After bosonizing the quark-antiquark sector, the fermionic part of the Lagrangian reads [41]

$$\mathcal{L}_{\mathrm{gLSM}}^{\mathrm{ferm}} = \bar{\psi}\left(\partial\!\!\!/ - \mu\gamma_0 + h_S\left(\sigma + \mathrm{i}\vec{\tau}\vec{\pi}\gamma_5\right) + \mathrm{i}h_V\left(\gamma_\mu\vec{\tau}\vec{\rho}^{\,\mu} + \gamma_\mu\gamma_5\vec{\tau}\vec{a}_1^{\,\mu}\right)\right)\psi\,. \tag{4.15}$$

Beside the usual kinetic term and the inclusion of the quark chemical potential μ we have an interaction term to the scalar mesons via the Yukawa coupling h_S and an interaction term to the vector and axial-vector mesons via the Yukawa coupling

h_V. As we are only interested in qualitative features of this model, we do not take into account the scale-dependence of these Yukawa couplings, we rather set $h_S = h_V$ which is a good approximation as shown in [121]. In a strict gauge symmetry the coupling would have to be replaced by $h_V = g/2$, cf. Sec. 4.3.1.

Effective average action of the gLSM

Putting all contributions of the Lagrangian together we can write down an ansatz for the effective average action of the gauged linear sigma model with quarks in the LPA ansatz, given by

$$\begin{aligned}\Gamma_k = \int d^4x \Big\{ & \bar{\psi}\left(\partial\!\!\!/ - \mu\gamma_0 + h_S\left(\sigma + \mathrm{i}\vec{\tau}\vec{\pi}\gamma_5\right) + \mathrm{i}h_V\left(\gamma_\mu\vec{\tau}\vec{\rho}^{\,\mu} + \gamma_\mu\gamma_5\vec{\tau}\vec{a}_1^{\,\mu}\right)\right)\psi \\ & + U_k(\phi^2) - c\sigma + \frac{1}{2}(\partial_\mu\phi)^2 + \frac{1}{8}\mathrm{Tr}\left(\partial_\mu V_\nu - \partial_\nu V_\mu\right)^2 \\ & - \mathrm{i}gV_\mu\phi\partial_\mu\phi - \frac{1}{2}g^2\left(V_\mu\phi\right)^2 + \frac{1}{4}m_{V,k}^2\mathrm{Tr}\left(V_\mu V_\mu\right) \\ & - \frac{1}{4}g^2V_\mu V_\nu[V_\mu, V_\nu] - \frac{1}{2}\mathrm{i}g\partial_\mu V_\nu[V_\mu, V_\nu]\Big\} + \Delta\Gamma_{\pi a_1}\,. \end{aligned} \tag{4.16}$$

On this level, the effective potential U_k and the vector meson bare mass $m_{V,k}^2$ are the only scale-dependent quantities. In this work the gauge coupling g is kept scale-independent which is a good approximation in order to capture the main relevant features for the description of the ρ and a_1 meson in terms of spectral functions [121].

If chiral symmetry is spontaneously broken, the mesonic field acquires a non-vanishing expectation value $\phi_0 = (\sigma_0, \vec{0})^\top$ which leads to an additional term in the effective average action of the form

$$-\int_x g\,\sigma_0\,\vec{a}_1^{\,\mu}\cdot\partial_\mu\vec{\pi}\,. \tag{4.17}$$

This is referred to as π-a_1 *mixing* in the literature and leads to off-diagonal elements in the meson propagator. In this work we eliminate this mixing and thus diagonalize the meson propagator by redefining the a_1 field in the following form,

$$\vec{a}_1^{\,\mu} \longrightarrow \vec{a}_1^{\,\mu} + \frac{g\sigma_0}{m_{V,k}^2 + g^2\sigma_0^2}\,\partial_\mu\vec{\pi}\,. \tag{4.18}$$

All terms which arise due to this redefinition on the level of the effective average action are summarized in $\Delta\Gamma_{\pi a_1}$ in Eq. (4.16). This shift of the a_1 field also generates new momentum-dependent coupling terms in the vertex functions $\Gamma_k^{(3)}$ and $\Gamma_k^{(4)}$ and modifies the wavefunction renormalization factors of the sigma and the pions. For explicit expressions for the relevant vertex functions we refer to App. B.2.

4.2.2 Vector Meson Propagators within the FRG

We will now address the question of how to describe massive spin-1 fields within an effective theory which is known to be problematic [122, 123]. While in the Proca formalism, adopted in Sec. 4.2.1, transversality of the corresponding Green functions is guaranteed only on-shell, taking the Stueckelberg limit in the Stueckelberg formalism produces spurious massless single-particle contributions in the vector Green functions.

In this work we go a somewhat different way and describe fluctuations due to (axial-)vector mesons within the FRG framework as single-particle contributions to the corresponding conserved vector-current correlation functions. This discussion can thereby be split into two parts. We start by giving a brief review regarding covariant T-products based on [123] and will then discuss how to implement this idea into the FRG framework in order to end up with a physically reasonable transverse vector meson propagator in the limit $k \to 0$.

Covariant T-products

The issue of defining covariant time-ordered products of vector or higher-rank tensor field operators is known for a long time already [134, 135]. In the following we consider the simple case of a conserved $U(1)$ current j_μ as done in [123]. Given such a conserved current j_μ, the naive attempt of defining a T-product

$$\langle T_{\text{naiv}}\, j_\mu(x) j_\nu(0)\rangle = \theta(x^0)\, \langle j_\mu(x) j_\nu(0)\rangle + \theta(-x^0)\, \langle j_\nu(0) j_\mu(x)\rangle \,, \tag{4.19}$$

does not result in a covariant quantity. One rather has to add an additional non-covariant term $\tau_{\mu\nu}(x)$, called *sea-gull* term, to render this naive T_{naiv}-product covariant, denoted by T_{cov},

$$\langle T_{\text{cov}}\, j_\mu(x) j_\nu(0)\rangle = \langle T_{\text{naiv}}\, j_\mu(x) j_\nu(0)\rangle + \tau_{\mu\nu}(x)\,. \tag{4.20}$$

Such an additional sea-gull term always has to appear if the corresponding equal-time commutators between different current components contain a Schwinger term, first encountered by Schwinger [136]. In the present case this equal-time commutator reads

$$\langle [j_0(x), j_k(y)]\rangle \big|_{x^0=y^0} = \mathrm{i}\partial_k \delta^3(\vec{x}-\vec{y}) \int_0^\infty ds\, \frac{\rho(s)}{s}\,, \tag{4.21}$$

where $\rho(s)$ is the spectral function of the current-current correlators. The requirement that Schwinger terms are canceled in the Ward identities then fixes the sea-gull term uniquely [137] which is in the present case given by

$$\tau_{\mu\nu}(x) = \mathrm{i}(g_{\mu 0} g_{\nu 0} - g_{\mu\nu})\delta^4(x) \int_0^\infty ds\, \frac{\rho(s)}{s}\,. \tag{4.22}$$

The explicit spectral representation of the causal Greens function with covariant time-ordered product is then given by

$$\langle T_{\text{cov}}\, j_\mu(x) j_\nu(0)\rangle = -\mathrm{i} \int ds\, \frac{\rho(s)}{s} \int \frac{d^4p}{(2\pi)^4}\, \mathrm{e}^{-\mathrm{i}kp}\, \frac{p^2 g_{\mu\nu} - p_\mu p_\nu}{p^2 - s + \mathrm{i}\epsilon}\,. \tag{4.23}$$

For a semi-positive spectral function $\rho(s)$, this expression is manifestly transverse and covariant. In order to translate this spectral function of a $U(1)$ current to the spectral function of a vector field V_μ we assume a first-order interaction of these two, $g_V j_\mu V^\mu$, and find the relation $g_V^2 \rho(s) = s^2 \rho_V(s)$. Using this relation, a massive stable vector meson with mass m_V would contribute with strength Z to the spectral function

$$\rho(s) = Z\, \frac{m_V^4}{g_V^2}\, \delta(s - m_V^2) + \dots\,. \tag{4.24}$$

Together with a current-field identity of the form

$$j_\mu(x) = \frac{m_V^2}{g_V} V_\mu(x)\,, \tag{4.25}$$

we arrive at a vector meson propagator $D^V_{\mu\nu}$ in Minkowski space-time which has a single-particle contribution of the form

$$D^V_{\mu\nu} = -\mathrm{i}\frac{Z}{m_V^2}\frac{p^2 g_{\mu\nu} - p_\mu p_\nu}{p^2 - m_V^2 + \mathrm{i}\epsilon} + \dots\,. \tag{4.26}$$

This propagator is purely transverse and does not have massless single-particle contributions and therefore differs from the one obtained within Proca or Stueckelberg approaches.

In the FRG, the introduction of a regulator function $R_k(p)$ and the necessity of ensuring the invertibility of the propagator in general gives rise to modified Ward identities (mWI) [138]. We will therefore use an ansatz for fluctuating vector mesons which contains additional longitudinal contributions that vanish in the limit $k \to 0$ such that we recover the propagator from Eq. (4.26) at the IR scale. This ansatz will be the subject of the following part.

FRG formulation of massive vector mesons

In order to implement the propagator for single-particle contributions of massive vector mesons into the FRG framework, we first write down the Euclidean counterpart of Eq. (4.26) in momentum space, see App. A for the used conventions,

$$D^{\mathrm{E},V}_{\mu\nu}(p) = \frac{Z}{m_V^2}\frac{-p^2}{p^2 + m_V^2}\,\Pi^T_{\mu\nu}(p)\,, \tag{4.27}$$

with transverse projector $\Pi^T_{\mu\nu}(p) = (\delta_{\mu\nu} - p_\mu p_\nu)/p^2$. In the FRG calculations we also need the corresponding two-point function given by the inverse of the Euclidean propagator. We therefore add a Stueckelberg part to the effective average action given in Eq. (4.16), as done for example in [120, 132]. The part of the ansatz for the effective average action which is quadratic in the vector fields is then given by

$$\Delta\Gamma_k = \int d^4x \left\{ \frac{1}{8}\,\mathrm{Tr}(\partial_\mu V_\nu - \partial_\nu V_\mu)^2 + \frac{1}{4} m_V^2\,\mathrm{Tr}\,(V_\mu V^\mu) + \lambda_k\,\mathrm{Tr}\,(\partial_\mu V^\mu)^2 \right\}. \tag{4.28}$$

where then the corresponding LPA-like ansatz for the vector meson two-point function reads

$$\begin{aligned}\Gamma^{(2),\mathrm{E}}_{\mu\nu,k}(p) =& (p^2 + m^2_{V,k})\,\Pi^T_{\mu\nu}(p) \\ &+ (\lambda_k\, p^2 + m^2_{V,k})\,\Pi^L_{\mu\nu}(p),\end{aligned} \tag{4.29}$$

with Stueckelberg parameter λ_k and longitudinal projector $\Pi^L_{\mu\nu}(p) = p_\mu p_\nu / p^2$.

Using this ansatz leads to non-vanishing unphysical longitudinal contributions of the vector meson propagators inside the loops of the flow equations which eventually gives rise to considerable negative contributions to the associated spectral functions. To fix this issue, we go beyond the usual LPA truncation and include scale- and

momentum-dependent wavefunction renormalization factors $Z_k^T(p^2)$ and $Z_k^L(p^2)$ in the ansatz for the Euclidean vector meson two-point function which then reads

$$\begin{aligned}\Gamma^{(2),\mathrm{E}}_{\mu\nu,k}(p) =& Z_k^T(p^2)\,(p^2+m_{V,k}^2)\,\Pi^T_{\mu\nu}(p)\\ &+\lambda_k\, Z_k^L(p^2)\,(p^2+m_{V,k}^2/\lambda_k)\,\Pi^L_{\mu\nu}(p)\,.\end{aligned} \tag{4.30}$$

In order to ensure that the corresponding propagator is purely transverse at the IR scale, i.e. that the following modified Ward identity is fulfilled

$$p_\mu D^{\mu\nu}_{k\to 0} = 0\,, \tag{4.31}$$

we choose a Stueckelberg parameter λ_k that starts at some finite value at the UV scale Λ and tends to zero in the limit $k\to 0$. In this way the longitudinal fluctuations with mass $m_{V,k}^2/\lambda_k$ diverge at the IR scale and hence decouple completely. More explicitly, we choose

$$\lambda_k = \frac{k^2}{\Lambda^2}, \qquad \text{with} \quad \lambda_\Lambda = 1,\ \lambda_k \xrightarrow{k\to 0} 0\,. \tag{4.32}$$

Moreover, we require the longitudinal wavefunction renormalization factor to cancel the Stueckelberg parameter in front of the longitudinal term, which can be accomplished by setting

$$\lambda_k\, Z_k^L(p^2) = Z_k^T(p^2)\,, \tag{4.33}$$

and assuming that this transverse wavefunction renormalization factor is independent of λ_k. With this setting, the longitudinal and transverse part of the vector meson two-point function coincide at the UV cutoff $k=\Lambda$ and we hence have a two-point function that is proportional to $\delta_{\mu\nu}$. When lowering the scale k, the longitudinal fluctuations get heavier and heavier compared to the transverse ones and finally switch themselves off automatically in the limit $k\to 0$. In this limit we are left with a purely transverse vector meson propagator. In order to ensure that this transverse part equals the desired single-particle contribution to the vector meson propagator as given in Eq. (4.27), we set

$$Z_k^T(p^2) = -Z_k^{-1}\, m_{V,k}^2/p^2 \equiv -m_{0,k}^2/p^2\,, \tag{4.34}$$

where we introduced the mass parameter $m_{0,k}$ which for $Z_k \le 1$ is expected to be larger than the vector meson mass $m_{V,k}$. The ordering $m_{0,k}\ge m_{V,k}$ will be checked explicitly in the numerical calculation in the next section, Sec. 4.2.3. However, at the UV scale we start with the initial condition $m_{V,\Lambda} = m_{0,\Lambda}$ which corresponds to $Z=1$. We finally obtain the following single-particle contribution to the Euclidean vector meson propagator

$$D^{\mathrm{E}}_{\mu\nu,k}(p) = \frac{-p^2}{m_{0,k}^2}\,\frac{1}{(p^2+m_{V,k}^2)}\,\Pi^T_{\mu\nu}(p) + \frac{-p^2}{m_{0,k}^2}\,\frac{1}{(p^2+\frac{\Lambda^2}{k^2}m_{V,k}^2)}\,\Pi^L_{\mu\nu}(p)\,. \tag{4.35}$$

In the limit $k\to 0$ the Ward identity from Eq. (4.31) is recovered where the longitudinal part completely decouples. With the inclusion of the wavefunction renormalization factor from Eq. (4.34) the transverse part of the propagator then has the

desired form as in Eq. (4.27). This treatment can be seen as an analogy to the LPA′ truncations for the (pseudo-)scalar sector in the literature.

At this point we note that the strength of the suppression of the longitudinal fluctuations can be further influenced by choosing the Stueckelberg parameter at the UV scale λ_Λ in a different way compared to the rather natural choice of $\lambda_\Lambda = 1$. Especially in later calculations at finite temperature we scaled this initial value by a factor of 5-10 in order to ensure that these longitudinal fluctuations are suppressed also on all intermediate k-scales. However, we checked explicitly that the precise value of λ_Λ does not affect the results. More details like the inclusion of a regulator function within this setting can be found in App. B.

4.2.3 Flow of the Euclidean Particle Masses

We now want to present first results for the RG flow of the Euclidean particle masses of the scalar mesons, the vector mesons and the quarks obtained by applying the FRG framework to the above presented setting. These Euclidean masses represent the basis for the calculation of spectral functions in Chapter 5.

The masses of the scalar mesons and the quarks are obtained by solving the flow equation for the effective potential of the quark-meson model given in Eq. (3.9) and are defined in Eqs. (3.11-3.13). As we will see, the vector mesons decouple from the flow as they are always heavier compared to the actual scale k and can therefore be neglected in the Euclidean flow of the effective potential.

The Euclidean masses of the vector and axial-vector meson are in the present framework defined as

$$m^2_{\rho,k} = m^2_{V,k}\,, \qquad\qquad m^2_{a_1,k} = m^2_{V,k} + g^2\phi_0^2\,, \tag{4.36}$$

and can, together with the mass parameter $m_{0,k}$, be computed by solving the particular flow equations obtained by projecting on the flow equation for the ρ meson two-point function, cf. App. B.3 and see Fig. 5.7 for the contributing terms.

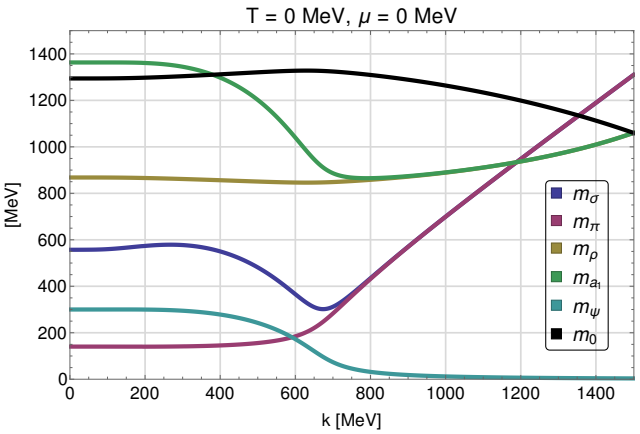

Figure 4.2: Flow of the Euclidean particle masses and of the mass parameter $m_{0,k}$ as a function of the RG-scale k in the vacuum.

The resulting scale-dependent quantities are shown in Fig. 4.2. Here we note that in contrast to later calculations where only the IR scale is relevant, we used a scale-dependent minimum in field space $\sigma_0 = \sigma_{0,k}$ in this calculation in order to interpret the k-dependent quantities on all intermediate scales. Starting at the UV cutoff $\Lambda = 1500$ MeV where chiral symmetry is restored, the masses of the chiral partners π-σ and ρ-a_1 are degenerate, the quark mass has its very small current value. Taking fluctuations into account by lowering the scale k, the mass parameter $m_{0,k}$ immediately splits from its counterpart $m_{V,k}$ and the relation $m_{0,k} \geq m_{V,k}$ stated in Sec. 4.2.2 clearly holds during the complete flow.

By lowering the scale further, the fermionic fluctuations drive the minimum away from zero towards the chirally broken phase with non-vanishing order parameter σ_0. This also leads to a mass splitting of the chiral partners and to a finite constituent quark mass, starting at around $k_\chi \approx 700$ MeV. The mass of the ρ meson remains approximately constant during the complete flow, whereas the a_1 meson mass begins to rise when chiral symmetry breaking sets in. We note that the vector meson masses are always equal or larger than the RG scale and hence decouple from the Euclidean flow, already observed in [121].

The initial parameter for the vector meson mass $m_V = 1060.0$ MeV and the value of the gauge coupling $g = 11.3$ are in all calculations fixed to reproduce the phenomenologically correct values of the ρ and a_1 meson pole masses, cf. Sec. 5.2. This results in the following values for the Euclidean quantities at the IR scale $k = 40$ MeV

$$\begin{aligned} \sigma_0 &= 93.0 \text{ MeV}\,, & m_\sigma &= 557.1 \text{ MeV}\,, \\ m_\pi &= 140.4 \text{ MeV}\,, & m_\psi &= 300.0 \text{ MeV}\,, \\ m_\rho &= 868.1 \text{ MeV}\,, & m_{a_1} &= 1363.1 \text{ MeV}\,, \\ m_0 &= 1294.3 \text{ MeV}\,. \end{aligned} \tag{4.37}$$

The values for m_ρ, m_{a_1} and m_0 can differ from these ones if we do not evaluate their flow equations at the k-dependent minimum but at the IR minimum, as it will be done to determine the IR-masses at finite temperature and chemical potential serving as input for the computation of spectral functions in Sec. 5.2.

4.3 Extensions of the Model

4.3.1 Introducing the Photon Field

In order to get access to the electromagnetic interaction within the gauged linear sigma model, for example to calculate electromagnetic spectral functions and dilepton rates, an important extension is the inclusion of the electromagnetic field A_μ to this model.

In the phenomenological vector meson dominance model of Sakurai, the photon field couples only to the charge neutral third component of the iso-triplet $\vec{\rho}$, accomplished by the following additional term in the Lagrangian,

$$\mathcal{L}_{\gamma\rho}^{\text{Sakurai}} = -\frac{e m_\rho^2}{g} \rho_\mu^3 A^\mu \,. \tag{4.38}$$

Note that in this model, interactions between the photon and charged particles are not considered. Obviously, this interaction term is not invariant under $U(1)$ gauge transformations. In contrast, Kroll, Lee and Zumino (KLZ) [127] proposed an approach where the photon couples to the charged pion components within the idea of $U(1)$ gauge invariance, i.e. by extending the covariant derivative in Eq. (4.9) in the form

$$\mathcal{L}_{\gamma\pi}^{\mathrm{KLZ}} = (D_\mu - \mathrm{i}eA_\mu T_3)\,\vec{\pi}\,. \tag{4.39}$$

The interaction of the photon field to the ρ meson is in the *KLZ* model introduced via the field strength tensors of these two,

$$\mathcal{L}_{\gamma\rho}^{\mathrm{KLZ}} = -\frac{e}{2g}\rho_{\mu\nu}^3 F^{\mu\nu}\,, \tag{4.40}$$

with $F_{\mu\nu} = \partial_\mu A_\nu - \partial_\nu A_\mu$ being the electromagnetic field strength tensor and $\rho_{\mu\nu}^3$ the third component of the ρ field strength tensor, defined via $V_{\mu\nu} = \vec{\rho}_{\mu\nu}\cdot\vec{T} + \vec{a}_{1,\mu\nu}\cdot\vec{T}^5$. If we also define a covariant derivative for the quark fields in the spirit of KLZ,

$$D_\mu\psi = (\partial_\mu - \mathrm{i}eA_\mu Q)\,\psi\,, \tag{4.41}$$

with electromagnetic coupling e and charge matrix Q, which for $N_f = 2$ is given by $Q = \mathrm{diag}(2/3, -1/3)$, one can show that the equivalence of the γ-ρ-interaction term in the KLZ model to the one in the VMD model of Sakurai is guaranteed only if $h_V = g/2$ in our ansatz given in Eq. (4.16).

However, in this first attempt to describe the electromagnetic coupling to the gauged linear sigma model we only implement this interaction in the sense of VMD as qualitative feature and not in a strict field theoretical verification. We therefore simply replace the derivatives ∂_μ in the ansatz in Eq. (4.16) by covariant ones, as done for example in [132]. Additionally to Eq. (4.41) we therefore have

$$D_\mu\phi = (\partial_\mu - \mathrm{i}eA_\mu T_3)\,\phi\,, \tag{4.42}$$

for the scalar sector and

$$D_\mu V_\nu = \partial_\mu V_\nu - \mathrm{i}eA_\mu[T_3, V_\nu]\,, \tag{4.43}$$

for the vector mesons. The photon thus only couples to the charged particles, i.e. the first two components of $\vec{\pi}$, $\vec{\rho}$ and $\vec{a}_1$.

Putting everything together, the effective average action of the gauged linear sigma model with quarks and photon-coupling reads [43]

$$\begin{aligned}\Gamma_k = \int d^4x\Big\{&\bar{\psi}\left(\not{D} - \mu\gamma_0 + h_S\left(\sigma + \mathrm{i}\vec{\tau}\vec{\pi}\gamma_5\right) + \mathrm{i}h_V\left(\gamma_\mu\vec{\tau}\vec{\rho}^{\,\mu} + \gamma_\mu\gamma_5\vec{\tau}\vec{a}_1^{\,\mu}\right)\right)\psi \\ &+ U_k(\phi^2) - c\sigma + \frac{1}{2}\left|(D_\mu - \mathrm{i}gV_\mu)\phi\right|^2 + \frac{1}{8}\mathrm{Tr}\left(V_{\mu\nu}V^{\mu\nu}\right) + \frac{1}{4}m_{V,k}^2\mathrm{Tr}\left(V_\mu V^\mu\right)\Big\}\,,\end{aligned} \tag{4.44}$$

with modified field strength tensor $V_{\mu\nu} = D_\mu V_\nu - D_\nu V_\mu - \mathrm{i}g\,[V_\mu, V_\nu]$. As we are only interested in the electromagnetic interaction with the other particles in the model, we omit the field strength tensor for the photon field in this ansatz.

Within this extended model we have non-vanishing $\Gamma^{(3)}_{\pi\pi A_\mu}$ and $\Gamma^{(3)}_{\psi\bar{\psi}A_\mu}$ vertices which enables us to compute electromagnetic two-point functions and the corresponding spectral functions, done in [43] and Sec. 5.3. More explicit expressions among other things for these vertices are listed in App. B.2.

4.3.2 Gauged Linear Sigma Model with Nucleons

Another phenomenological improvement of the gLSM is the inclusion of baryon degrees of freedom. On the one hand this would enable to describe phenomenologically important vector meson-nucleon scattering processes, on the other hand, by replacing the quark fields with nucleon fields one could bypass the problem of unphysical quark-antiquark decay thresholds in the vacuum seen in mesonic spectral functions in quark-meson-type models and already discussed in Sec. 3.2.3. In this way we end up with a purely hadronic low-energy model where now all degrees of freedom and the associated processes are physically realized in the hadronic phase.

The ansatz for the effective average action of the gLSM with nucleons follows by replacing the quark-antiquark fields in Eq. (4.16) with fields for the nucleon and its parity partner as done for the scalar sector within the parity-doublet model in Sec. 3.3. With an additional chirally invariant mass term for the nucleons it follows

$$\begin{aligned}\Gamma_k = \int d^4x \Big\{ & \bar{N}_1 \left(\partial\!\!\!/ - \mu\gamma_0 + h_{S,1}\left(\sigma + \mathrm{i}\vec{\tau}\vec{\pi}\gamma_5\right) + \mathrm{i}h_{V,1}\left(\gamma_\mu\vec{\tau}\vec{\rho}^{\,\mu} + \gamma_\mu\gamma_5\vec{\tau}\vec{a}_1^{\,\mu}\right)\right) N_1 \\ & + \bar{N}_2 \left(\partial\!\!\!/ - \mu\gamma_0 + h_{S,2}\left(\sigma - \mathrm{i}\vec{\tau}\vec{\pi}\gamma_5\right) + \mathrm{i}h_{V,2}\left(\gamma_\mu\vec{\tau}\vec{\rho}^{\,\mu} - \gamma_\mu\gamma_5\vec{\tau}\vec{a}_1^{\,\mu}\right)\right) N_2 \\ & + m_{0,\mathrm{B}}\left(\bar{N}_1\gamma_5 N_2 - \bar{N}_2\gamma_5 N_1\right) \\ & + U_k(\phi^2) - c\sigma + \frac{1}{2}(\partial_\mu\phi)^2 + \frac{1}{8}\mathrm{Tr}\left(\partial_\mu V_\nu - \partial_\nu V_\mu\right)^2 \\ & - \mathrm{i}gV_\mu\phi\partial_\mu\phi - \frac{1}{2}g^2\left(V_\mu\phi\right)^2 + \frac{1}{4}m_{V,k}^2\mathrm{Tr}\left(V_\mu V_\mu\right) + \lambda_k\,\mathrm{Tr}\left(\partial_\mu V^\mu\right)^2 \\ & - \frac{1}{4}g^2 V_\mu V_\nu [V_\mu, V_\nu] - \frac{1}{2}\mathrm{i}g\partial_\mu V_\nu [V_\mu, V_\nu]\Big\} + \Delta\Gamma_{\pi a_1}\,. \end{aligned} \tag{4.45}$$

We note the minus in the coupling of the parity partner N_2 to the pseudo-scalar and axial-vector mesons π and a_1. From this ansatz we can extract the vertices $\Gamma^{(3)}_{\bar{N}N\rho}$ and $\Gamma^{(3)}_{\bar{N}Na_1}$ which then give new contributions to the flow equations for the ρ and a_1 two-point functions. In the spectral functions these contributions give rise to a decay in nucleon pairs and to in-medium scattering processes, cf. Sec. 5.2.3.

5

Towards Realistic Vector Meson Spectral Functions

To explore the low-energy features of QCD in experiments, one possible way is to study the spectral properties of real and virtual photons emitted in heavy-ion collisions. Since they only interact electromagnetically, their measured spectrum provides undisturbed information about the space-time history of the inner structure of the fireball created in such collisions.

Due to the direct coupling of the ρ, ω and ϕ meson to such lepton pairs, the invariant mass of the dileptons reflects the mass distribution of the vector mesons at the moment of its decay. Given the in-medium spectral functions of the light vector mesons one could therefore reconstruct the dilepton rate and look for signatures for the restoration of chiral symmetry or the existence of a critical endpoint in the resulting spectra. Prerequisite for this is the phenomenologically correct description of the vector meson spectral functions at finite temperature and chemical potential, where the ρ meson plays a central role as it provides the dominant contribution.

In this chapter we now present results for the ρ and a_1 meson spectral functions obtained by applying the FRG framework to effecive models introduced in Chapter 3 and Chapter 4 using analytically continued flow equations as discussed in Sec. 2.2.2. Here, the results at finite temperature and chemical potential will enable us to study modifications and resulting signatures for the restoration of chiral symmetry and for the CEP in the used models.

We start this chapter by a brief overview concerning vector mesons, spectral functions and the connection to the QCD phase diagram in Sec. 5.1. In Sec. 5.2 we present results for vector and axial-vector spectral functions at finite temperature and chemical potential as obtained in different model settings. Results for electromagnetic spectral functions are shown and discussed in Sec. 5.3.

5.1 Introduction

Electromagnetic probes like real photons and dileptons turned out to be the ideal information carrier providing direct insights into strong-interaction matter in experiments. Since their mean free path is much larger than the typical size of the systems created in heavy-ion collisions, once produced they escape the fireball essentially unaffected and therefore carry unique information on the spectral properties of the hot and dense QCD medium. The natural candidates for this in-medium spectroscopy are the vector mesons which couple directly to the electromagnetic current and are for this reason expected to contribute significantly to the measured spectra. In the low-energy region with invariant dilepton mass $M_{ll} \leq 1$ GeV, which is substantial to study spontaneous chiral symmetry breaking, the relevant vector mesons are the light ones, $\rho(770)$, $\omega(782)$ and the $\phi(1020)$ meson.

However, photons and dileptons are emitted continuously during all stages of such a collision process [116]. The earlier they are produced, the heavier the invariant mass of the emitted dileptons is on average. All relevant sources of dileptons are illustrated in the sketch shown in Fig. 5.1a. Chronologically, the first source of dileptons in a heavy-ion collision is through Bremsstrahlung of the approaching colliding nuclei. Once these nuclei touch and overlap, processes like the Drell-Yan annihilation process, where a quark from one nucleon annihilates with an antiquark from the other one forming a lepton pair, dominate for $M_{ll} \gtrsim 3$ GeV. In the following thermalization process towards the quark-gluon-plasma (QGP) phase, the main contribution of dileptons comes from quark-antiquark annihilation processes and weak decays of the open-charm mesons D and $\bar{D}$. In the next stages, the system more and more expands and cools down, the QGP successively turns into a hadron gas

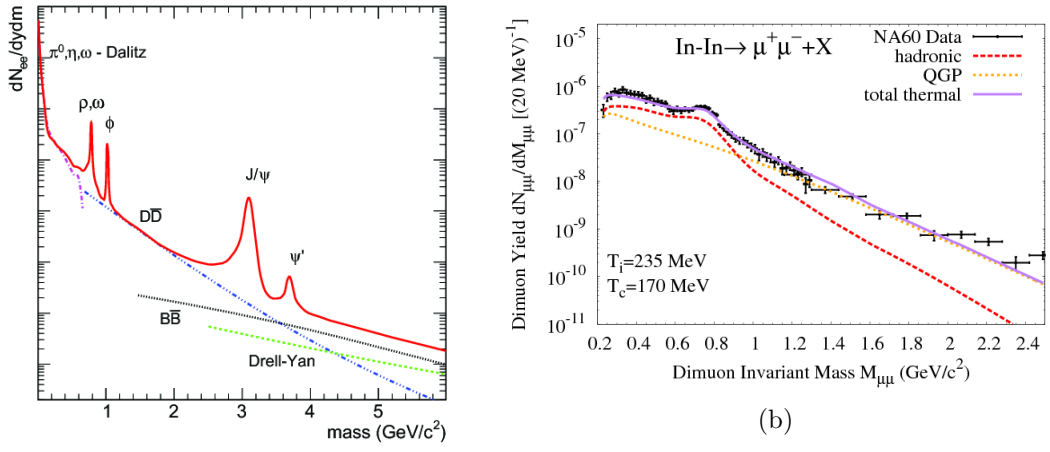

(a) (b)

Figure 5.1: Sketch of the elektron-positron mass distribution from proton-proton collisions [139] (a) and comparison of NA60 data to theoretical calculations of dimuon invariant-mass spectra from Indium-Indium collisions [140] (b).

where now dileptons are mainly produced via hadronic interactions among themselves. Here the main contribution comes through the formation of light vector mesons which directly decay into dileptons, indicated by the peaks at low invariant masses in Fig. 5.1a. During the freezeout stage the dominant dilepton sources are Dalitz decays of π^0, η or ω mesons.

In experiments, only the full space-time integrated spectra of the entire history of the fireball is accessible. In Fig. 5.1b we see an example of such a dilepton spectrum, in this case dimuons from In-In collisions, measured at the SPS [141, 142]. In these spectra one hopes to find evidences for both, the confinement-deconfinement phase transition as well as for chiral symmetry restoration. While the suppression of heavy quarkonium states like J/Ψ could signal deconfinement [143, 144], in-medium modifications of the light vector mesons could provide evidences for the restoration of chiral symmetry [145–147]. In this context, Brown and Rho suggested a dropping ρ mass as a consequence of chiral symmetry restoration [148] in order to explain the measured enhancement of the dilepton yield at invariant masses significantly below the ρ mass [149]. Another explanation for this enhancement is a broadening or melting of the ρ spectral function due to in-medium scattering effects, which seems to be the favoured scenario [150,151]. Another interesting question is how a possible critical endpoint would manifest itself in the vector meson spectral function and in the resulting dilepton spectra.

On a more formal level, the production rate of dileptons at four-momentum q can in general be expressed in terms of the electromagnetic spectral function $\mathrm{Im}\,\Pi^{\mu\nu}_{\mathrm{em}}$ and is to leading order in the electromagnetic coupling α_{em} given by [86, 147, 152]

$$\frac{dN^8_{ll}}{d^4x\,d^4q} = -\frac{\alpha^2_{\mathrm{em}}}{3\pi^3 M^2}\, f^B(q_0;T)\, g_{\mu\nu}\,\mathrm{Im}\,\Pi^{\mu\nu}_{\mathrm{em}}(M,q;\mu_B,T)\,. \tag{5.1}$$

Here, f^B denotes the Bose-Einstein distribution and $q_0^2 = M^2 + \vec{q}^{\,2}$ the energy of the lepton pair. The effects of the strong interaction are encoded in the electromagnetic spectral function which is defined as imaginary part of the retarded current-current correlation function,

$$\Pi^{\mu\nu}_{\mathrm{em}}(q) = -\mathrm{i}\int d^4x\, \mathrm{e}^{iqx}\,\theta(x_0)\,\langle j^{\mathrm{em}}_\mu(x)\, j^{\mathrm{em}}_\nu(0)\rangle_{T,\mu}\,. \tag{5.2}$$

For low invariant masses $M \leq 1$ GeV, the electromagnetic current can within the vector meson dominance model be expressed in a hadronic basis, i.e. in terms of the light vector meson fields (CFI), cf. Sec. 4.1,

$$j^{\mathrm{em}}_\mu = \frac{m^2_\rho}{g_\rho}\rho_\mu + \frac{m^2_\omega}{g_\omega}\omega_\mu + \frac{m^2_\phi}{g_\phi}\phi_\mu\,. \tag{5.3}$$

In this sense, also the electromagnetic spectral function can be expressed in terms of the vector meson spectral functions [147],

$$\mathrm{Im}\,\Pi_{\mathrm{em}} \sim \mathrm{Im}\,D_\rho + \frac{1}{9}\mathrm{Im}\,D_\omega + \frac{2}{9}\mathrm{Im}\,D_\phi\,, \tag{5.4}$$

where the ρ spectral function provides the dominant contribution.

A more convenient way of calculating the dilepton rate in the present framework is the usage of the Weldon formula [153],

$$\frac{dN_{ll}^{8}}{d^4x\, d^4q} = \frac{\alpha}{12\pi^3}\left(1+\frac{2m^2}{q^2}\right)\left(1-\frac{4m^2}{q^2}\right)^{1/2} q^2\,(2\rho_{\mathrm{em}}^{\perp}+\rho_{\mathrm{em}}^{\parallel})\,n_B(q_0)\,. \tag{5.5}$$

In this form, the dilepton production rate can be calculated in terms of the electromagnetic spectral function which can be decomposed in a part parallel and a part vertical to the heat bath [43].

With given realistic electromagnetic or vector meson spectral functions at finite temperature and chemical potential one thus has access to the associated dilepton rate and with transport simulations in principle also to the full integrated spectra and can draw conclusions how critical phenomena could manifest itself in the measured spectra. As the underlying signatures are visible in the in-medium spectral functions, we will in the following section present results for the T- and μ-dependent ρ and a_1 meson spectral functions obtained within basically three different settings, related to the used model and truncation.

5.2 Vector Meson Spectral Functions: Results

5.2.1 With Scalar Mesons and Quarks

In this first setting we solve the flow equation for the effective potential in the quark-meson model, Eq. (3.9), and then employ the Proca ansatz within the gLSM, Eq. (4.16), where in this first truncation we only implement (pseudo-)scalar mesons and quarks as fluctuating fields in the flow equations for $\Gamma_k^{(2)}$. From the resulting relevant parts of the ansatz we can then extract the flow equation for the vector meson mass $m_{V,k}^2$, an UV ansatz for the retarded vector meson two-point functions and the vertices $\Gamma^{(3)}$ and $\Gamma^{(4)}$, see [41] for this setting and App. B for explicit expressions. With this input we then solve the analytically continued flow equations for the retarded ρ and a_1 two-point functions and finally compute the respective temperature- and chemical-potential dependent spectral functions, cf. Sec. 2.2.2. The diagrammatic form of the flow equations for the ρ and a_1 two-point functions within this setting is illustrated in Fig. 5.2. On this level we can already identify which decay and capture processes can occur. For an off-shell ρ meson we have the processes

$$\rho^* \to \psi + \bar{\psi}\,, \quad \rho^* \to \pi + \pi\,, \tag{5.6}$$

and for an off-shell a_1 meson

$$\begin{aligned} &a_1^* \to \psi + \bar{\psi}\,, \quad a_1^* \to \pi + \sigma\,, \\ &a_1^* + \pi \to \sigma\,, \quad a_1^* + \sigma \to \pi\,. \end{aligned} \tag{5.7}$$

The particular processes are only possible if the energy constraints are fulfilled, namely for a decay process $\omega \geq E_\alpha + E_\beta$ and for a capture process $\omega + E_\alpha \geq E_\beta$, with ω being the total energy of an off-shell particle and $E_{\alpha/\beta}$ the energy of the involved particles.

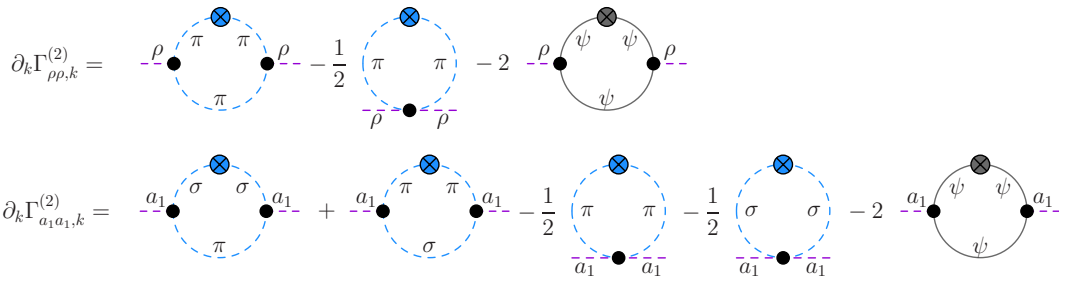

Figure 5.2: Flow equations for the ρ and a_1 two-point functions in diagrammatic form. Vertices are indicated by black dots, regulator insertions by crossed circles. The color of the lines and regulators represents the type of field: blue for scalar mesons, gray for quark-antiquarks and purple for vector mesons.

T- and μ-dependent Euclidean masses

We start by discussing the temperature- and chemical-potential dependent Euclidean particle masses which serve as input for the computation of the spectral functions.

The masses of the sigma meson, the pions and the quarks are obtained by solving the flow equation of the effective potential which is done within the setting discussed in Sec. 3.2.1. There we have the following values in the vacuum: $m_\pi = 140$ MeV, $m_\sigma = 557$ MeV and $\sigma_0 = 93$ MeV. The initial value for $m_{V,\Lambda} = 1450$ MeV as well as for the scale-independent gauge coupling $g = 11.4$ are chosen to reproduce the physical vacuum-pole masses of the ρ and a_1 meson reasonably well in the vacuum: $m^p_\rho = 789.3$ MeV and $m^p_{a_1} = 1274.7$ MeV. The resulting Euclidean masses are $m_\rho = 1298.3$ MeV and $m_{a_1} = 1676.3$ MeV. This huge discrepancy could be reduced for example by including wavefunction renormalization factors. However, there is no a priori reason for the two masses to agree, the Euclidean masses should rather be seen as parameters to fix the physical ones as they have no direct physical meaning.

In Fig. 5.3a we see the Euclidean masses of all particles as a function of temper-

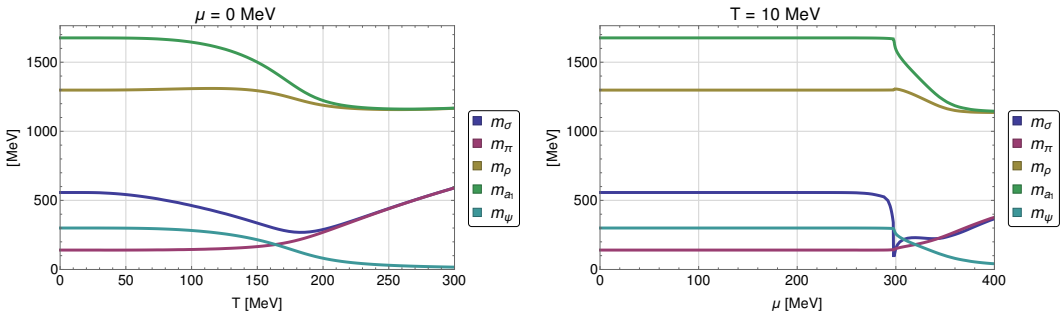

(a) (b)

Figure 5.3: Euclidean masses of all particles as a function of temperature at $\mu = 0$ MeV (a) and as a function of chemical potential across the CEP at $T = 10$ MeV (b).

ature at vanishing quark chemical potential. Starting in the chirally broken phase with the vacuum values listed above, the masses of the chiral partners are split while the quark mass has its constituent value. By increasing the temperature we see a smooth behaviour of all masses towards the phase where chiral symmetry is restored, as expected for this chiral crossover transition. This phase is characterized by an almost vanishing quark mass and degenerate masses for the chiral partners π-σ and ρ-a_1 which sets in at around $T_\chi \approx 185$ MeV. The ρ mass remains almost constant with increasing temperature, the a_1 mass slightly drops when chiral symmetry restoration sets in.

The chemical-potential dependent Euclidean masses for the same particles are shown in Fig. 5.3b as a function of chemical potential across the CEP of the quark-meson model, located at $(T_{\mathrm{CEP}}; \mu_{\mathrm{CEP}}) \approx (10; 298)$ MeV. The masses do not change over a wide range of chemical potential as expected from the Silver Blaze property [154]. Close to the CEP, the sigma mass as critical mode drops significantly and should become exactly massless when hitting the CEP precisely. In addition, the chiral condensate drops and so do the vector meson masses and the quark mass. At large chemical potentials beyond the CEP, the masses of the chiral partners coincide again and the quarks become almost massless, similar to the case of high temperature and vanishing chemical potential.

Real and imaginary part of $\Gamma^{(2),R}$

As the real and imaginary parts of $\Gamma^{(2),R}$ are solved separately we now present results for these parts and their compositions.

In Fig. 5.4a we see the real parts of the ρ and a_1 retarded two-point functions in the vacuum. As this is not a quantitative study, we estimate the pole masses of the particles by the zeros of these real parts, which is a good approximation if the width of the resonance, i.e. the imaginary part of $\Gamma^{(2),R}$, is sufficiently small. For a more

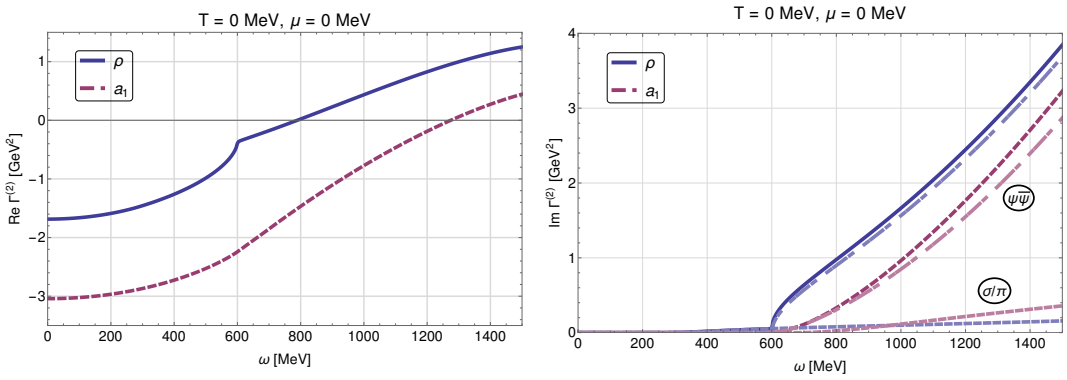

(a) (b)

Figure 5.4: Real (a) and imaginary (b) part of the retarded two-point functions of the ρ (blue) and a_1 meson (dashed red) as a function of external energy ω at $T = \mu = 0$ MeV. The imaginary part is splitted into the fermionic contributions (upper light dashed lines) and the mesonic contributions (lower light dashed lines).

precise determination of these pole masses one has to study the analytic structure of $\Gamma^{(2),R}$ and look for poles on the second Riemann sheet, see for example [155].

The imaginary parts of $\Gamma^{(2),R}$, shown in Fig. 5.4b, are non-vanishing if a process becomes energetically possible. For the ρ meson the imaginary part begins at $\omega = 2m_\pi \approx 280$ MeV, for the a_1 meson at $\omega = 2m_\psi \approx 600$ MeV. To see how the particular processes contribute to the full imaginary part, these different contributions are plotted separately in Fig. 5.4b. As we see, for both particles the imaginary part related to the quark-antiquark decay clearly dominates over the mesonic decay processes, even in the vacuum where physically this process should not be possible at all. However, this decay process is naturally present in the current setting as there is no mechanism which describes confinement. It therefore needs further investigations of how to suppress or even disable such quark-antiquark processes in the confined phase of the phase diagram.

In-medium spectral functions

We now discuss the in-medium ρ and a_1 meson spectral functions at vanishing external spatial momentum as a function of external frequency ω, shown in logarithmic scales in Fig. 5.5.

In the vacuum, the $\rho^* \to \pi + \pi$ decay gives rise to non-vanishing values in the ρ spectral function for $\omega \gtrsim 280$ MeV. A further increase can be seen starting at $\omega \approx 600$ MeV related to the decay into a quark-antiquark pair. The a_1 spectral function begins to rise at $\omega \approx 600$ MeV, when a decay into a quark-antiquark becomes energetically possible, it further increases due to the mesonic decay channel $a_1^* \to \pi + \sigma$. The large contribution of the quark-antiquark decay channel leads to a broad structure of both spectral functions.

By increasing the temperature (left column in Fig. 5.5), the a_1 meson can capture a pion from the heat bath forming a sigma meson, $a_1^* + \pi \to \sigma$. This process is possible when $\omega = E_{\sigma,k} - E_{\pi,k}$, i.e. if the difference of the scale-dependent energies equals the external frequency ω and is therefore bounded by $\omega \leq m_\sigma - m_\pi$ giving rise to an increase of the a_1 spectral function in this ω-region. On scales where the difference $E_{\sigma,k} - E_{\pi,k}$ flows through an (approximate) saddle point, the spectral function develops a pronounced peak analogous to a van Hove singularity in the density of states in the electronic band-structure of solids. This effect can be seen in the a_1 spectral function on the left side in Fig. 5.5 for $T = 100$ MeV and $T = 150$ MeV. As with a further increase of the temperature the difference of the sigma and the pion mass tends to zero, cf. Fig. 5.3a, this capture-threshold moves to smaller energies.

For temperatures above the crossover, the quark mass and the related quark-antiquark decay threshold drops significantly, the masses of the chiral partners π-σ and ρ-a_1 become more and more degenerate. This also leads to the degeneracy of the mesonic decay processes $\rho^* \to \pi + \pi$ and $a_1^* \to \pi + \sigma$. Furthermore, the quarks become the lightest degrees of freedom and give the dominant contribution to both spectral functions. All these effects lead to a strong broadening and finally a complete degeneration of the ρ and a_1 meson spectral functions which can be directly linked to the restoration of chiral symmetry.

The chemical-potential dependent spectral functions of the ρ and a_1 meson at $T = 10$ MeV are shown on the right side in Fig. 5.5. As expected from the Silver Blaze property, both spectral functions remain almost unchanged from $\mu = 0$ MeV to

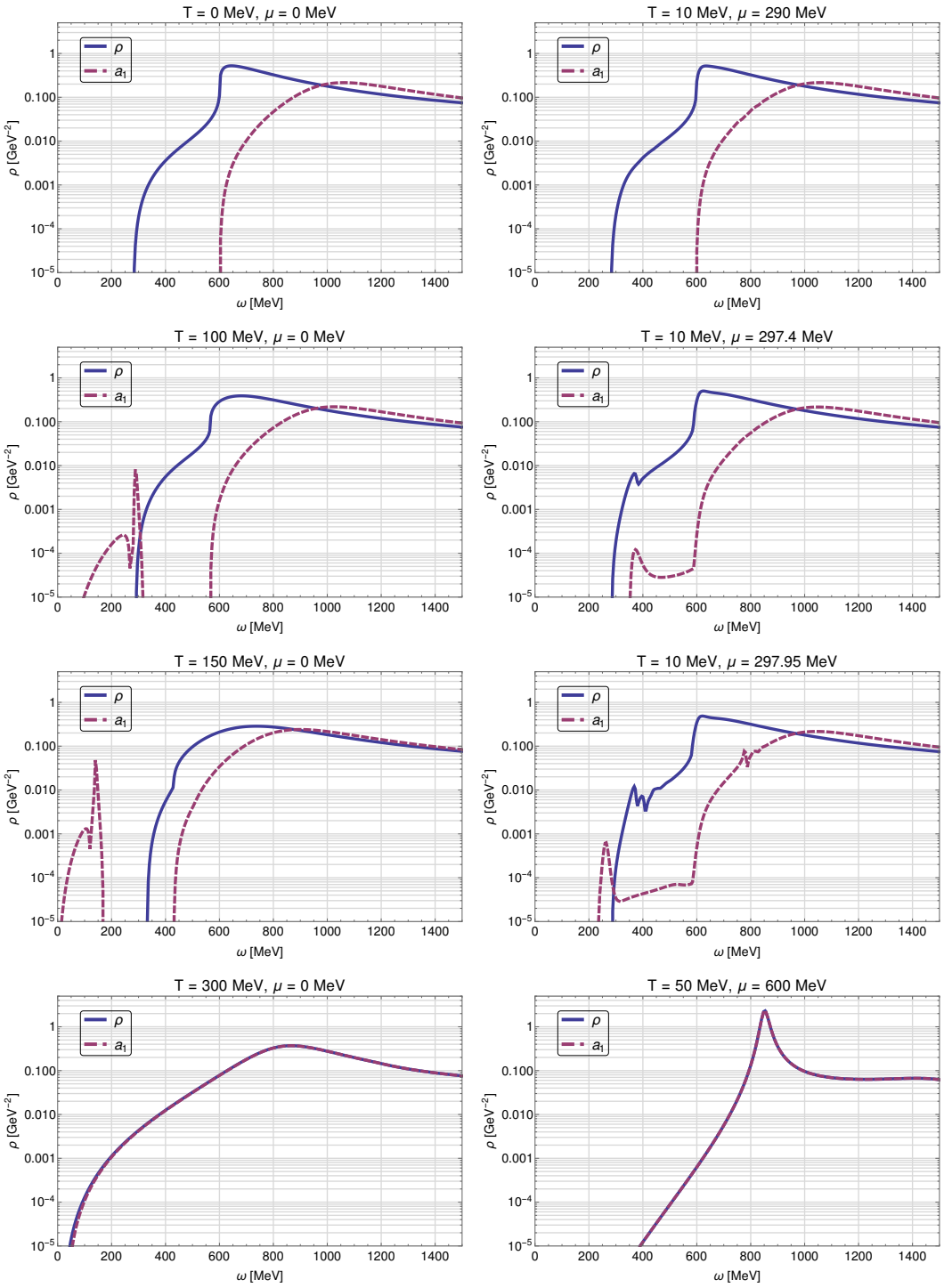

Figure 5.5: Spectral functions of the ρ (blue) and a_1 meson (dashed red) as a function of external frequency ω for increasing temperature at $\mu = 0$ MeV (left column) and for increasing chemical potential along the axis of the CEP at $T = 10$ MeV (right column).

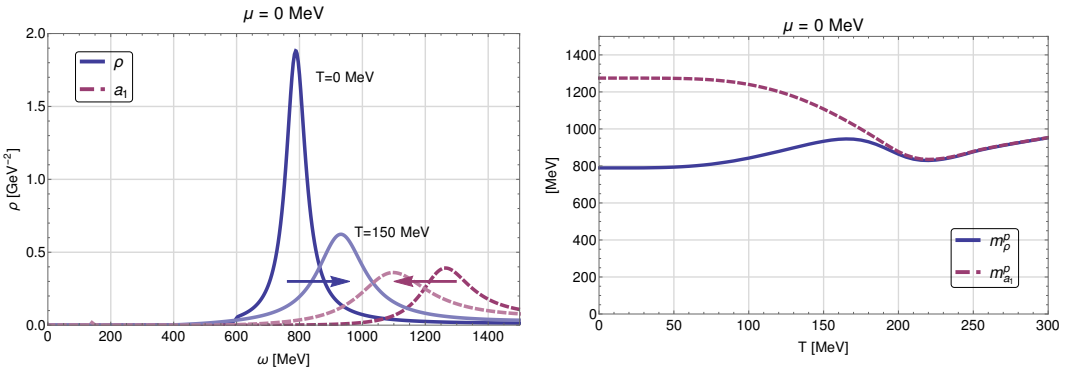

(a) (b)

Figure 5.6: Spectral functions of the ρ (blue) and a_1 meson (dashed red) at $T = 0$ MeV (darker color) and $T = 150$ MeV (lighter color) for $\mu = 0$ MeV without quark-antiquark decay channel plotted in linear scales (a) and temperature-dependent pole masses of the ρ (blue) and a_1 meson (dashed red) (b).

values close to the CEP, already mentioned for the associated μ-dependent Euclidean masses. However, from $\mu = 297.4$ MeV on we observe sensitive modifications in the a_1 spectral function induced by the dropping sigma mass near the CEP. As a consequence, the threshold of the process $a_1^* \to \pi + \sigma$ moves significantly towards lower energies and should be located at the pion mass when hitting the CEP exactly, which is difficult in a numerical calculation. On the other hand, the ρ spectral function shows only small μ-induced modifications. At large chemical potential we again see full degeneracy of the ρ and the a_1 spectral functions. Here we note that we choose $T = 50$ MeV and $\mu = 600$ MeV to avoid the thermodynamically problematic regime on the right side of the first order line, already discussed in Sec. 3.2.2.

In Fig. 5.6a we again see the temperature-induced effects on the ρ and a_1 spectral functions plotted in linear scales, where in this plot the imaginary parts of the quark-antiquark decays were disabled by hand. With increasing temperature, the peaks of both spectral functions move to each other and at the same time strongly broaden. This can also be observed by looking at the T-dependent pole masses, shown in Fig. 5.6b, which basically equal the position of the peaks in the spectral functions. Starting with the vacuum values $m_\rho^p = 789.3$ MeV and $m_{a_1}^p = 1274.7$ MeV, both pole masses slightly move to each other until they become degenerate at $T \approx 200$ MeV, as a consequence of chiral symmetry restoration. Our results are thus consistent with the melting-ρ-scenario, where the ρ mass remains almost constant and the a_1 mass shifts towards the mass of the ρ meson [147, 156].

5.2.2 Fluctuating Vector Mesons

We now improve the setting from Sec. 5.2.1 by including fluctuating (axial-)vector mesons in the flow of $\Gamma_k^{(2)}$. Therefore we use the formalism discussed in Sec. 4.2.2, namely the ansatz from Eq. (4.16) together with the Stueckelberg part given in Eq. (4.28), and will as in the previous setting neglect vector meson self-interactions

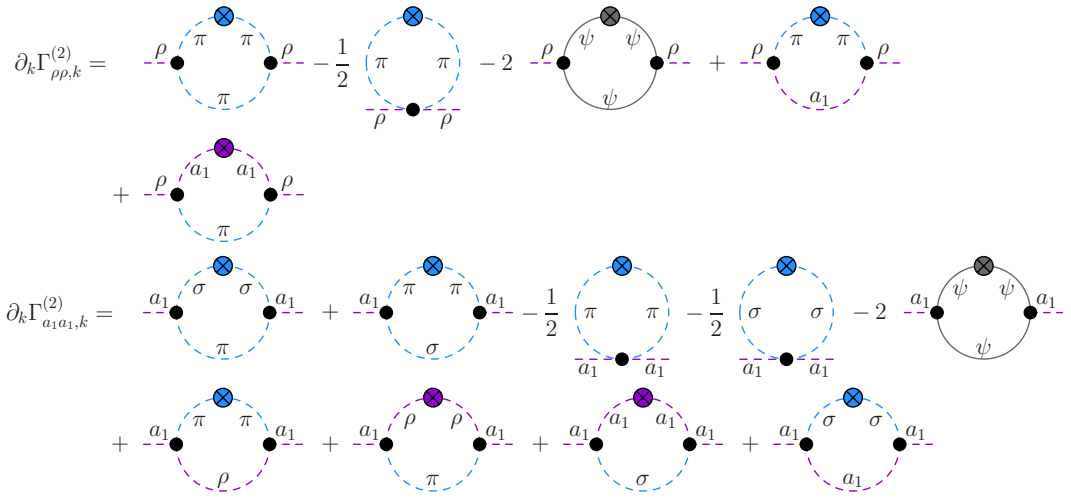

Figure 5.7: Flow equations for the ρ and a_1 two-point functions in diagrammatic form. Vertices are indicated by black dots, regulator insertions by crossed circles. The color of the lines and regulators represents the type of field: blue for scalar mesons, gray for quark-antiquarks and purple for vector mesons.

maintaining only the Abelian part of the gLSM ansatz. This results in non-vanishing $\Gamma^{(3)}_{a_1\rho\pi}$ and $\Gamma^{(3)}_{a_1 a_1 \sigma}$ vertices and the vector meson propagator given in Eq. (4.35).

While we use the same input from the effective potential as above, we now have new flow equations for the vector meson mass $m^2_{V,k}$ and for $m^2_{0,k}$ as new k-dependent quantity. The diagrammatic form of the flow equations for the ρ and a_1 two-point functions is shown in Fig. 5.7. Possible processes for an off-shell ρ meson are now

$$\begin{aligned} &\rho^* \to \psi + \bar{\psi}\,, \quad \rho^* \to \pi + \pi\,, \\ &\rho^* \to a_1 + \pi\,, \quad \rho^* + \pi \to a_1\,, \quad \rho^* + a_1 \to \pi\,, \end{aligned} \tag{5.8}$$

and for an off-shell a_1 meson

$$\begin{aligned} &a_1^* \to \psi + \bar{\psi}\,, \\ &a_1^* \to \pi + \sigma\,, \quad a_1^* + \pi \to \sigma\,, \quad a_1^* + \sigma \to \pi\,, \\ &a_1^* \to \rho + \pi\,, \quad a_1^* + \pi \to \rho\,, \quad a_1^* + \rho \to \pi\,, \\ &a_1^* \to a_1 + \sigma\,, \quad a_1^* + \sigma \to a_1\,, \quad a_1^* + a_1 \to \sigma\,. \end{aligned} \tag{5.9}$$

Due to the new vertices, we thus have decay channels involving the ρ and a_1 meson, $\rho^* \to a_1 + \pi$, $a_1^* \to \rho + \pi$ and $a_1^* \to a_1 + \sigma$ as well as related capture processes, now also for the ρ meson.

T- and μ-dependent Euclidean masses

The temperature and chemical-potential dependent Euclidean particle masses within this setting are shown in Fig. 5.8. As the input from the effective potential is

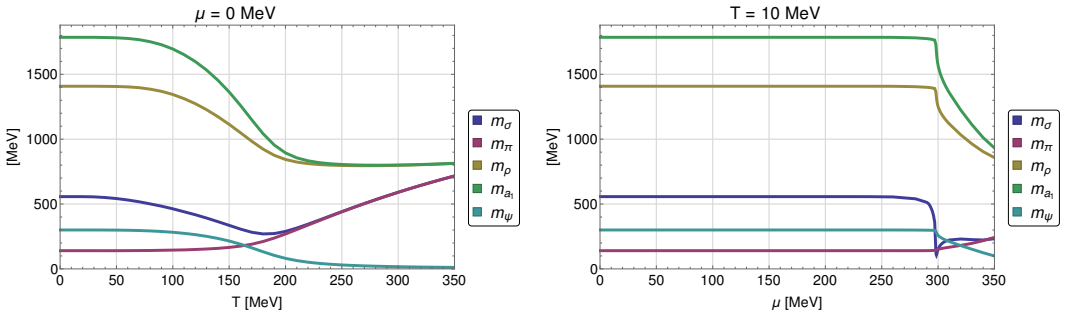

(a) (b)

Figure 5.8: Euclidean masses of all particles as a function of temperature at $\mu = 0$ MeV (a) and as a function of chemical potential across the CEP at $T = 10$ MeV (b).

the same as in Sec. 5.2.1, only the vector meson masses m_ρ and m_{a_1} change in comparison to Fig. 5.3. In this calculation, we again fixed the initial value of $m_{V,\Lambda} = m_{0,\Lambda} = 1060.0$ MeV and $g = 11.3$ to reproduce reasonable values for the ρ and a_1 pole masses: $m_\rho^p = 776.3$ MeV and $m_{a_1}^p = 1242.6$ MeV. This results in Euclidean vector meson masses in this case of $m_\rho = 1408.1$ MeV and $m_{a_1} = 1785.3$ MeV, which are even larger than in the previous setting.

The T- and μ-dependence of these masses is similar to Fig. 5.3. Starting in the vacuum, the masses of the ρ and a_1 meson are split. By increasing the temperature both masses drop and become degenerate for $T \gtrsim 230$ MeV as a consequence of the restoration of chiral symmetry, as can be seen in Fig. 5.8a. As a difference, the slope of the masses in this case is more enhanced than in Fig. 5.3a. As a function of μ, the masses m_ρ and m_{a_1} do not change until μ-values close to the CEP, where both masses significantly drop and for very large chemical potentials again become degenerate.

In this setting it seems to make a huge difference if the flow equations for $m_{\rho,k}$ and $m_{0,k}$ are evaluated at the k-dependent minimum in field space $\sigma_{0,k}$, as plotted in Fig. 4.2, or at the minimum at the IR scale $\sigma_{0,k_{\mathrm{IR}}}$ as done in Fig. 5.8, even for their values at the IR scale. Although the values for the Euclidean masses in Fig. 4.2 are closer to the physical ones, we here use the grid method and evaluate these flow equations as well as the flow equations for $\Gamma_k^{(2)}$ as usual at a fixed value in field space $\sigma = \sigma_{0,k_{\mathrm{IR}}}$.

In-medium spectral functions

Before discussing the in-medium modifications of the ρ and a_1 spectral functions in this setting, we look at the imaginary parts of the respective processes listed in Eq. (5.8) and Eq. (5.9) separately, shown in Fig. 5.9. As the capture processes become only possible and thus visible at finite temperature, we choose $T = 150$ MeV and $\mu = 0$ MeV for this plot.

For the ρ meson, Fig. 5.9a, we have the decay into a quark-antiquark, the decay into two pions and as new decay process the decay into an a_1-π-pair. Additionally the ρ can capture a pion from the heat bath forming an a_1 meson. This process gives

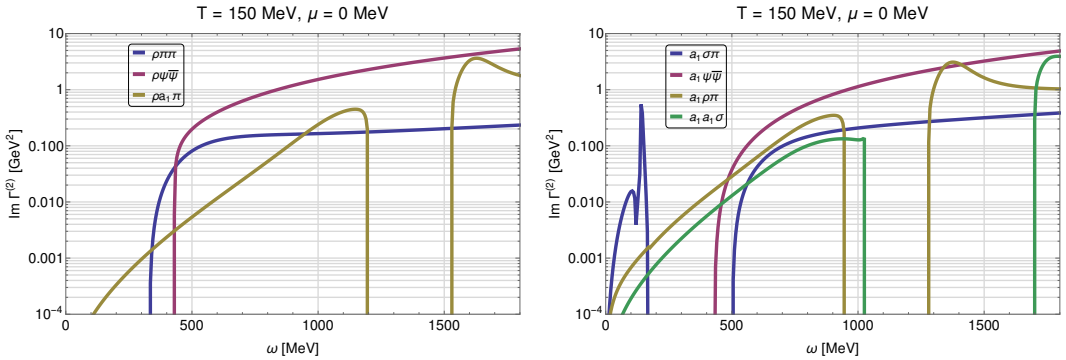

(a) (b)

Figure 5.9: Imaginary part of $\Gamma^{(2),R}$ divided into the different capture and decay processes at $T = 150$ MeV and $\mu = 0$ MeV separately for the ρ meson (a) and the a_1 meson (b).

rise to an increase of the imaginary part for lower frequencies and is energetically bounded by $\omega = m_{a_1} - m_\pi$. For the a_1 meson, Fig. 5.9b, we have as new processes the decay into a ρ-π pair and into an a_1-σ pair. Here also the related in-medium capture processes are possible, i.e. the capture of pion and of a sigma meson.

The resulting ρ and a_1 spectral functions at finite temperature and chemical potential are shown in Fig. 5.10. For $T = \mu = 0$ MeV, the picture is quite similar to the one found in Fig. 5.5, except the additional decay thresholds at large frequencies. Here only the threshold $\omega = m_\rho + m_\pi \approx 1549$ MeV is visible in the a_1 spectral function whereas the thresholds $\omega = m_{a_1} + m_\pi \approx 1926$ MeV and $\omega = m_{a_1} + m_\sigma \approx 2342$ MeV lie outside the considered energy region with the used UV-cutoff $\Lambda = 1500$ MeV.

With increasing temperature (left column in Fig. 5.10), the ρ and a_1 can capture particles from the heat bath, giving rise to an increase of both spectral functions in the low frequency domain. For the ρ meson we have the process $\rho^* + \pi \to a_1$, for the a_1 we have the processes $a_1^* + \pi \to \sigma$, $a_1^* + \pi \to \rho$ and $a_1^* + \sigma \to a_1$ contributing to the full imaginary part in this region, see Fig. 5.9 for the thresholds of the particular processes. In the a_1 spectral function we again see a pronounced peak at $T = 100$ MeV and $T = 150$ MeV which is analogue to a van Hove singularity and has already been discussed in Sec. 5.2.1. As the masses of the vector mesons decrease with increasing temperature, the thresholds for the new decay processes move towards smaller frequencies, like for the process $\rho^* \to a_1 + \pi$, at $T = 150$ MeV located at $\omega = m_{a_1} + m_\pi \approx 1530$ MeV. At $T = 300$ MeV the masses of the chiral partners are fully degenerate and the quarks become the lightest degrees of freedom which both leads to a complete degeneracy and broadening of the ρ and a_1 spectral functions, analogous to the high-temperature case in Fig. 5.5.

The chemical-potential dependent spectral functions on the right side of Fig. 5.10 are qualitative similar to the ones found in Fig. 5.5. Both spectral functions do not change up to μ-values near the CEP, which is expected from the Silver Blaze property also in this case. At $\mu = 297.4$ MeV and $\mu = 297.95$ MeV we see the effect of the dropping sigma mass in the significant lowering of the threshold for the decay channel $a_1^* \to \sigma + \pi$, where the structure of the resulting plateau is slightly different

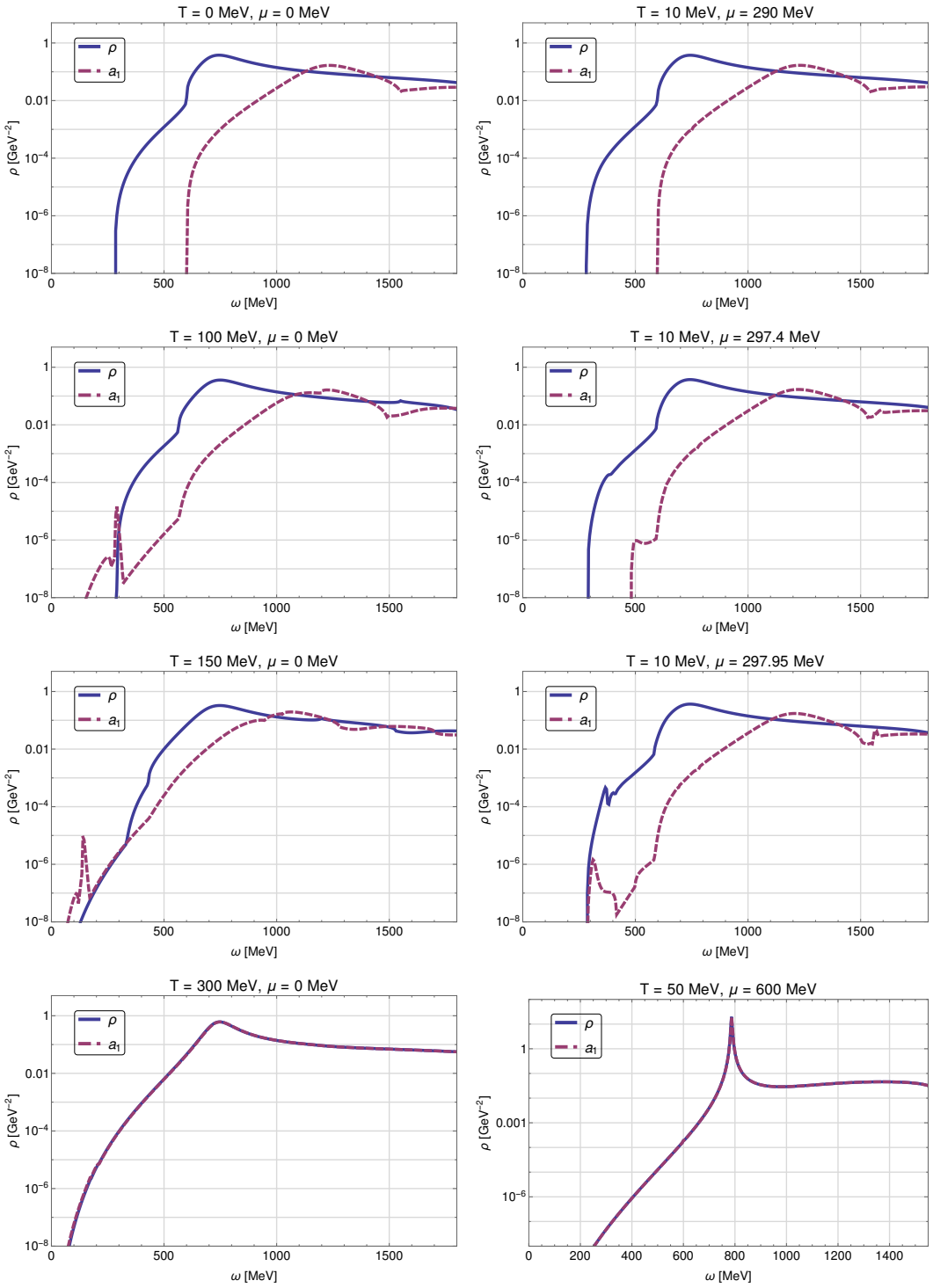

Figure 5.10: Spectral functins of the ρ (blue) and a_1 meson (dashed red) as a function of external frequency ω for increasing temperature at $\mu = 0$ MeV (left column) and for increasing chemical potential along the axis of the CEP at $T = 10$ MeV (right column).

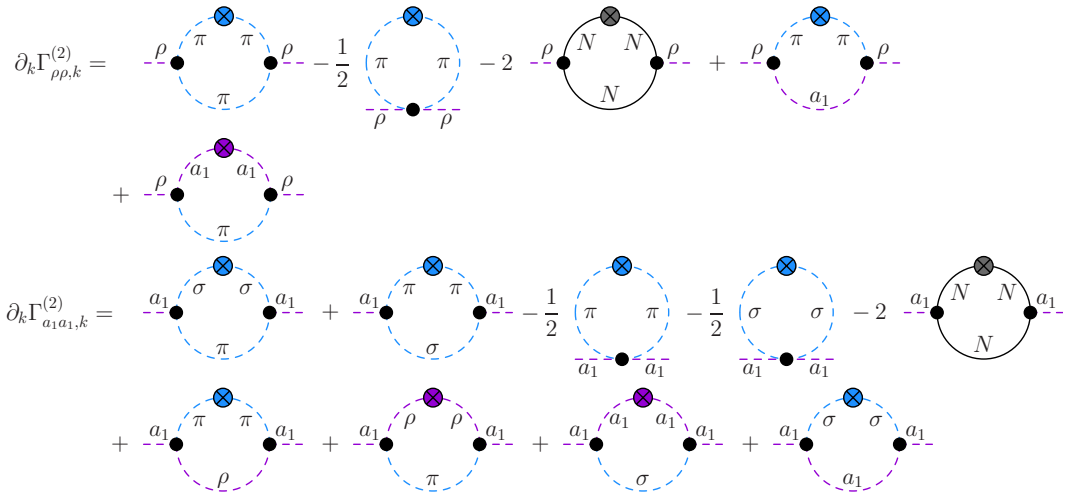

Figure 5.11: Flow equations for the ρ and a_1 two-point functions in diagrammatic form. Vertices are indicated by black dots, regulator insertions by crossed circles. The color of the lines and regulators represents the type of field: blue for scalar mesons, black for all combinations of the nucleons N_1 and N_2 and purple for vector mesons.

compared to the same case in Fig. 5.5. At the same time the threshold for $a_1^* \to \rho + \pi$ gets slightly more enhanced while the ρ spectral function does not really change at all. Overall, the only clear signature for the CEP is encoded in the dropping threshold in the a_1 spectral function. For large chemical potential we again see full degeneracy of both spectral functions reflecting the restoration of chiral symmetry.

5.2.3 Spectral Functions with Nucleons

In this section we now modify the ansatz used in the setting in Sec. 5.2.2 by replacing the quark fields with fields for the nucleon $N_1, \bar{N}_1$ and its parity partner $N_2, \bar{N}_2$. We then obtain a purely hadronic effective low-energy model, cf. Sec. 4.3.2, where the quarks and the associated unphysical decay processes in the hadronic phase are now absent.

Technically we therefore first solve the flow equation for the effective potential of the parity-doublet model, which was discussed in Sec. 3.3, and on this input the flow equations for m_V^2, m_0^2 and finally for the ρ and a_1 two-point functions which are illustrated in diagrammatic form in Fig. 5.11. Possible processes for the ρ meson in this setting are now

$$\begin{aligned} &\rho^* \to N + \bar{N}\,, \quad \rho^* + \bar{N}, N \to N, \bar{N}\,, \\ &\rho^* \to \pi + \pi\,, \\ &\rho^* \to a_1 + \pi\,, \quad \rho^* + \pi \to a_1\,, \qquad \rho^* + a_1 \to \pi\,. \end{aligned} \tag{5.10}$$

For the a_1 meson we have the processes

$$\begin{aligned}
&a_1^* \to N + \bar{N}\,, \quad a_1^* + \bar{N}, N \to N, \bar{N}\,, \\
&a_1^* \to \pi + \sigma\,, \quad a_1^* + \pi \to \sigma\,, \quad a_1^* + \sigma \to \pi\,, \\
&a_1^* \to \rho + \pi\,, \quad a_1^* + \pi \to \rho\,, \quad a_1^* + \rho \to \pi\,, \\
&a_1^* \to a_1 + \sigma\,, \quad a_1^* + \sigma \to a_1\,, \quad a_1^* + a_1 \to \sigma\,,
\end{aligned} \tag{5.11}$$

where the vector meson-nucleon processes as new ones compared to the previous setting are meant to hold for various combinations of N_1 and N_2, namely $V^* \to N_1, N_2 + \bar{N}_1, \bar{N}_2$ and $V^* \to N_2, N_1 + \bar{N}_1, \bar{N}_2$ as decay processes and $V^* + \bar{N}_1, N_1 \to N_2, \bar{N}_2$ and $V^* + \bar{N}_2, N_2 \to N_1, \bar{N}_1$ as in-medium capture processes with $V \in \{\rho, a_1\}$.

T- and μ-dependent Euclidean masses

As in the previous settings in Sec. 5.2.1 and Sec. 5.2.2 we fix the parameters for the effective potential to reproduce physical reasonable vacuum-values for the masses of the scalar mesons π/σ and the fermions, in this case the nucleon N_1 and its parity partner N_2. Since in the vacuum there are no baryons, one in principle has to fix their masses at $T = 0$ MeV close to a μ_B related to the onset of nuclear matter. Due to the Silver Blaze property we do not expect a significant change of these masses from $\mu = 0$ MeV to this onset-point and we therefore fix all masses together at $T = \mu = 0$ MeV. The parameters $g = 7.4$ and $m_{V,\Lambda} = 2035.0$ MeV are fixed to reproduce the phenomenological correct pole masses, resulting in $m_\rho^p = 774.1$ MeV and $m_{a_1}^p = 1262.4$ MeV. The corresponding Euclidean masses in the vacuum then have the following values

$$\begin{aligned}
\sigma_0 &= 93.0 \text{ MeV}\,, \quad & m_\sigma &= 633.5 \text{ MeV}\,, \\
m_\pi &= 140.9 \text{ MeV}\,, \quad & m_{B_1} &= 938.3 \text{ MeV}\,, \\
m_{B_2} &= 1535.6 \text{ MeV}\,, \quad & m_\rho &= 808.5 \text{ MeV}\,, \\
m_{a_1} &= 1062.0 \text{ MeV}\,.
\end{aligned} \tag{5.12}$$

Their temperature dependence at $\mu = 0$ MeV is shown in Fig. 5.12a. As expected from a crossover, all masses change very smoothly. While the masses of the ρ meson and the nucleon N_1 remain almost constant, the masses of their parity partners a_1 and N_2 decrease with increasing temperature which leads to a successive mass degeneracy for large temperatures. The masses of the scalar mesons π and σ behave similar to the ones already obtained in the quark-meson model calculations. At $T = 500$ MeV, the masses of the chiral partners ρ-a_1, N_1-N_2 and π-σ become (almost) completely degenerate.

The Euclidean masses as a function of baryon chemical potential across the chiral CEP at $T = 67$ MeV are shown in Fig. 5.12b. As this critical endpoint is located at larger T compared to the previous settings, especially the masses of the sigma meson and the N_2 slightly decrease from $\mu_B = 800$ MeV to values close to the CEP. As already discussed in the previous sections, at the CEP the sigma mass and the chiral order parameter drop significantly, leading also to a drop of the other masses. For very large μ_B we again see full degeneracy of the masses of the chiral partners.

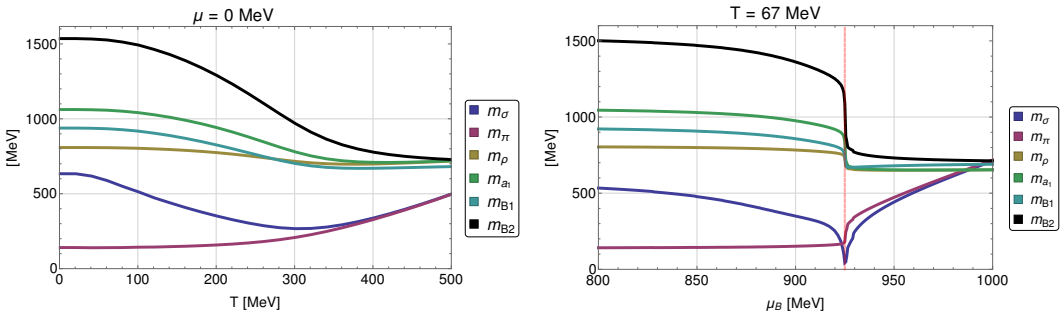

(a) (b)

Figure 5.12: Euclidean masses of all particles as a function of temperature at $\mu = 0$ MeV (a) and as a function of chemical potential across the chiral CEP which is located at around $T = 67$ MeV and $\mu = 925$ MeV (vertical red line) (b).

In-medium spectral functions

Spectral functions for the ρ and a_1 meson within this hadronic model are shown for different combinations of T and μ_B in Fig. 5.13.

Due to the absence of the quark-antiquark decay channel in this model, both spectral functions are less broad in the vacuum compared to the previous settings but show an enhanced peak located at the particular pole mass. In both cases, decays into scalar mesons $\rho^* \to \pi + \pi$ and $a_1^* \to \pi + \sigma$ are the most dominant processes in the vacuum which also determine the start-thresholds in both spectral functions. For the ρ we also have the decay $\rho^* \to a_1 + \pi$ located at $\omega \approx 1200$ MeV, which is quite weak and not really visible. The baryonic decay $\rho^* \to N_1 + \bar{N}_1$ located at $\omega = 2m_{B_1} \approx 1877$ MeV gives rise to a pronounced threshold. In the a_1 spectral function this threshold is only poorly visible but instead the threshold $a_1^* \to N_1 + \bar{N}_2$ at large frequencies $\omega = m_{B_1} + m_{B_2} \approx 2474$ MeV can be clearly identified. The other decay channels $a_1^* \to \rho + \pi$ and $a_1^* \to a_1 + \sigma$ do not contribute strongly and therefore are only barely visible in the a_1 spectral function.

With increasing temperature (left column in Fig. 5.13) the typical in-medium capture processes for the ρ and the a_1 meson become possible. At $T = 100$ MeV the a_1 spectral function already shows a pronounced plateau, where in this region all capture processes including the nucleon-scattering process $a_1^* + \bar{N}_1, N_1 \to N_2, \bar{N}_2$ are energetically possible and therefore contribute to the imaginary part of $\Gamma^{(2),R}$. Here the left peak can be related to the process $a_1^* + \pi \to \sigma$, the right one to the capture of a pion forming a ρ meson which also marks the right border of this plateau at $\omega = m_\rho - m_\pi \approx 660$ MeV. For $T = 200$ MeV this capture region gets even more enhanced where now the capture of nucleons provides the main contributions for low frequencies, $\omega \leq m_{B_2} - m_{B_1} \approx 464$ MeV. The peak next to this plateau is again related to the capture process $a_1^* + \pi \to \rho$. In the ρ spectral function the contributions of the decay into a pion pair suppresses the other capture-thresholds $\rho^* + \pi \to a_1$ and $\rho^* + \bar{N}_1, N_1 \to N_2, \bar{N}_2$ such that we only see small temperature effects. In both spectral functions the baryonic decay thresholds lower as their masses decrease with increasing temperature, cf. Fig. 5.12a.

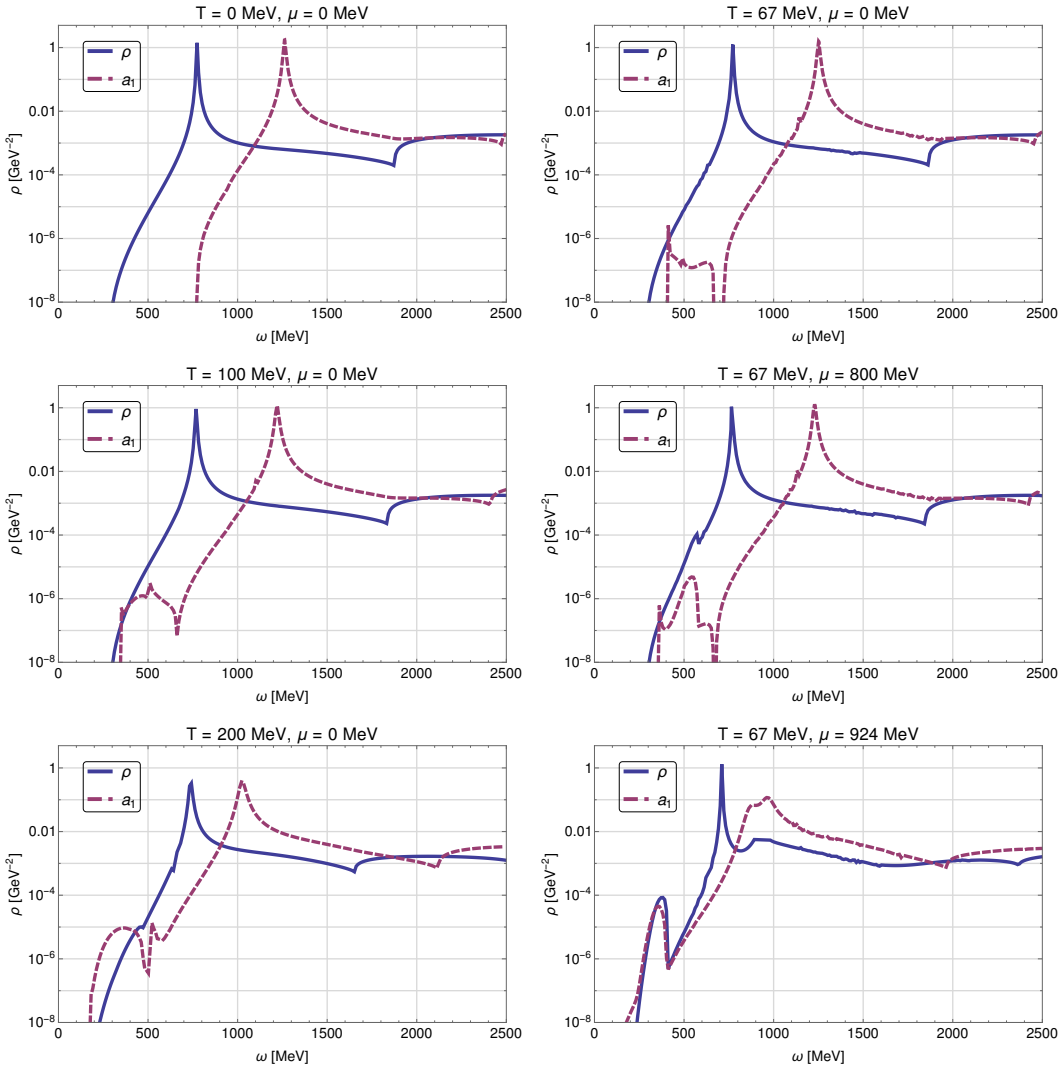

Figure 5.13: Spectral functions of the ρ (blue) and a_1 meson (dashed red) as a function of external frequency ω for increasing temperature at $\mu = 0$ MeV (left column) and for increasing chemical potential towards the chiral CEP at $T = 67$ MeV (right column).

Along the axis of the chiral critical endpoint at $T = 67$ MeV (right column in Fig. 5.13) we see that already at $\mu = 0$ MeV in-medium processes become possible. By cranking up the baryon chemical potential, the contribution from the capture of a N_1 forming a N_2 nucleon gets larger and larger, as can bee seen as enhanced bump and spike in both spectral functions at $\mu = 800$ MeV around $\omega \approx 555$ MeV. Close to the CEP at $\mu = 924$ MeV this effect gets even stronger forming almost a peak structure in both cases. As here the sigma mass abruptly lowers, cf. Fig. 5.12b, the threshold $a_1^* \to \pi + \sigma$ moves towards lower frequencies leading to a broadening of the a_1 spectral function.

Overall, the inclusion of baryon degrees of freedom leads to much sharper spectral functions as the contributions of the quark-antiquark decays, especially in the hadronic phase at low T and μ_B, are gone. The additional physical baryon-scattering processes in the medium contribute significantly to the imaginary part of $\Gamma^{(2)}$, especially for large μ_B near the chiral CEP. As in this calculation we suffered for example from non-monotonic behaviour of the k-dependent energy difference $E_{\sigma,k} - E_{\pi,k}$ at some T-μ_B combinations (which are not shown in Fig. 5.13) leading to unphysical capture thresholds, and in the present truncation we were not able to describe nuclear matter phenomenologically correct, cf. Sec. 3.3.2, a phenomenologically enhanced qualitative and quantitative study has to be postponed to future studies.

5.3 Electromagnetic Spectral Functions

5.3.1 Rho-Photon Mixing and FRG Setup

Beside the computation of vector meson spectral functions and the usage of VMD-relations like given in Eq. (5.4) one can also directly compute the in-medium electromagnetic spectral function to get access to the dilepton rate.

In this section we will use the model extension described in Sec. 4.3.1 to include the photon field A_μ and associated vertices $\Gamma^{(3)}$ and $\Gamma^{(4)}$ into our FRG setup in order to compute electromagnetic two-point functions and the related spectral functions. Technically we therefore go a step back and use a setting similar to the one in Sec. 5.2.1, i.e. input from the effective potential of the quark-meson model and only (pseudo-)scalar mesons and quarks as fluctuating fields in the flow equations for $\Gamma_k^{(2)}$ and $m_{V,k}^2$. The parameters here are the same as in Sec. 3.2.1 and Sec. 5.2.1. Due to the A_μ field in the ansatz for Γ_k we now have new non-vanishing vertices $\Gamma^{(3)}_{\pi\pi A}$, $\Gamma^{(3)}_{\psi\psi A}$, $\Gamma^{(4)}_{\pi\pi A\rho}$ and $\Gamma^{(4)}_{\pi\pi AA}$, giving rise to new diagrams, see App. B.2 for explicit expressions.

Since on the level of $\Gamma^{(2)}$ the ρ meson and the photon mix, the physical two-point functions are obtained by diagonalizing the following 2×2 matrix

$$\begin{pmatrix} \Gamma^{(2)}_{AA} & \Gamma^{(2)}_{A\rho} \\ \Gamma^{(2)}_{\rho A} & \Gamma^{(2)}_{\rho\rho} \end{pmatrix} \xrightarrow{\text{diagonalise}} \begin{pmatrix} \tilde{\Gamma}^{(2)}_{AA} & 0 \\ 0 & \tilde{\Gamma}^{(2)}_{\rho\rho} \end{pmatrix}, \tag{5.13}$$

where the physical electromagnetic two-point function $\tilde{\Gamma}^{(2)}_{AA}$ is given by

$$\tilde{\Gamma}^{(2)}_{AA} = \frac{1}{2}\left\{ \Gamma^{(2)}_{\rho\rho} + \Gamma^{(2)}_{AA} - \sqrt{\left(\Gamma^{(2)}_{\rho\rho} - \Gamma^{(2)}_{AA}\right)^2 + 4\,\Gamma^{(2)}_{\rho A}\Gamma^{(2)}_{A\rho}} \right\}. \tag{5.14}$$

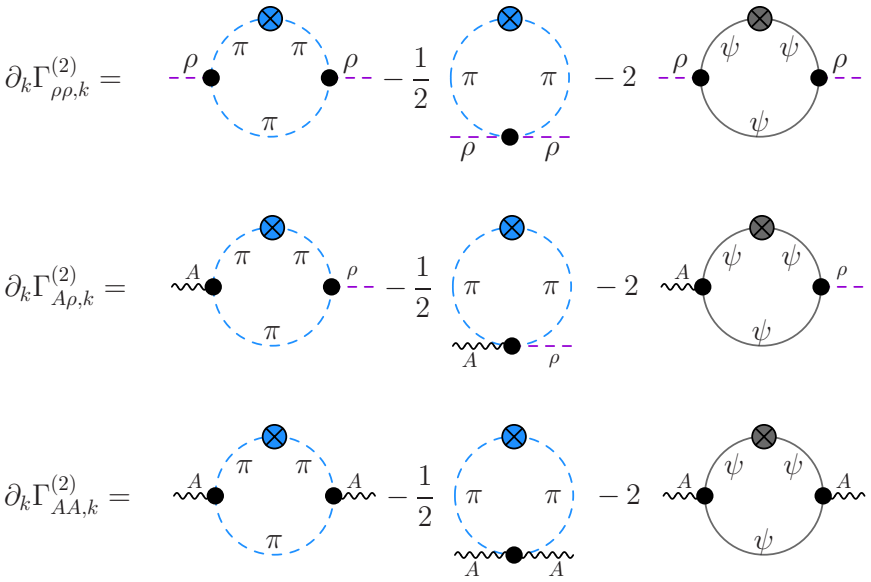

Figure 5.14: Diagrammatic representation of the flow equations for the bare rho, the bare photon and the the mixed rho-photon two-point function.

The flow equations for the bare ρ meson, the bare photon and the mixed rho-photon two-point function are illustrated in Fig. 5.14. By solving these flow equations separately one can then with Eq. (5.14) compute the physical photon two-point function and based on that the associated electromagnetic spectral function.

In order to get physical insights into this expression for $\tilde{\Gamma}^{(2)}_{AA}$ we can expand the particular two-point functions in powers of the electromagnetic coupling $e = \frac{4\pi}{137}$. The self-energy parts of the bare two-point functions are of the following orders,

$$\Gamma^{(2)}_{\rho\rho} = \mathcal{O}(g^2)\,, \qquad \Gamma^{(2)}_{AA} = \mathcal{O}(e^2)\,, \qquad \Gamma^{(2)}_{\rho A} = \Gamma^{(2)}_{A\rho} = \mathcal{O}(eg)\,, \tag{5.15}$$

with g being the gauge coupling. By a Taylor expansion in e we find for the photon two-point function

$$\tilde{\Gamma}^{(2)}_{AA} = \underbrace{\Gamma^{(2)}_{AA} - \frac{\Gamma^{(2)}_{A\rho}\Gamma^{(2)}_{\rho A}}{\Gamma^{(2)}_{\rho\rho}}}_{\mathcal{O}(e^2)} + \mathcal{O}(e^4)\,. \tag{5.16}$$

The first correction term from the rho-photon mixing is of the same order in e as the bare photon two-point function. Physically, this second term represents the ρ contribution to the photon two-point function which reflects the idea of vector meson dominance.

5.3.2 Electromagnetic Spectral Functions: Results

We now discuss results for the in-medium electromagnetic spectral functions, which are obtained by the real and imaginary part of the physical two-point function $\tilde{\Gamma}^{(2)}_{AA}$.

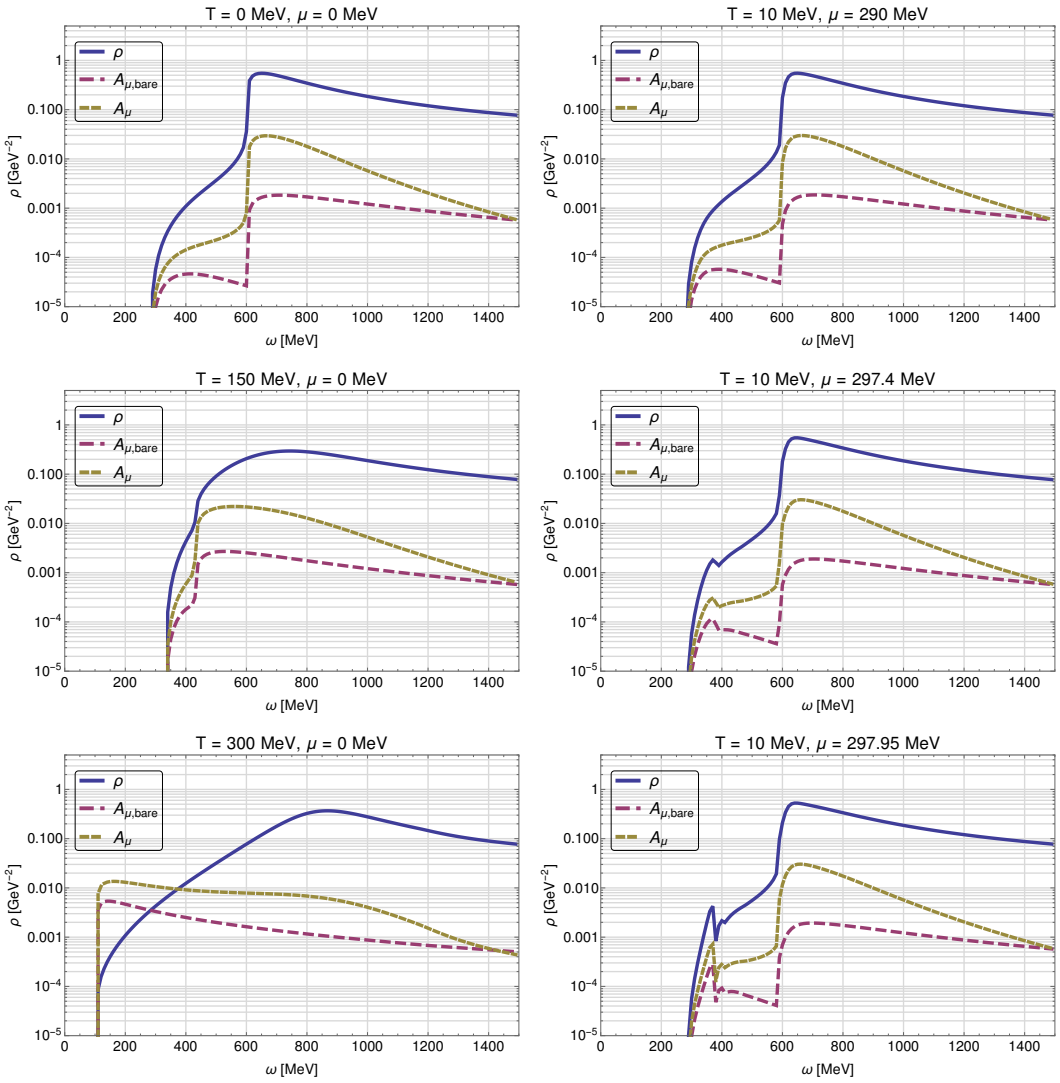

Figure 5.15: Spectral functions of the bare ρ meson (blue), the bare photon (dashed red) and the full photon (dashed yellow) as a function of external frequency ω for increasing temperature at $\mu = 0$ MeV (left column) and for increasing chemical potential towards the CEP along $T = 10$ MeV (right column).

In Fig. 5.15 we see the bare ρ spectral function, the bare photon spectral function and the full photon spectral function at different combinations of temperature and quark-chemical potential.

In the present truncation, the ρ and the photon can only decay into two pions and a quark-antiquark pair. The particular thresholds in the vacuum are located at $\omega = 2m_\pi \approx 280$ MeV and $\omega = 2m_\psi \approx 600$ MeV, see Fig. 5.3 for the related input-masses. The bare ρ spectral function is thereby in all T-μ-cases the same as in Fig. 5.5. With increasing temperature (left column in Fig. 5.15) the quarks get lighter and the pions heavier leading to the typical broadening of the spectral functions already observed in Sec. 5.5 and Fig. 5.10. Since the photon-pion coupling is much smaller than the rho-pion coupling ($e \ll g$), the bare photon spectral function becomes more flat compared to the bare rho one, especially at $T = 300$ MeV, while the physical photon spectral function is a mixture of both bare spectral functions.

Close to the CEP (right column in Fig. 5.15), we only see small modifications in the pion threshold in all spectral functions while their principle vacuum structure basically remains unchanged.

The fact that we do not observe clear signatures for the critical endpoint in the electromagnetic spectral function is no surprise as neither the ρ spectral function nor the bare photon spectral function contain processes which would show up for example a dropping sigma threshold close to the CEP. In our truncation, the propagators in the loops are sharp, representing only the single-particle contributions and one therefore would need a sigma propagator in the loops of the flow equations for $\Gamma_k^{(2)}$ which, however, is absent for the bare ρ and bare photon two-point functions.

In order to make the critical endpoint of the model visible in the electromagnetic spectral function we would have to improve the current truncation for example by inserting full a_1 propagators inside the loops. In this way, signatures for critical physics could show up in the ρ spectral function via processes like $\rho^* \to \pi + a_1$.

6

Self-Consistent Solutions of Flow Equations

In the previous chapter we saw that the FRG is an appropriate tool to compute meaningful (axial-)vector meson and electromagnetic spectral functions, also in the vicinity of phase transitions and critical endpoints. A central issue in the truncation usually employed in these calculations is the usage of propagators which only describe the single-particle contribution of the particular fields, and not the fully dressed propagators containing the full spectral properties. Unfortunately, this is necessary to ensure the location of thresholds to be determined by the physical pole masses as well as to resolve non-trivial structures in the spectral functions, for example n-particle thresholds.

From the perspective of the FRG, this turns out to be very difficult from a technical point of view as the necessary analytic continuation procedure avoids a simple iteration scheme. However, in this chapter we present a numcerical procedure to compute self-consistent spectral functions using the Källén–Lehmann spectral representation which also allows for a straightforward generalization to finite temperature. To demonstrate the feasibility of this procedure we compute spectral functions of the pion and the sigma meson within the $O(4)$-symmetric model. This approach was driven by a first FRG study on self-consistent spectral functions in the vacuum in which the formalism is very difficult to apply at finite temperature [40].

The used $O(n)$-symmetric model represents a simple effective low-energy model for QCD and plays also an important role in condensed matter physics. Therefore it has been the subject of various FRG studies [33, 37, 157–159].

After discussing the basic idea in Sec. 6.1.1, we present the numerical procedure, first for the Euclidean system and then for the Minkowski system in Sec. 6.1.2. Results are then shown for first checks on the reconstruction method in Sec. 6.1.1 and finally for spectral functions in the $O(4)$ model in Sec. 6.2.2.

6.1 Basic Idea and Numerical Setting

6.1.1 Introduction

Starting point is the $O(4)$-symmetric model and its flow equations for the pion and sigma meson two-point functions, illustrated in Fig. 6.1. The idea of solving FRG flow equations self-consistently is to reinsert the k-dependent two-point functions calculated in every k-step on the left side as new input into the loops on the right side of the equations for $\Gamma_k^{(2)}$. Compared to the previous truncation where we extracted the k-dependent two-point functions on the right side of the equations always from the ansatz of the effective average action, this would end up in a completely backcoupled solution. While this is in principle straightforwardly possible for the Euclidean system [78], a backcoupled solution within the real-time formalism requires a closer consideration.

The numerical procedure which we apply proceeds as follows. At first we solve the Euclidean system consisting of the equations for $\Gamma_{\pi,k}^{(2)}$, $\Gamma_{\sigma,k}^{(2)}$ and the equation for the effective potential U_k. The vertices $\Gamma_k^{(3)}$ and $\Gamma_k^{(4)}$ are then extracted momentum independently from the effective potential. While doing this, we store the k-flow of all Euclidean quantities, namely the Euclidean masses, the vertices and the momentum independent tadpoles. Using this Euclidean input, we solve the Minkowski system consisting only of the momentum-dependent diagrams in a self-consistent way. The Minkowski system is obtained from the Euclidean counterpart by using the usual analytic continuation procedure (as we use a three-dimensional regulator) and the spectral representation for Euclidean regulated propagators. To get rid of the full field-dependent equations, we use a truncation to only obtain two-point functions and spectral functions at the physical minimum σ_0.

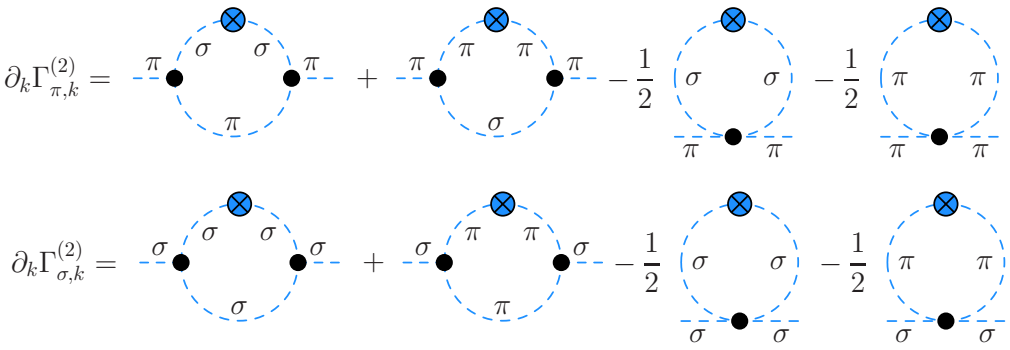

Figure 6.1: Flow equations for the π and σ two-point functions within the $O(4)$ model in a diagrammatic form.

6.1.2 Numerical Procedure

Euclidean system

In the Euclidean system we have to deal with the following system of equations,

$$\begin{aligned}
\partial_k U_k[\phi] &= \mathrm{Flow}\left(R_k, \Gamma^{(2),E}_{k,\pi}, \Gamma^{(2),E}_{k,\sigma}\right), \\
\partial_k \Gamma^{(2),E}_{k,\pi}[\phi=\phi_0; p_0, \vec{p}] &= \mathrm{Flow}\left(R_k, \Gamma^{(3)}_k, \Gamma^{(4)}_k, \Gamma^{(2),E}_{k,\pi}, \Gamma^{(2),E}_{k,\sigma}\right)\Big|_{\phi=\phi_0}, \\
\partial_k \Gamma^{(2),E}_{k,\sigma}[\phi=\phi_0; p_0, \vec{p}] &= \mathrm{Flow}\left(R_k, \Gamma^{(3)}_k, \Gamma^{(4)}_k, \Gamma^{(2),E}_{k,\pi}, \Gamma^{(2),E}_{k,\sigma}\right)\Big|_{\phi=\phi_0}.
\end{aligned} \tag{6.1}$$

The flow of the effective potential is solved on a grid in field-direction, whereas the flow equations of the two-point functions $\Gamma^{(2),E}_{k,\pi}$ and $\Gamma^{(2),E}_{k,\sigma}$ are evaluated at the physical minimum at the IR scale σ_0. To backcouple field-dependent two-point functions into the flow of the effective potential, we assume the following decomposition in order to obtain these field-dependent two-point functions,

$$\Gamma^{(2),E}[\phi, p] = \Gamma^{(2),E}[\phi_0, p] - \Gamma^{(2),E}[\phi_0, 0] + m^2_E[\phi]\,. \tag{6.2}$$

We hence separate the full two-point function into a field-independent but momentum dependent part and a field-dependent but momentum independent part which is identified with the Euclidean mass extracted from the effective potential. This separation-ansatz seems rather natural when coming from the usual LPA or LPA′ truncation but of course contains fully backcoupled objects. How good this truncation is, compared to the full field-dependent solution, has to be checked in future comparative studies.

In the evaluation of the right side of the flow equations for $\Gamma^{(2),E}_k$ we have to deal with a Matsubara sum over bosonic Matsubara frequencies $q_{0,n}$ and a three dimensional integral over the spatial components of the loop momentum $\vec{q}$. The expression for a momentum dependent diagram is then given by (and analogously for the tadpoles)

$$J_k(p_0, \vec{p}) = \sum_n \int d^3\vec{q}\, \left(\Gamma^{(3)}\right)^2 \partial_k R_k(\vec{q})\, \left(D^E_k(q_{0,n}, \vec{q})\right)^2 D^E_k(q_{0,n} \pm p_0, \vec{q} \pm \vec{p})\,, \tag{6.3}$$

where the regulated Euclidean propagator is related to the two-point function as usual by $D^E_k \equiv D^{E,\mathrm{Reg}}_k = (\Gamma^{(2),E}_k + R_k)^{-1}$.

Since the Matsubara sum as well as the spatial integral cannot be performed analytically, we set up a grid for the Euclidean two-point functions in p_0 and $|\vec{p}|$ direction and solve all expressions like in Eq. (6.3) at every scale k on every gridpoint $(p_{0i}, |\vec{p}|_j)$. In the numerical calculation we sum over a finite number of Matsubara modes and extrapolate if the momenta jump off the grid. We checked explicitly that the number of Matsubara modes we included ($n_{\max} \approx \pm 100$) and the concrete extrapolation procedure does not affect the results. As inital form at the UV scale $\Lambda = 500$ MeV we set

$$\begin{aligned}
U_\Lambda[\phi] &= a\,\phi^2 + b\,\phi^4\,, \\
\Gamma^{(2),E}_{\pi,\Lambda}[\phi_0; p_0, \vec{p}] &= p_0^2 + \vec{p}^{\,2} + m^2_{\pi,\Lambda}[\phi_0]\,, \\
\Gamma^{(2),E}_{\sigma,\Lambda}[\phi_0; p_0, \vec{p}] &= p_0^2 + \vec{p}^{\,2} + m^2_{\sigma,\Lambda}[\phi_0]\,,
\end{aligned} \tag{6.4}$$

where as usual, we add the explicit symmetry breaking term $c\sigma$ only at the IR scale. The parameters a, b and c are chosen to reproduce physical reasonable values for σ_0 and the (pole) masses m_π^p and m_σ^p in the vacuum, cf. Sec. 6.2.2: $a = -7.46 \cdot 10^4$ MeV^2, $b = 3.65$, $c = 1.75 \cdot 10^6$ MeV^3. As regulator function we use the standard three-dimensional Litim regulator.

Minkowski system

In order to construct an analytically continued system of equations for retarded two-point functions $\Gamma^{(2),R}$, we use the Källén–Lehmann spectral representation for the scale-dependent regulated Euclidean propagators, which reads

$$D_k^{E,\mathrm{Reg}}(p_0,\vec{p}) = \int_{-\infty}^{\infty} d\omega' \frac{1}{\omega' + \mathrm{i}p_0}\,\rho_k(\omega',\vec{p}) = \int_0^{\infty} d\omega' \frac{2\omega'}{\omega'^2 + p_0^2}\,\rho_k(\omega',\vec{p})\,. \tag{6.5}$$

The existence of a spectral representation just follows from Cauchy's integral theorem and the use of a three-dimensional regulator function.

After replacing the propagators with this representation, the loop functions on the right side of the flow equations have the following form (see Eq. (6.3) for the Euclidean counterpart)

$$J_k(p_0,\vec{p}) = \sum_n \int d^3\vec{q} \int_{\omega_1,\omega_2,\omega_3} d\omega_1 d\omega_2 d\omega_3 \;\left(\Gamma_k^{(3)}\right)^2 \partial_k R_k(\vec{q}) \tag{6.6}$$

$$\times \frac{8\;\omega_1\omega_2\omega_3\;\rho_{k,1}(\omega_1,\vec{q})\rho_{k,2}(\omega_2,\vec{q})\rho_{k,3}(\omega_3,\vec{q}-\vec{p})}{\left(\omega_1^2 + q_{0,n}^2\right)\left(\omega_2^2 + q_{0,n}^2\right)\left(\omega_3^2 + (p_0 - q_{0,n})^2\right)}\,, \tag{6.7}$$

which obviously still involves a spatial momentum integration. If we use an $O(4)$ approximation of the form $\rho_k(\omega,\vec{p}) = \rho_k\left(\sqrt{\omega^2+\vec{p}^2},0\right) \equiv \rho_k(\sqrt{\omega^2+\vec{p}^2})$, we can shift the non-trivial spatial momentum dependence in the first argument and trivially carry out the spatial momentum integration. We are hence left with ω-integrals for every propagator involved in the loops on the right side of the flow equations which have to be performed in every integration step. Note that this $O(4)$ approximation is strictly speaking only valid at vanishing temperature for a regulator that does not break $O(4)$ invariance, i.e. not for the three-dimensional regulator considered here, while it is in any case just an approximation at finite temperature. We use this approximation here to reduce the number of momentum arguments that have to be taken into account to resolve the momentum dependence of the two-point function.

In these expressions we can then perform the Matsubara sum analytically and simply apply the standard analytic continuation procedure described in Sec. 2.2.2. The Euclidean system then turns into a Minkowski system with flow equations for the real and imaginary parts of the retarded two-point functions,

$$\begin{aligned}
\partial_k \mathrm{Re}\,\Gamma_{k,\pi}^{(2),R}[\phi_0;\omega] &= \mathrm{Flow}\left(R_k,\Gamma_k^{(3)}[\phi_0],\Gamma_k^{(4)}[\phi_0];\rho_{\pi,k},\rho_{\sigma,k}\right)\,,\\
\partial_k \mathrm{Im}\,\Gamma_{k,\pi}^{(2),R}[\phi_0,\omega] &= \mathrm{Flow}\left(R_k,\Gamma_k^{(3)}[\phi_0],\Gamma_k^{(4)}[\phi_0];\rho_{\pi,k},\rho_{\sigma,k}\right)\,,\\
\partial_k \mathrm{Re}\,\Gamma_{k,\sigma}^{(2),R}[\phi_0,\omega] &= \mathrm{Flow}\left(R_k,\Gamma_k^{(3)}[\phi_0],\Gamma_k^{(4)}[\phi_0];\rho_{\pi,k},\rho_{\sigma,k}\right)\,,\\
\partial_k \mathrm{Im}\,\Gamma_{k,\sigma}^{(2),R}[\phi_0,\omega] &= \mathrm{Flow}\left(R_k,\Gamma_k^{(3)}[\phi_0],\Gamma_k^{(4)}[\phi_0];\rho_{\pi,k},\rho_{\sigma,k}\right)\,.
\end{aligned} \tag{6.8}$$

The k-dependent spectral function ρ_k can be computed at every scale k as

$$\rho_k(\omega) = \frac{1}{\pi} \frac{\operatorname{Im} \Gamma_k^{(2),R}(\omega)}{\left(\operatorname{Re} \Gamma_k^{(2),R}(\omega) - k^2\right)^2 + \left(\operatorname{Im} \Gamma_k^{(2),R}(\omega)\right)^2} , \tag{6.9}$$

for the pion and sigma meson respectively. The shifted real part is due to the inclusion of the Litim regulator and the continuation procedure, where we have a global minus sign.

To reduce the numerical effort, we further consider the combination

$$(DD)_k^{E,\mathrm{Reg,eff}}(p_0, \vec{p}) = D_k^{E,\mathrm{Reg}}(p_0, \vec{p}) \cdot D_k^{E,\mathrm{Reg}}(p_0, \vec{p}) , \tag{6.10}$$

for which we also assume a spectral representation and whose spectral function then reads (again for three-dimensional flat regulator and vanishing spatial external momentum)

$$\rho_k^{\mathrm{eff}}(\omega) = -\frac{1}{\pi} \frac{2 \operatorname{Im} \Gamma_k^{(2),R}(\omega) \left(\operatorname{Re} \Gamma_k^{(2),R}(\omega) - k^2\right)}{\left(\left(\operatorname{Re} \Gamma_k^{(2),R}(\omega) - k^2\right)^2 + \left(\operatorname{Im} \Gamma_k^{(2),R}(\omega)\right)^2\right)} . \tag{6.11}$$

We note that the existence of a spectral representation of such a combination is a priori not clear if the involved propagators have a non-trivial structure. The consequences of this assumption have to be tested in future studies.

However, in this way we can reduce the three-dimensional ω-integrals in Eq. (6.7) to two-dimensional ones. A general momentum-dependent loop function $J_k(p_0)$ at $T = 0$ MeV (for simplicity) then reads

$$J_k(p_0) = \int_{\omega_1,\omega_2} d\omega_1 d\omega_2 \, \frac{10k^4 \, (\omega_1 + \omega_2) \, \rho_k^{\mathrm{eff}}(\omega_1) \rho_k(\omega_2)}{15\pi^2 \left((\omega_1 + \omega_2)^2 + p_0^2\right)} . \tag{6.12}$$

In the numerical calculation, the system of equations given in Eq. (6.8) is solved on a grid in frequency-direction ω_i whereby the two-dimensional frequency-integrals can be solved numerically in every k-step. The cutoff for these frequency-integrals Λ_ω determines the size of the ω-grid and is chosen to be much larger than the RG cutoff scale Λ, where we extrapolate the spectral functions for $\omega > \Lambda_\omega$ with $\rho(\omega) \propto 1/\omega^2$ and checked explicitly that the results do not depend on the precise value of the cutoff, see Fig. 6.4a. The initial conditions for the real and imaginary parts of the two-point functions at the UV-scale Λ are chosen to be

$$\Gamma_{\pi,\Lambda}^{(2),R}[\phi_0; \omega] = (\omega + \mathrm{i}\epsilon)^2 - m_{\pi,\Lambda}^2[\phi_0] , \tag{6.13}$$

$$\Gamma_{\sigma,\Lambda}^{(2),R}[\phi_0; \omega] = (\omega + \mathrm{i}\epsilon)^2 - m_{\sigma,\Lambda}^2[\phi_0] , \tag{6.14}$$

where ϵ is kept as a small parameter and the Euclidean masses $m_{\pi,\Lambda}^2[\phi_0]$ and $m_{\sigma,\Lambda}^2[\phi_0]$ are extracted from the effective potential.

6.2 Self-Consistent Spectral Functions: Results

6.2.1 Reconstructing Propagators: First Checks

In a first step, the reconstruction procedure of propagators used in the Minkowski framework is tested. Therefore we compare Euclidean propagators obtained as inverse from the solution of the Euclidean system to those ones obtained by calculating

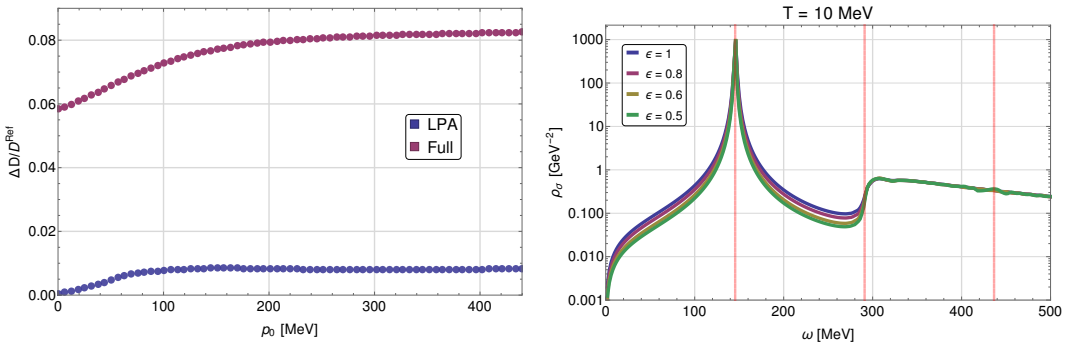

(a) (b)

Figure 6.2: Comparison of the resulting Euclidean pion propagators obtained by two different calculation methods, for the LPA truncation (blue) and the full self-consistent framework (red) (see text for details) (a) and vacuum-spectral function within a $O(1)$ model for different values for ϵ (shown in units of MeV) (b).

the spectral function via solving the Minkowski system and using the spectral representation from Eq. (6.2). The relative difference in comparison to a reference propagator (here the one obtained from the Euclidean system) as a function of discrete Euclidean frequency p_0 is shown in Fig. 6.2a, once for the LPA truncation and once for the full self-consistent solution, in both cases for the pion propagator at the IR scale.

The reconstruction of LPA propagators seems to work very well since the deviation here is 1% at most (blue dots in Fig. 6.2a). As possibly expected, the reconstruction of the full backcoupled propagators is not as good as in the LPA case since of course we have non-trivial effects in the k-dependent spectral functions in this system what makes this calculation also numerically much more involved. The deviation in this calculation of around 8% at most is quite acceptable though (red dots in Fig. 6.2a). In both cases the most precise reconstruction can be made at the lowest Matsubara frequency $p_0 = 0$ MeV.

As a next check we calculate the spectral function of a simple $O(1) \backsimeq \mathbb{Z}_2$ model with only one scalar field σ within the self-consistent framework, plotted for different values for the ϵ-parameter in Fig. 6.2b. In this setting, the off-shell σ^* can in principle decay into multiple sigma fields which thresholds are indicated with vertical red lines in Fig. 6.2b (m_σ, $2m_\sigma$, $3m_\sigma$). While the inclusion of only the single-particle contributions of the full propagators leads to decay processes of the form $A^* \to B+C$ (as done in Chapter 5), a self-consistent solution contains in principle all possible n-particle thresholds. Once a threshold appears in the k-dependent spectral function, it gets backcoupled to thresholds appearing in the next k-step. In Fig. 6.2b we see a little bump exactly located at $3m_\sigma$, which signals that the first non-trivial process $\sigma^* \to 3\sigma$ is included in this self-consistent calculation. How large the contribution of this specific process to the imaginary part of $\Gamma^{(2),R}$ actually is cannot be answered within this purely numerical procedure and has to be studied in future comparable projects.

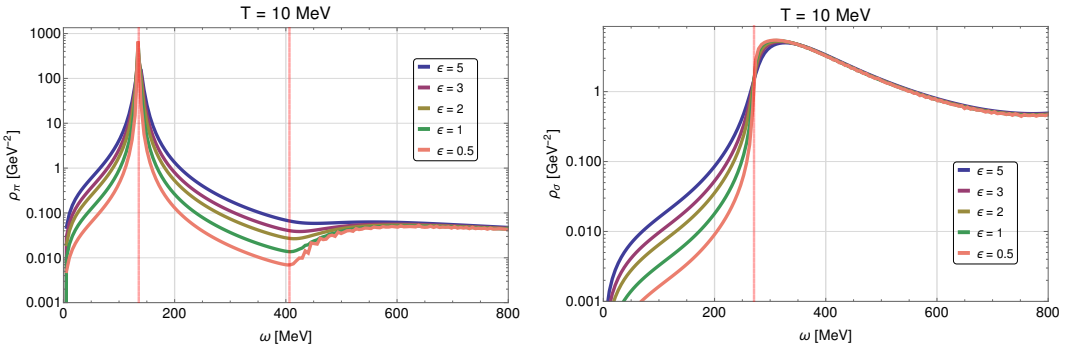

(a) (b)

Figure 6.3: Spectral functions of the pion (a) and sigma meson (b) as a function of external frequency ω at $T = 10$ MeV for different values of ϵ (shown in units of MeV).

6.2.2 Spectral Functions in the $O(4)$ Model

After having tested the reconstruction procedure on a more basic level, we now present results for self-consistent spectral functions for the pion and sigma meson within the $O(4)$ model. We therefore proceed exactly as described in Sec. 6.1, where the parameters for the effective potential at the UV scale from Eq. (6.4) and for the explicit symmetry breaking term are chosen to reproduce physical reasonable values for the pion and sigma pole masses, which are again identified with the zero crossing of the real part of $\Gamma^{(2),R}$. The resulting minimum σ_0 and the pole masses together with the corresponding Euclidean masses extracted from the effective potential are listed in Tab. 6.1. While for the pion the pole and Euclidean mass almost agree, the difference is larger for the sigma masses. This is not surprising as especially for heavier and not so well isolated bound states and resonances there is no a priori reason for them to agree.

The pion and sigma meson spectral functions at $T = 10$ MeV for different values of the ϵ-parameter (from the analytic continuation procedure) are shown in Fig. 6.3. The vertical red lines in Fig. 6.3a indicate the position of the pion pole mass and the location of the first non-trivial three-particle threshold at $\omega = 3m_\pi^p \approx 406.5$ MeV. We see that for smaller ϵ-values the pion spectral function develops a threshold exactly at this position, signaling that the sigma propagator in the loops in Fig. 6.1 now basically is the two-pion resonance from Fig. 6.3b giving rise to the process $\pi^* \to \sigma + \pi \simeq 3\pi$. However, this process is the only non-trivial which is energetically possible in the considered ω-window. The sigma meson spectral function shows the

σ_0	m_π^p	m_σ^p	m_π^E	m_σ^E
93.0 MeV	135.5 MeV	353.7 MeV	137.4 MeV	429.6 MeV

Table 6.1: Values for $\sigma_0 \equiv f_\pi$, the Euclidean masses and the corresponding pole masses in the vacuum at $T = 10$ MeV.

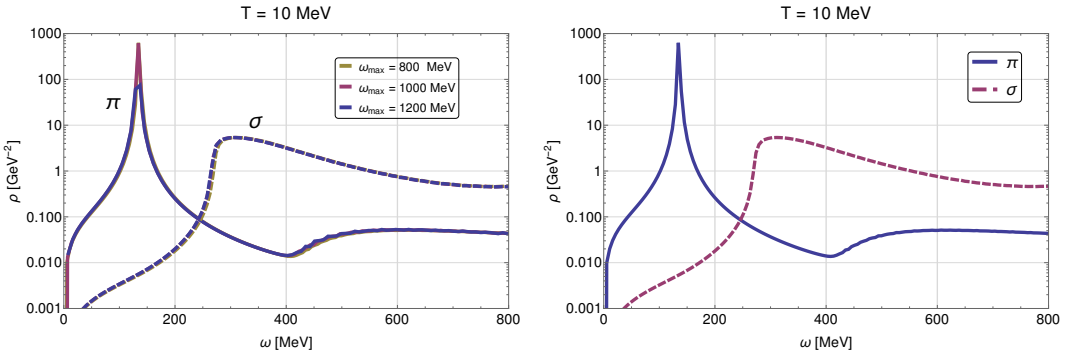

(a) (b)

Figure 6.4: Spectral functions of the pion and sigma meson as a function of external frequency ω for different values of the frequency-cutoff Λ_ω (a) for $\Lambda_\omega = 800$ MeV and $\epsilon = 1$ MeV as final setting (b).

usual pronounced two-pion threshold which location is now determined by two times the pion pole mass (vertical red line in Fig. 6.3b).

In order to test the dependency on the cutoff of the frequency-integrals, cf. the Minkowski system in Sec. 6.1, both spectral functions for $\epsilon = 1$ MeV and different values for this cutoff, denoted by Λ_ω, are shown in Fig. 6.4a. As we see, all curves lie on top of each other which shows that the results do not depend on the concrete value of Λ_ω. However, as final configuration we chose $\Lambda_\omega = 800$ MeV and $\epsilon = 1$ MeV, plotted for $T = 10$ MeV in Fig. 6.4b.

Pion and sigma spectral functions for $T = 100$ MeV and $T = 800$ MeV are shown in Fig. 6.5. At $T = 100$ MeV, possible capture processes lead to a broadening of the peak in the pion spectral function as well as of the whole sigma spectral function due to which the decay threshold in the pion spectral function can only barely be identified. The pole mass of the pion slightly decreases to a value of $m_\pi^p = 119.7$ MeV, the sigma meson pole mass stays almost constant and has at $T = 100$ MeV a value of $m_\sigma^p = 355$ MeV. By increasing the temperature further to $T = 800$ MeV, the pole

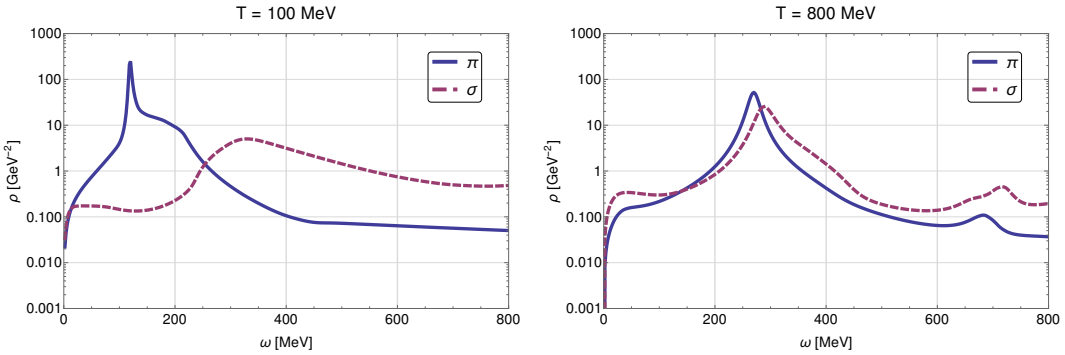

(a) (b)

Figure 6.5: Spectral functions of the pion (blue) and sigma meson (red) as a function of external frequency ω at $T = 100$ MeV (a) and $T = 800$ MeV (b).

masses are $m_\pi^p = 270$ MeV and $m_\sigma^p = 291$ MeV whereby both spectral functions now form a more enhanced peak and tend to degenerate completely.

Although this purely numerical procedure of solving Euclidean and real-time flow equations self-consistently works, an important next step would be to perform an $\epsilon = 0$-calculation and to study the specific trivial and non-trivial processes isolated such that for example their strength and visibility can be estimated.

7

Summary and Outlook

The main topic of this thesis was the computation of (axial-)vector meson spectral functions at finite temperature and chemical potential within the non-perturbative functional renormalization group approach. Here we used a recently proposed analytic continuation procedure on the level of the flow equations in order to get access to spectral functions as real-time quantities. These computations were performed on the basis of low-energy effective models for QCD aiming at a qualitative description of the hadronic sector of QCD and the associated interactions involving the (axial-)vector mesons. Additionally to that, we computed in-medium electromagnetic spectral functions and presented first results for self-consistent spectral functions within a simple $O(4)$ model. In this chapter we now want to summarize the main results obtained in these calculations and discuss possible next steps for future studies.

Starting point was the quark-meson model together with the parity-doublet model as low-energy effective models for two-flavor QCD incorporating the concept of chiral symmetry, discussed and presented in Chapter 3. There we focused on the phase structure of these models where in the quark-meson model we found the typical structure of a chiral critical endpoint at low temperatures and large quark chemical potentials dividing a crossover transition for larger temperatures from a first order phase transition for $T \lesssim 10$ MeV. The inclusion of the nucleon and its parity partner as baryon degrees of freedom within the parity-doublet model allowed for a modelling of the liquid-gas phase transition, in addition to the chiral transition. Here it turned out that with the used LPA truncation it is not able to fix the phenomenologically correct value for the binding energy and for the saturation density simultaneously. Consequently, this model was rather used in a qualitative sense serving as a purely hadronic effective model. The phenomenologically correct description of nuclear matter in a quantitative sense has to be postponed to future projects. Here, a mean-field omega meson together with an improved truncation towards LPA$'$ could be used to shift the phase transition to the correct location.

In Chapter 4 we then concentrated on the theoretical description of (axial-)vector

mesons by fundamental fields in an effective theory. Here, the ρ and a_1 meson were introduced in the spirit of Sakurai, i.e. as gauge bosons arising from a local $SU(2) \times SU(2)$ gauge symmetry. An additional Yukawa-type interaction to quark-antiquark fields then lead us to the so-called gauged linear sigma model with quarks. When describing fluctuations due to massive (axial-)vector mesons, this formalism had to be extended as here the known problems of ensuring transversality and convariance of the associated time-ordered product arise. The FRG formulation of the single-particle contribution of a vector meson propagator fulfilling these requirements and also the associated (modified) Ward identity described in Sec. 4.2.2 represents one main result of this work. In order to also account for an electromagnetic interaction and a coupling to baryon degrees of freedom, the gauged linear sigma model was finally extended by an additional $U(1)$ gauge symmetry and by means of the parity-doublet model, respectively.

The main results for (axial-)vector meson and electromagnetic spectral functions along the phase diagram of the respective models were presented in Chapter 5. Within the first setting in Sec. 5.2.1 the possible processes for the ρ meson were $\rho^* \to \pi+\pi$ and $\rho^* \to \psi+\bar{\psi}$ whereas for the a_1 meson we had the processes $a_1^* \to \pi+\sigma$, $a_1^* + \pi \to \sigma$, $a_1^* + \sigma \to \pi$ and $a_1^* \to \psi + \bar{\psi}$. With increasing temperature and/or quark chemical potential we observed various modifications in the ρ and a_1 meson spectral functions. Along the temperature axis at $\mu = 0$ MeV, the main effects were a broadening or melting of both spectral functions and a complete degeneracy at large temperature which could be connected to the restoration of chiral symmetry as the associated order parameter was obtained within the same framework. This behavior could also be seen in the temperature-dependent Euclidean masses and the pole masses of the ρ and a_1 meson. Close to the critical endpoint of the quark-meson model, the dropping sigma mass lead to sensitive modifications in the a_1 spectral function, namely the abrupt lowering of the threshold of the process $a_1^* \to \pi + \sigma$ which could be clearly identified as signature for the CEP of the model.

The developed formalism of describing fluctuating (axial-)vector mesons then allowed to include additional processes involving (axial-)vector mesons, $\rho^* \to a_1 + \pi$ and $\rho^* + \pi/a_1 \to a_1/\pi$ for the ρ meson and $a_1^* \to \rho + \pi$, $a_1^* + \pi/\rho \to \rho/\pi$, $a_1^* \to a_1 + \sigma$ and $a_1^* + \sigma/a_1 \to a_1/\sigma$ for the a_1 meson. These additional processes lead to more involved structures in the in-medium spectral functions as we have more possible capture processes at finite temperature in this setting. However, the overall in-medium-induced effects are similar to the previous setting, namely a broadening and successive degeneracy with increasing temperature and a dropping $\pi + \sigma$ threshold in the a_1 spectral function in the region close to the CEP.

This setting was in Sec. 5.2.3 extended by means of replacing the quark-antiquark degrees of freedom with fields for the nucleon and its parity partner. In this way, unphysical quark-antiquark thresholds in the hadronic phase, present in the ρ and a_1 spectral functions in the previous settings, could be removed whereby all processes including the new ones, namely $\rho^* \to N + \bar{N}$, $\rho^* + \bar{N}, N \to N, \bar{N}$ and $a_1^* \to N + \bar{N}$, $a_1^* + \bar{N}, N \to N, \bar{N}$, are physically realized in the hadronic phase of the phase diagram. The absence of the quark thresholds lead to more peaked ρ and a_1 spectral functions where we also saw new decay thresholds at large frequencies and new contributions at intermediate frequencies related to in-medium vector meson-nucleon scattering processes. Close to the chiral critical endpoint we observed a broadening

of the a_1 spectral function. The lowering of the $\pi + \sigma$ threshold in the a_1 spectral function was covered by increasing capture-contributions related to the process $a_1^* + \bar{N}, N \to N, \bar{N}$.

As last result in this main chapter we presented electromagnetic spectral functions at finite temperature and chemical potential. Here, the physical electromagnetic two-point function is given as mixture of the bare ρ, the ρ-photon and the bare photon two-point function in which we in a first step implemented only the decay processes $\pi + \pi$ and $\psi + \bar{\psi}$. In the temperature and chemical-potential dependent electromagnetic spectral functions we observed a broadening with increasing temperature, in the region of the chiral CEP we only saw small modifications. This could be explained by a shortcoming of the used ansatz and truncation since we would need a dressed a_1 propagator in the ρ two-point function in order to identify signatures at the CEP which are induced by a dropping sigma mass.

The numerical framework of computing self-consistent spectral functions presented in Chapter 6 can be seen as the third main result of this work. The idea here was to reinsert full k-dependent propagators into the loops on the right side of the equations using the spectral representation for regulated Euclidean propagators. We showed that this reconstruction procedure, with a deviation of 8% at most, works quite well. As an example we computed pion and sigma spectral functions within the $O(4)$ model where we could identify a first non-trivial decay threshold in the pion spectral function related to the process $\pi^* \to \sigma + \pi \simeq 3\pi$. One advantage of this approach is the straightforward generalization to finite temperature. Here we saw that the pion-peak got broader and both spectral functions tended to degenerate completely at $T = 800$ MeV.

From a technical point of view, an important next step is to transfer this idea of self-consistent solutions of analytically continued flow equations also to (axial-)vector meson spectral functions as this is needed to identify non-trivial structures, for example signatures for critical physics in the electromagnetic spectral function via fully backcoupled a_1 propagators. Beside further phenomenological extensions of the used hadronic model, for example towards a quantitative description of nuclear matter or via the inclusion of Delta resonances, a future aim is to integrate realistic spectral functions into transport approaches in order to calculate dilepton spectra and to study how critical physics like phase transitions or a critical endpoint could manifest itself in these spectra. This analysis could finally give hints to specify features of the QCD phase diagram from actual measured electromagnetic spectra in heavy-ion collisions.

A

Notations and Conventions

Dirac algebra

In the derivation and calculation of FRG flow equations in Euclidean space-time we use the chiral representation of Euclidean gamma matrices,

$$\gamma^0 = \begin{pmatrix} 0 & \mathbb{1} \\ \mathbb{1} & 0 \end{pmatrix}, \qquad \gamma^i = \begin{pmatrix} 0 & \mathrm{i}\sigma^i \\ -\mathrm{i}\sigma^i & 0 \end{pmatrix}, \tag{A.1}$$

where the Pauli matrices σ^i are given by

$$\sigma^1 = \begin{pmatrix} 0 & 1 \\ 1 & 0 \end{pmatrix}, \qquad \sigma^1 = \begin{pmatrix} 0 & -\mathrm{i} \\ \mathrm{i} & 0 \end{pmatrix}, \qquad \sigma^1 = \begin{pmatrix} 1 & 0 \\ 0 & -1 \end{pmatrix}. \tag{A.2}$$

These gamma matrices are hermitian and obey the Euclidean Clifford algebra,

$$\{\gamma^\mu, \gamma^\nu\} = 2\delta^{\mu\nu}\mathbb{1}\,. \tag{A.3}$$

Additionally we define

$$\gamma^5 = \gamma^0\gamma^1\gamma^2\gamma^3 = \begin{pmatrix} \mathbb{1} & 0 \\ 0 & -\mathbb{1} \end{pmatrix}. \tag{A.4}$$

Matsubara Sum and integrals

For integrations we define the shorthand notations

$$\int_p \equiv \int \frac{d^4p}{(2\pi)^4}\,, \qquad \int_x \equiv \int d^4x\,. \tag{A.5}$$

In Euclidean space-time, finite temperature is introduced via

$$\int \frac{d^4p}{(2\pi)^4} \quad \longrightarrow \quad \sum\!\!\!\!\!\!\int_p \equiv T\sum_{n\in\mathbb{Z}} \int \frac{d^3p}{(2\pi)^3}\,, \tag{A.6}$$

where the sum runs over discrete bosonic and fermionic Matsubara modes

$$p^B_{0,n} = 2n\pi T\,, \qquad p^F_{0,n} = 2(n+1)\pi T\,. \tag{A.7}$$

Fourier transform and functional calculus

For Fourier transformations of bosonic and fermionic fields we use the conventions

$$\phi(x) = \int_p \phi(p) \mathrm{e}^{\mathrm{i}px}\,, \qquad \phi(p) = \int_x \phi(x) \mathrm{e}^{-\mathrm{i}px}\,, \tag{A.8}$$

$$\psi(x) = \int_p \psi(p) \mathrm{e}^{\mathrm{i}px}\,, \qquad \psi(p) = \int_x \psi(x) \mathrm{e}^{-\mathrm{i}px}\,, \tag{A.9}$$

$$\bar{\psi}(x) = \int_p \bar{\psi}(p) \mathrm{e}^{-\mathrm{i}px}\,, \qquad \bar{\psi}(p) = \int_p \bar{\psi}(x) \mathrm{e}^{\mathrm{i}px}\,. \tag{A.10}$$

Analogously, the Fourier transformation of two-point functions is defined as (here for a bosonic two-point function, as example)

$$\Gamma^{(2)}_{\phi_a\phi_b}(p,p') = \int_x \int_y \Gamma^{(2)}_{\phi_a\phi_b}(x,y)\, \mathrm{e}^{-\mathrm{i}px}\, \mathrm{e}^{-\mathrm{i}p'y}\,. \tag{A.11}$$

The basic functional derivative is given by

$$\frac{\delta\phi_a(x)}{\delta\phi_b(x')} = \delta_{ab}\, \delta^{(4)}(x-x')\,, \tag{A.12}$$

where useful representations of the Dirac delta function are

$$\int_x \mathrm{e}^{\mathrm{i}(p+p')x} = (2\pi)^4 \delta^{(4)}(p+p')\,, \tag{A.13}$$

$$\int_p \mathrm{e}^{\mathrm{i}p(x+x')} = \delta^{(4)}(x+x')\,. \tag{A.14}$$

The following small calculation is useful for the derivation of flow equations,

$$\frac{\delta}{\delta\phi_b(x')}\partial_\mu\phi_a(x) = \partial_\mu \frac{\delta\phi_a(x)}{\delta\phi_b(x')} = \partial_\mu \delta^{(4)}(x-x')\delta_{ab} = \delta_{ab}\int_p (\mathrm{i}p_\mu)\mathrm{e}^{\mathrm{i}p(x-x')}\,. \tag{A.15}$$

Euclidean and Minkowski space-time

Throughout this work we use the notation p_0 as zeroth component of Euclidean momenta and ω as zeroth component in Minkowski space-time. These two are related to each other by

$$p_0 \longrightarrow -\mathrm{i}\omega\,. \tag{A.16}$$

For a four-vector we therefore have

$$p_E^2 = p_0^2 + \vec{p}^{\,2} \longrightarrow -p_M^2 = -(\omega^2 - \vec{p}^{\,2})\,, \tag{A.17}$$

where a four-vector without explicit index is always meant to be an Euclidean one. With the definition of an additional global minus sign we obtain the (free) retarded propagator out of the Euclidean one as (here for a scalar field)

$$D^E(p_0,\vec{p}) = \frac{1}{p_0^2 + \vec{p}^{\,2} + m^2} \quad \longrightarrow \quad D^R(\omega,\vec{p}) = \frac{1}{(\omega+\mathrm{i}\epsilon)^2 - \vec{p}^{\,2} - m^2}\,. \tag{A.18}$$

For the transverse part of the single-particle contribution of the massive vector meson propagator discussed in Sec. 4.2.2 we have for the zeroth and the spatial components, respectively

$$D_{00}^{E,V}(p_0,\vec{p}) = -\frac{1}{m^2}\frac{p_E^2\,\delta_{00} - p_0 p_0}{p_E^2 + m^2} \quad \longrightarrow \quad D_{00}^{R,V}(\omega,\vec{p}) = \frac{1}{m^2}\frac{p_M^2\,g_{00} - \omega^2}{(\omega+\mathrm{i}\epsilon)^2 - \vec{p}^{\,2} - m^2}\,, \tag{A.19}$$

$$D_{ij}^{E,V}(p_0,\vec{p}) = -\frac{1}{m^2}\frac{p_E^2\,\delta_{ij} - p_i p_j}{p_E^2 + m^2} \quad \longrightarrow \quad D_{ij}^{R,V}(\omega,\vec{p}) = -\frac{1}{m^2}\frac{p_M^2\,g_{ij} - p_i p_j}{(\omega+\mathrm{i}\epsilon)^2 - \vec{p}^{\,2} - m^2}\,, \tag{A.20}$$

with the metric tensor defined as in [123], $g_{\mu\nu} = \mathrm{diag}(1,-1,-1,-1)$. In the actual calculation we first project on the transverse part via Euclidean projectors in Euclidean space-time and after this we perform the analytic continuation to obtain the retarded two-point function and propagator, respectively. The Euclidean projectors are given by

$$\Pi_{\mu\nu}^{T}(p) = \frac{\delta_{\mu\nu} - p_\mu p_\nu}{p^2}\,, \qquad \Pi_{\mu\nu}^{L}(p) = \frac{p_\mu p_\nu}{p^2}\,. \tag{A.21}$$

Useful relations for Dirac delta functions

The following relations are useful for performing the limit $\epsilon \to 0$ in the imaginary part of retarded two-point functions, discussed in App. C,

$$\delta(x) = \lim_{\epsilon\to 0}\frac{1}{\pi}\frac{\epsilon}{\epsilon^2 + x^2}\,, \qquad \delta'(x) = -\lim_{\epsilon\to 0}\frac{1}{\pi}\frac{2x\epsilon}{(\epsilon^2 + x^2)^2}\,, \tag{A.22}$$

$$\delta(x(k)) = \sum_{k_0}\frac{1}{|x'(k_0)|}\delta(k-k_0)\,, \quad \delta'(x(k)) = \sum_{k_0}\frac{1}{|x'(k_0)|}\frac{\delta'(k-k_0)}{x'(k)}\,. \tag{A.23}$$

B

Derivation of Flow Equations

In this appendix we discuss details concerning the derivation of flow equations within the FRG framework. We will first list all objects which enter the flow equations and will then discuss how to derive flow equations for the specific k-dependent quantities.

B.1 Regulators and Euclidean Propagators

Regulator functions

Throughout this work we use sharp, three-dimensional Litim regulators [63] which allow for an analytic evaluation of Matsubara sums. More explicitly, we employ the following regulator functions for (pseudo-)scalar mesons, (axial-)vector mesons, quark-antiquarks and nucleons,

$$R_{\sigma/\pi,k}\,(p) = (k^2 - \vec{p}^{\,2})\,\Theta(k^2 - \vec{p}^{\,2})\,, \tag{B.1}$$

$$R^{T,L}_{\rho/a_1,k}(p) = \frac{-m^2_{0,k}}{p^2}\,(k^2 - \vec{p}^{\,2})\,\Pi^{T,L}_{\mu\nu}(p)\,\Theta(k^2 - \vec{p}^{\,2})\,, \tag{B.2}$$

$$R_{\psi,k} \quad (p) = \mathrm{i}\not{p}\,(\sqrt{k^2/\vec{p}^{\,2}} - 1)\,\Theta\left(k^2 - \vec{p}^{\,2}\right)\,, \tag{B.3}$$

$$R_{N,k} \quad (p) = -\mathrm{i}\not{p}\,(\sqrt{k^2/\vec{p}^{\,2}} - 1)\,\Theta\left(k^2 - \vec{p}^{\,2}\right)\,. \tag{B.4}$$

We note that the minus sign in Eq. (B.3) compared to Eq. (B.4) is due to a different definition of the corresponding two-point function, which does not matter in the calculations in this work as we only have pure fermion loops in the flow equations.

Euclidean regulated propagators

The Euclidean regulated propagators, in general defined by

$$D^E_{\alpha,k}(p) = \left(\Gamma^{(2)}_{\alpha,k}(p) + R_{\alpha,k}(p)\right)^{-1}\,, \quad \text{with} \quad \alpha \in \{\sigma, \pi, \rho, a_1, \psi, N\}\,, \tag{B.5}$$

are explicitly given as

$$D^E_{\sigma/\pi,k}(p) = \frac{\Theta(k^2-\vec{p}^2)}{p_0^2+k^2+m^2_{\sigma/\pi}} + \frac{\Theta(\vec{p}^2-k^2)}{p^2+m^2_{\sigma/\pi}}\,, \tag{B.6}$$

$$\begin{aligned} D^E_{\rho/a_1,k}(p) =& \frac{\Theta(k^2-\vec{p}^2)}{m^2_{0,k}}\left(\frac{-p^2}{p_0^2+k^2+m^2_{\rho/a_1,k}}\Pi^T_{\mu\nu}(p) + \frac{-p^2}{p_0^2+k^2+m^2_{l,\rho/a_1,k}}\Pi^L_{\mu\nu}(p)\right)\,, \\ &+ \frac{\Theta(\vec{p}^2-k^2)}{m^2_{0,k}}\left(\frac{-p^2}{p^2+m^2_{\rho/a_1,k}}\Pi^T_{\mu\nu}(p) + \frac{-p^2}{p^2+m^2_{l,\rho/a_1,k}}\Pi^L_{\mu\nu}(p)\right)\,, \end{aligned} \tag{B.7}$$

$$D^E_{\psi,k}(p) = \frac{\Theta(k^2-\vec{p}^2)}{m^2_\psi+(p_0+\mathrm{i}\mu)^2+k^2}\left(m_\psi - \mathrm{i}\gamma_0(p_0+\mathrm{i}\mu) - \mathrm{i}\not{\vec{p}}\sqrt{k^2/\vec{p}^2}\right)\,, \tag{B.8}$$

$$+ \frac{\Theta(\vec{p}^2-k^2)}{m^2_\psi+(p_0+\mathrm{i}\mu)^2+\vec{p}^2}\left(m_\psi - \mathrm{i}\gamma_0(p_0+\mathrm{i}\mu) - \mathrm{i}\not{\vec{p}}\right)\,. \tag{B.9}$$

For the nucleon propagator we only show a more general expression as it is non-diagonal in field space and therefore a more complicated and lengthy expression,

$$D^E_{N,k}(p) = \left[\begin{pmatrix} -\mathrm{i}\not{p} - \gamma_0\mu_B + h_1\sigma & m_{0,B}\gamma_5 \\ -m_{0,B}\gamma_5 & -\mathrm{i}\not{p} - \gamma_0\mu_B + h_2\sigma \end{pmatrix} + \mathbb{1}R_{N,k}(p)\right]^{-1}\,. \tag{B.10}$$

Euclidean particle energies and masses

The k-dependent Euclidean particle masses appearing in these propagators are defined as

$$m^2_{\sigma,k} = 2\,U_k'(\phi_0^2) + 4\,\phi_0^2\,U_k''(\phi_0^2)\,, \tag{B.11}$$

$$m^2_{\pi,k} = 2\,U_k'(\phi_0^2)\,, \tag{B.12}$$

$$m^2_{\rho,k} = m^2_{Vk}\,, \tag{B.13}$$

$$m^2_{a_1,k} = m^2_{V,k} + g^2\phi_0^2\,, \tag{B.14}$$

$$m^2_{l,\rho,k} = \xi\, m^2_{\rho,k}\,\Lambda^2/k^2\,, \tag{B.15}$$

$$m^2_{l,a_1,k} = \xi\, m^2_{a_1,k}\,\Lambda^2/k^2\,, \tag{B.16}$$

$$m^2_{\psi,k} = h^2\phi_0^2\,, \tag{B.17}$$

where ϕ_0 is meant to be the global minimum of the effective potential U_k and U_k', U_k'' the first and second derivative with respect to the chirally invariant ϕ^2. The longitudinal masses $m_{l,\rho,k}$ and $m_{l,a_1,k}$ contain a dimensionless scaling factor ξ which is usually chosen to be 5-10, cf. Sec. 4.2.2. The associated Euclidean particle energies are defined by

$$E^2_{\alpha,k} = m^2_{\alpha,k} + k^2\,, \quad \text{with} \quad \alpha \in \{\sigma,\pi,\rho,a_1,\psi,N\}\,. \tag{B.18}$$

The masses of the nucleon and its parity partner are given by

$$m^2_{B_1,k} = \frac{1}{2}\left(+(h_1-h_2)\sigma_0 + \sqrt{4m^2_{0,B}+(h_1+h_2)^2\sigma_0^2}\right)^2\,, \tag{B.19}$$

$$m^2_{B_2,k} = \frac{1}{2}\left(-(h_1-h_2)\sigma_0 + \sqrt{4m^2_{0,B}+(h_1+h_2)^2\sigma_0^2}\right)^2\,, \tag{B.20}$$

whereby the corresponding energies read

$$E^2_{B_1,k} = \frac{1}{2}\Big(2k^2 + 2m^2_{0,B} + h_1^2\sigma_0^2 + h_2^2\sigma_0^2 + \sigma_0(h_1-h_2)\sqrt{\sigma_0^2(h_1+h_2)^2 + 4m^2_{0,B}}\Big)\,, \tag{B.21}$$

$$E^2_{B_2,k} = \frac{1}{2}\Big(2k^2 + 2m^2_{0,B} + h_1^2\sigma_0^2 + h_2^2\sigma_0^2 - \sigma_0(h_1-h_2)\sqrt{\sigma_0^2(h_1+h_2)^2 + 4m^2_{0,B}}\Big)\,. \tag{B.22}$$

B.2 Explicit Expressions for Vertex Functions

The vertex functions $\Gamma_k^{(3)}$ and $\Gamma_k^{(4)}$ are in our setting obtained by taking three and four functional derivatives of the ansatz for the effective average action with respect to the respective fields. Therefore we first express the different parts of the ansatz from Eq. (4.16) explicitly in terms of the fields,

$$\frac{1}{4}m^2_{v,k}\mathrm{Tr}V_\mu V^\mu = \frac{1}{2}m^2_{V,k}\left[(\vec{\rho}^{\,\mu})^2 + (\vec{a}_1^{\,\mu})^2\right]\,, \tag{B.23}$$

$$-\mathrm{i}gV_\mu\phi\partial_\mu\phi = g\left[(\vec{\rho}^{\,\mu}\times\vec{\pi})\,\partial_\mu\vec{\pi} - \sigma\vec{a}_1^{\,\mu}\partial_\mu\vec{\pi} + \vec{a}_1^{\,\mu}\vec{\pi}\partial_\mu\sigma\right]\,, \tag{B.24}$$

$$-\frac{1}{2}g^2V_\mu\phi V_\mu\phi = \frac{1}{2}g^2\left[(\vec{\rho}^{\,\mu}\times\vec{\pi} - \sigma\vec{a}_1^{\,\mu})^2 + (\vec{a}_1^{\,\mu}\vec{\pi})^2\right]\,, \tag{B.25}$$

$$-\frac{1}{2}\mathrm{i}g\mathrm{Tr}\partial_\mu V_\nu[V_\mu,V_\nu] = g\big[\partial_\mu\vec{\rho}^{\,\nu}\,(\vec{\rho}^{\,\mu}\times\vec{\rho}^{\,\nu} + \vec{a}_1^{\,\mu}\times\vec{a}_1^{\,\nu}) \tag{B.26}$$

$$+\,\partial_\mu\vec{a}_1^{\,\nu}\,(\vec{\rho}^{\,\mu}\times\vec{a}_1^{\,\nu} + \vec{a}_1^{\,\mu}\times\vec{\rho}^{\,\nu})\,\big]\,, \tag{B.27}$$

$$\frac{1}{4}g^2\mathrm{Tr}V_\mu V_\nu[V_\mu,V_\nu] = \frac{1}{4}g^2\left[(\vec{\rho}^{\,\mu}\times\vec{\rho}^{\,\nu} + \vec{a}_1^{\,\mu}\times\vec{a}_1^{\,\nu})^2 + (\vec{\rho}^{\,\mu}\times\vec{a}_1^{\,\nu} + \vec{a}_1^{\,\mu}\times\vec{\rho}^{\,\nu})^2\right]\,. \tag{B.28}$$

An obvious term which is only consistent with global chiral symmetry and included for example in [121, 132] is given by

$$-\frac{1}{4}\tilde{g}\phi^2\mathrm{Tr}V_\mu V_\mu = \frac{1}{2}\tilde{g}\left[\left(\vec{\pi}^2+\sigma^2\right)\left((\vec{\rho}^{\,\mu})^2 + (\vec{a}_1^{\,\mu})^2\right)\right]\,. \tag{B.29}$$

In the present work we neglect the non-Abelian interaction terms Eq. (B.27) and Eq. (B.28) which would give rise to vector meson self-interactions. In the Euclidean flow these terms are suppressed due to the large masses. In the spectral functions they would only contribute at large frequencies and therefore play no decisive role in the qualitative study of spectral functions.

The explicit expressions for the relevant vertex functions $\Gamma_k^{(3)}$ and $\Gamma_k^{(4)}$read

$$\Gamma^{(3)}_{\bar{\psi}\psi\rho_i^\mu,k} = \mathrm{i}h_V\gamma^\mu\tau_i\,, \tag{B.30}$$

$$\Gamma^{(3)}_{\bar{\psi}\psi a_{1,i}^\mu,k} = \mathrm{i}h_V\gamma^\mu\gamma^5\tau_i\,, \tag{B.31}$$

$$\Gamma^{(3)}_{\pi_k\pi_j\rho_i^\mu,k}\left(q_{\pi_k},q_{\pi_j}\right) = -\mathrm{i}g\epsilon_{ijk}(q^\mu_{\pi_k}-q^\mu_{\pi_j})\Big(1-\frac{g^2\phi_0^2}{m^2_{a_1,k}}\Big)\,, \tag{B.32}$$

$$\Gamma^{(3)}_{\sigma\pi_j a_{1,i}^\mu,k}(q_\sigma,q_{\pi_j}) = \mathrm{i}g\delta_{ij}\Big[q^\mu_\sigma+q^\mu_{\pi_j}\Big(\frac{g^2\phi_0^2}{m^2_{a_1,k}}-1\Big)\Big]\,, \tag{B.33}$$

$$\Gamma^{(3)}_{\sigma a_{1,j}^\nu a_{1,i}^\mu,k} = 2g^2\phi_0\delta^{\mu\nu}\delta_{ij}\,, \tag{B.34}$$

$$\Gamma^{(3)}_{\pi_k\rho_j^\nu a_{1,i}^\mu,k} = -g^2\phi_0\delta^{\mu\nu}\epsilon_{ijk}\,, \tag{B.35}$$

$$\Gamma^{(4)}_{\pi_l\pi_k\rho_j^\nu\rho_i^\mu,k} = g^2\delta^{\mu\nu}\left(2\delta_{ij}\delta_{kl}-\delta_{ik}\delta_{jl}-\delta_{il}\delta_{jk}\right)\,, \tag{B.36}$$

$$\Gamma^{(4)}_{\pi_l\pi_k a_{1,j}^\nu a_{1,i}^\mu,k} = g^2\delta^{\mu\nu}\left(\delta_{ik}\delta_{jl}+\delta_{il}\delta_{jk}\right)\,, \tag{B.37}$$

$$\Gamma^{(4)}_{\sigma\sigma a_{1,j}^\nu a_{1,i}^\mu,k} = 2g^2\delta_{ij}\delta^{\mu\nu}\,. \tag{B.38}$$

From the model extensions discussed in Sec. 4.3.1 and Sec. 4.3.2 we get following additional vertices

$$\Gamma^{(3)}_{\bar{\psi}\psi A^\mu,k} = -\mathrm{i}e\gamma^\mu Q\,, \tag{B.39}$$

$$\Gamma^{(3)}_{\bar{N}N\rho_i^\mu,k} = \mathrm{i}h_\rho\gamma^\mu\tau_i\,, \tag{B.40}$$

$$\Gamma^{(3)}_{\bar{N}Na_{1,i}^\mu,k} = \mathrm{i}h_{a_1}\gamma^\mu\gamma^5\tau_i\,, \tag{B.41}$$

$$\Gamma^{(3)}_{\pi_j\pi_i A^\mu,k}\left(q_{\pi_i},q_{\pi_j}\right) = -\mathrm{i}e\epsilon_{3jk}(q^\mu_{\pi_i}-q^\mu_{\pi_j})\Big(1-\frac{g^2\phi_0^2}{m^2_{a_1,k}}\Big)\,, \tag{B.42}$$

$$\Gamma^{(4)}_{\pi_j\pi_i A^\nu A^\mu,k} = 2e\delta^{\mu\nu}\left(\delta_{ij}-\delta_{i3}\delta_{j3}\right)\,, \tag{B.43}$$

$$\Gamma^{(4)}_{\pi_k\pi_j\rho_i^\nu A^\mu,k} = eg\delta^{\mu\nu}\left(2\delta_{i3}\delta_{kj}-\delta_{3k}\delta_{ij}-\delta_{3j}\delta_{ik}\right)\,, \tag{B.44}$$

with charge matrix $Q=\mathrm{diag}(2/3,-1/3)$ and nucleon coupling matrices given by $h_\rho=\mathrm{diag}(h_1,h_2)$ and $h_{a_1}=\mathrm{diag}(h_1,-h_2)$.

The vertices used in the $O(4)$ model in Chapter 6 are given by

$$\Gamma^{(3)}_{\pi_j\pi_i\sigma,k} = 4\phi_0\delta_{i,j}U_k''\,, \tag{B.45}$$

$$\Gamma^{(3)}_{\sigma\sigma\sigma,k} = 12\phi_0U_k''+8\phi_0^3U_k^{(3)}\,, \tag{B.46}$$

$$\Gamma^{(4)}_{\pi_l\pi_k\pi_j\pi_i,k} = 4U_k''\left(\delta_{ij}\delta_{lk}+\delta_{ik}\delta_{jl}+\delta_{il}\delta_{jk}\right)\,, \tag{B.47}$$

$$\Gamma^{(4)}_{\sigma\sigma\sigma\sigma,k} = 12U_k''+48\phi_0^2U_k^{(3)}+16\phi_0^4U_k^{(4)}\,, \tag{B.48}$$

$$\Gamma^{(4)}_{\pi_j\pi_i\sigma\sigma,k} = \delta_{ij}\left(4U_k^{(2)}+8\phi_0^3U_k^{(3)}\right)\,, \tag{B.49}$$

with $U_k^{(n)}$ being the n-th derivative of the effective potential with respect to ϕ^2, evaluated at ϕ_0^2.

B.3 On the Derivation of Flow Equations

Effective potential

The flow equation of the effective potential in the quark-meson model presented in Sec. 3.2.1 is computed as follows,

$$\begin{aligned}\partial_k U_k &= \frac{1}{2}\mathrm{STr}\left[\partial_k R_k \left(\Gamma_k^{(2)} + R_k\right)^{-1}\right] \\ &= \frac{1}{2}\mathrm{Tr}\left\{\partial_k R_{k,B} \left(\Gamma_{k,B}^{(2)} + R_{k,B}\right)^{-1}\right\} - \mathrm{Tr}\left\{\partial_k R_{k,F} \left(\Gamma_{k,F}^{(2)} + R_{k,F}\right)^{-1}\right\} \\ &= \sum\!\!\!\!\!\!\int_q 2k \left(\frac{1}{q_0^2 + E_{\sigma,k}^2} + \frac{3}{q_0^2 + E_{\pi,k}^2}\right)\Theta(k^2 - \vec{q}^{\,2}) \\ &\qquad - N_\mathrm{c} N_\mathrm{f} \sum\!\!\!\!\!\!\int_q \frac{4}{(q_0 + \mathrm{i}\mu)^2 + E_\psi^2}\Theta(k^2 - \vec{q}^{\,2})\,. \end{aligned} \tag{B.50}$$

In these expressions, the integration over the internal three-momentum as well as the Matsubara sum can be performed analytically which allows for an expression in terms of bosonic and fermionic occupation numbers, see [160, 161] for the analytic evaluation of Matsubara sums. We end up with the flow equation already given in Eq. (3.9),

$$\begin{aligned}\partial_k U_k = \frac{k^4}{12\pi^2}\Bigg\{ &\frac{1 + 2\,n_B(E_{\sigma,k})}{E_{\sigma,k}} + \frac{3\,(1 + 2\,n_B(E_{\pi,k}))}{E_{\pi,k}} \\ &- \frac{4N_f N_c}{E_{\psi,k}}\left(1 - n_F(E_{\psi,k} - \mu) - n_F(E_{\psi,k} + \mu)\right)\Bigg\}, \end{aligned} \tag{B.51}$$

where the bosonic and fermionic occupation numbers are defined as

$$n_B(E) = \frac{1}{\mathrm{e}^{E/T} - 1}\,, \qquad n_F(E) = \frac{1}{\mathrm{e}^{E/T} + 1}\,. \tag{B.52}$$

In the flow equation for the effective potential of the parity-doublet model presented in Sec. 3.3.1 only the fermionic contribution changes as in this case we have the nucleon propagator instead of the quark propagator. We therefore obtain

$$(\partial_k U_k)_F = -\,\mathrm{Tr}\left\{D_{N,k}^E(p)\,\partial_k R_{N,k}(p)\right\} \tag{B.53}$$

$$= \frac{k^4}{12\pi^2}\frac{4N_f}{E_{B_1,k}\,E_{B_2,k}}\big(- (E_{B_1,k} + E_{B_2,k}) \tag{B.54}$$

$$+ E_{B_2,k}\,n_F(E_{B_1,k} - \mu) + E_{B_1,k}\,n_F(E_{B_2,k} - \mu) \tag{B.55}$$

$$+ E_{B_2,k}\,n_F(E_{B_1,k} + \mu) + E_{B_1,k}\,n_F(E_{B_2,k} + \mu)\big)\,. \tag{B.56}$$

Vector meson two-point functions

Flow equations for Euclidean two-point functions have the general form as discussed in Sec. 2.2.1 and more explicitly given in Eq. (2.24). The specific contributions to the ρ and a_1 two-point functions related to the different model-settings are illustrated diagrammatically in Fig. 5.2, Fig. 5.7 and Fig. 5.11. In order to extract the physical

transverse part of these two-point functions, we project the flow equations by using the transverse projector. This transverse projector can further be decomposed into a part parallel and a part vertical to the heat bath,

$$\partial_k \Gamma^{(2),\perp}_{\rho/a_1,k}(p) = \frac{1}{2(N_\mathrm{f}^2-1)} \operatorname{Tr}\left[\Pi^{T,\perp}_{\mu\nu}(p)\left(\partial_k \Gamma^{(2)}_{\rho/a_1,k}(p)\right)^{ij}_{\nu\sigma}\right], \tag{B.57}$$

$$\partial_k \Gamma^{(2),\parallel}_{\rho/a_1,k}(p) = \frac{1}{(N_f^2-1)} \operatorname{Tr}\left[\Pi^{T,\parallel}_{\mu\nu}(p)\left(\partial_k \Gamma^{(2)}_{\rho/a_1,k}(p)\right)^{ij}_{\nu\sigma}\right], \tag{B.58}$$

where $i,j \in 1,\ldots,(N_\mathrm{f}^2-1)$ are adjoint flavor indices. The three dimensional vertical and four dimensional parallel projection operators are defined by

$$\Pi^{T,\perp}_{\mu\nu}(p) = \begin{cases} 0 & \text{if } \mu=0 \text{ or } \nu=0 \\ \delta_{\mu\nu} - \frac{p_\mu p_\nu}{\vec{p}^2} & \text{else} \end{cases}, \tag{B.59}$$

$$\Pi^{T,\parallel}_{\mu\nu}(p) = \delta_{\mu\nu} - \frac{p_\mu p_\nu}{p^2} - \Pi^{T}_{\mu\nu}(p)\,, \tag{B.60}$$

with

$$\Pi^{T}_{\mu\nu}(p) = \Pi^{T,\perp}_{\mu\nu}(p) + \Pi^{T,\parallel}_{\mu\nu}(p) = \delta_{\mu\nu} - \frac{p_\mu p_\nu}{p^2}. \tag{B.61}$$

For vanishing external spatial momentum, $\vec{p}=0$, the vertical and parallel parts of the flow equations coincide,

$$\partial_k \Gamma^{(2),\perp}_{\rho/a_1,k}(p_0) = \partial_k \Gamma^{(2),\parallel}_{\rho/a_1,k}(p_0). \tag{B.62}$$

Since the flow equations $\partial_k \Gamma^{(2)}_{\rho/a_1,k}(p)$ can become quite complicated and lengthy, depending on the model-setting, we refrain from listing them in an explicit form in this work. However, for the first setting in Sec. 5.2.1 the explicit loop functions can be found in [41].

Projections: vector meson mass and wavefunction renormalizations

The Euclidean vector meson mass in the first setting in Sec. 5.2.1 and for the electromagnetic spectral functions in Sec. 5.3 is defined by the momentum independent part of the vector meson two-point function in the LPA Proca ansatz which is given by

$$\Gamma^{(2)}_{V,k} = (p^2 + m^2_{V,k})\,\Pi^{T}_{\mu\nu}(p)\,. \tag{B.63}$$

The flow equation for $m^2_{V,k}$ can thus be obtained by

$$\partial_k m^2_{V,k} = \frac{1}{2(N_f^2-1)} \lim_{p\to 0} \operatorname{Tr}\left[\Pi^{T,\perp}_{\mu\nu}(p)\left(\partial_k \Gamma^{(2)}_{\rho,k}(p)\right)^{ij}_{\nu\sigma}\right] = \partial_k m^2_{\rho,k}\,, \tag{B.64}$$

where the contributions to the flow of $\Gamma^{(2)}_{\rho,k}$ are illustrated in Fig. 5.2 and Fig. 5.14, respectively.

In the second and third setting in Sec. 5.2.2 and Sec. 5.2.3 the transverse part of the vector meson two-point function is given by

$$\Gamma^{(2)}_{V,k} = \frac{-m^2_{0,k}}{p^2}(p^2 + m^2_{V,k})\,\Pi^{T}_{\mu\nu}(p)\,. \tag{B.65}$$

Here we have to modify the prescription of extracting the vector meson mass $m^2_{V,k}$ from the flow of the two-point function. We start with the mass parameter $m^2_{0,k}$, for which the flow equation can be defined as follows,

$$\partial_k m^2_{0,k} = -\frac{1}{3(N_f^2-1)} \lim_{p\to 0} \frac{\partial}{\partial \left|\vec{p}\right|^2} \mathrm{Tr}\left[p^2\, \Pi^T_{\mu\nu}(p)\, \left(\partial_k \Gamma^{(2)}_{\rho,k}(p)\right)^{ij}_{\nu\sigma}\right] . \tag{B.66}$$

For the momentum derivative of the projected and traced flow equation we proceed as follows. We first take the limit $p_0 \to 0$ and then perform the derivative with respect to $\left|\vec{p}\right|^2$. After setting $\left|\vec{p}\right|^2$ to zero, we can finally integrate the spatial three-momentum and afterwards perform the Matsubara sum. After the integration we use $\partial_x \Theta(x) = \delta(x)$ and deal with terms that are proportional to $\Theta(x)\delta(x)$ by defining $\Theta(0) \equiv 1/2$.

In contrast, for defining the flow of wavefunction renormalization factors for (pseudo-)scalar mesons Z_k, appearing in the combination

$$\Gamma^{(2)}_k \sim Z_k\, p^2\,, \tag{B.67}$$

we perform two separate derivatives each with respect to $|\vec{p}|$, divided by 2. After the first $|\vec{p}|$-derivative we use the fact that all terms proportional to the δ distribution vanish. We then can proceed as for the flow for $m^2_{0,k}$. The flow for the wavefunction renormalization factor of the pion can then for example be obtained by

$$\partial_k Z_{\pi,k} = \frac{1}{2(N_f^2-1)} \lim_{p\to 0} \frac{\partial^2}{\partial \left|\vec{p}\right|^2} \mathrm{Tr}\left[\left(\partial_k \Gamma^{(2)}_{\pi,k}(p)\right)^{ij}\right] . \tag{B.68}$$

We are left with the flow equation for the vector meson mass $m^2_{V,k}$ from Eq. (B.65). For that we use the fact that the flow of the product of $m^2_{V,k}$ and $m^2_{0,k}$ vanishes,

$$\partial_k \left(m^2_{V,k} \cdot m^2_{0,k}\right) = -\frac{1}{3(N_f^2-1)} \lim_{p\to 0} \mathrm{Tr}\left[p^2\, \Pi^T_{\mu\nu}(p)\, \partial_k \left(\Gamma^{(2)}_{\rho,k}(p)\right)^{ij}_{\nu\sigma}\right] = 0\,. \tag{B.69}$$

From that we obtain the following flow equation for $m^2_{V,k}$,

$$\partial_k m^2_{V,k} = \partial_k m^2_{\rho,k} = -\frac{m^2_{V,k}}{m^2_{0,k}}\, \partial_k m^2_{0,k}\,. \tag{B.70}$$

All flow equations are traced and manipulated using the Mathematica packages *DoFun* [162] and *FormTracer* [163]. For the numerical implementation we mainly used the *GNU Scientific Library* (GSL) whereas for higher dimensional integrations we used the C package *Cubature*.

Explicit expressions for all flow equations and the involved objects used in this work can be found in the Mathematica file *flow_equations_cj.nb* which is handed out within this dissertation.

C

Properties of Retarded Two-Point Functions and Spectral Functions

In this appendix we discuss further important properties of retarded two-point functions and spectral functions.

On the definition of vector meson spectral functions

In order to extract spectral functions from analytically continued FRG flow equations we need the imaginary part of retarded (axial-)vector meson propagators. Therefore we have to convince ourselves that this can be done as one would naively expect, also in the presence of Schwinger and seagull terms, cf. Sec. 4.2.2.

The vector meson spectral function $\rho_V(s)$ is basically defined via the commutator of the vector field V_μ as

$$\langle V_\mu(x), V_\nu(0)\rangle = -\int_0^\infty ds\, \frac{s^2\rho_V(s)}{m_V^4}\left(g_{\mu\nu}+\frac{\partial_\mu\partial_\nu}{s}\right)\mathrm{i}\Delta(x;s)\,, \tag{C.1}$$

with the invariant delta function

$$\mathrm{i}\Delta(x;m^2) = \int_p \epsilon(p_0)\,2\pi\delta(p^2-m^2)\mathrm{e}^{-\mathrm{i}px}\,. \tag{C.2}$$

Its Fourier transformation is given by

$$\int_x \mathrm{e}^{\mathrm{i}px}\,\langle V_\mu(x), V_\nu(0)\rangle = -2\pi\epsilon(p_0)\Theta(p^2)\,\frac{p^2\rho_V(p^2)}{m_V^4}\left(p^2 g_{\mu\nu}-p_\mu p_\nu\right)\,. \tag{C.3}$$

By expressing the invariant delta function through the imaginary part of the retarded Green function,

$$\mathrm{i}\Delta(x;m^2) = -2\,\mathrm{Im}\,\Delta_R(x;m^2)\,, \tag{C.4}$$

we can write

$$\epsilon(p_0)\Theta(p^2)p^2\rho_V(p^2)\left(p^2 g_{\mu\nu} - p_\mu p_\nu\right) = \frac{1}{\pi}\int_0^\infty ds\, s^2\rho_V(s)\left(g_{\mu\nu} - \frac{p_\mu p_\nu}{s}\right)\mathrm{Im}\,\frac{-1}{(p_0+\mathrm{i}\epsilon)^2 - \vec{p}^2 - s}\,, \tag{C.5}$$

where we canceled the factor m_V^4 on both sides. Since the Fourier transform of $\mathrm{Im}\,\Delta_R(x;m^2)$ has support only at $p^2 = m^2$ we can trade powers of p^2 for matching powers of s, leading to

$$\epsilon(p_0)\Theta(p^2)\rho_V(p^2)\left(g_{\mu\nu} - \frac{p_\mu p_\nu}{p^2}\right) = -\frac{1}{\pi}\mathrm{Im}\int_0^\infty ds\,\frac{\rho_V(s)}{s}\frac{p^2 g_{\mu\nu} - p_\mu p_\nu}{(p_0+\mathrm{i}\epsilon)^2 - \vec{p}^2 - s}\,. \tag{C.6}$$

From this expression we see that we can safely extract the spectral function from the transversally projected retarded (axial-)vector meson propagator with spectral representation as in Eq. (4.23), i.e. for the transverse part of the full Feynman propagator of the form

$$D^V_{\mu\nu}(p) = -\mathrm{i}\int_0^\infty ds\,\frac{\rho_V(s)}{s}\int_p \mathrm{e}^{-\mathrm{i}px}\frac{p^2 g_{\mu\nu} - p_\mu p\nu}{(p_0+\mathrm{i}\epsilon)^2 - \vec{p}^2 - s}\,. \tag{C.7}$$

Analytic imaginary parts of retarded two-point functions

For the imaginary parts of the retarded two-point functions involved in the spectral functions in Chapter 5 it is possible to perform the limit $\epsilon \to 0$ in the definition of the retarded two-point function in Eq. (2.2.2) analytically.

Therefore the first step is to express the imaginary part of the loop functions in the flow equations for $\Gamma_k^{(2),R}$ in terms of Dirac delta functions and its derivatives respectively using Dirac-Sokhotsky identities,

$$\lim_{\epsilon\to 0}\mathrm{Im}\left(\frac{1}{\omega+\mathrm{i}\epsilon - E_\alpha \pm E_\beta}\right) \to -\pi\delta(\omega - E_\alpha \pm E_\beta)\,, \tag{C.8}$$

$$\lim_{\epsilon\to 0}\mathrm{Im}\left(\frac{1}{(\omega+\mathrm{i}\epsilon - E_\alpha \pm E_\beta)^2}\right) \to \pi\delta'(\omega - E_\alpha \pm E_\beta)\,. \tag{C.9}$$

As the particle energies E_α and E_β are k-dependent quantities, these delta functions together with the k-integral collapse to the $k = k_0$ values which are determined by

$$\omega - E_{\alpha,k} \pm E_{\beta,k} = 0\,. \tag{C.10}$$

The integrated flow equations for the imaginary part of $\Gamma_k^{(2),R}$ then reduce to the following form,

$$\begin{aligned}\int_{k_{\mathrm{UV}}}^{k_{\mathrm{IR}}} dk\,\partial_k \mathrm{Im}\Gamma_k^{(2)} &= \int_{k_{\mathrm{UV}}}^{k_{\mathrm{IR}}} dk\,\left(f(k)\delta(k-k_0) + g(k)\delta'(k-k_0)\right)\\ &= -f(k_0) + g'(k_0)\,.\end{aligned} \tag{C.11}$$

The used relations for delta functions and derivatives can be found in App. A.

Initial form of retarded two-point functions

In order to calculate spectral functions we first solve the real and imaginary parts of the retarded two-point functions separately. The retarded two-point functions are obtained from their Euclidean counterparts by applying the analytic continuation procedure described in Sec. 2.2.2. For the calculation in Sec. 5.2.1 we use the following ansatz at the UV scale $\Lambda = 1500$ MeV,

$$\Gamma^{(2),R}_{\rho,\Lambda}(\omega,\vec{p}) = (\omega + \mathrm{i}\epsilon)^2 - \vec{p}^{\,2} - m^2_{\rho,\Lambda}\,, \tag{C.12}$$

$$\Gamma^{(2),R}_{a_1,\Lambda}(\omega,\vec{p}) = (\omega + \mathrm{i}\epsilon)^2 - \vec{p}^{\,2} - m^2_{a_1,\Lambda}\,. \tag{C.13}$$

While for the imaginary part we perform the limit $\epsilon \to 0$ explicitly, cf. App. C, we use a small value $\epsilon = 0.1$ MeV or $\epsilon = 1$ MeV for the real part which is almost independent of this ϵ parameter. In the computation of electromagnetic two-point functions and spectral functions in Sec. 5.3 we use following ansatz,

$$\Gamma^{(2),R}_{\rho\rho,\Lambda}(\omega,\vec{p}) = (\omega + \mathrm{i}\epsilon)^2 - \vec{p}^{\,2} - m^2_{\rho,\Lambda}\,, \tag{C.14}$$

$$\Gamma^{(2),R}_{AA,\Lambda}(\omega,\vec{p}) = (\omega + \mathrm{i}\epsilon)^2 - \vec{p}^{\,2}\,, \tag{C.15}$$

$$\Gamma^{(2),R}_{\rho A,\Lambda}(\omega,\vec{p}) = 0\,. \tag{C.16}$$

In contrast, in the calculation with fluctuating (axial-)vector mesons in Sec. 5.2.2 and Sec. 5.2.3, we have used the following ansatz for the real and imaginary part,

$$\Gamma^{(2),R}_{\rho,\Lambda}(\omega) = m^2_{0,k}\left(1 + \frac{m^2_{\rho,k}}{(\epsilon - \mathrm{i}\omega)^2}\right), \tag{C.17}$$

$$\Gamma^{(2),R}_{a_1,\Lambda}(\omega) = m^2_{0,k}\left(1 + \frac{m^2_{a_1,k}}{(\epsilon - \mathrm{i}\omega)^2}\right). \tag{C.18}$$

Interpretation of loop functions

Expressing the loop functions in terms of Dirac delta functions and bosonic/fermionic occupation numbers allows for an easy interpretation related to the specific physical processes. These processes can thereby be divided into three different categories: vacuum processes, capture processes and particle-hole processes.

The vacuum processes $\omega \to E_\alpha + E_\beta$ and $E_\alpha + E_\beta \to \omega$ are associated to statistical weight factors of the form $(1 + n_B(E_\alpha) + n_B(E_\beta))$, where the delta functions in the imaginary part are given by

$$\delta(\omega - E_{\alpha,k} - E_{\beta,k})\,, \qquad \delta(\omega + E_{\alpha,k} + E_{\beta,k})\,. \tag{C.19}$$

Capture processes like $\omega + E_\alpha \to E_\beta$ and $\omega + E_\beta \to E_\alpha$ are only possible at finite temperature and give rise to statistical weight factors of the form $(\pm n_B(E_\alpha) \mp n_B(E_\alpha))$. The associated delta functions are given by

$$\delta(\omega + E_{\alpha,k} - E_{\beta,k})\,, \qquad \delta(\omega - E_{\alpha,k} + E_{\beta,k})\,. \tag{C.20}$$

Finally, particle-hole processes are proportional to the derivative of the occupation number, e.g. $n'_B(E_\alpha)$.

Bibliography

[1] M. Gell-Mann, *Symmetries of baryons and mesons*, *Phys. Rev.* **125** (1962) 1067.

[2] M. Gell-Mann, *A Schematic Model of Baryons and Mesons*, *Phys. Lett.* **8** (1964) 214.

[3] G. Zweig, *An SU(3) model for strong interaction symmetry and its breaking. Version 1*, .

[4] M. Y. Han and Y. Nambu, *Three-triplet model with double* SU(3) *symmetry*, *Phys. Rev.* **139** (1965) B1006.

[5] H. Fritzsch and M. Gell-Mann, *Current algebra: Quarks and what else?*, *eConf* **C720906V2** (1972) 135 [hep-ph/0208010].

[6] D. J. Gross and F. Wilczek, *Ultraviolet behavior of non-abelian gauge theories*, *Phys. Rev. Lett.* **30** (1973) 1343.

[7] H. D. Politzer, *Reliable perturbative results for strong interactions?*, *Phys. Rev. Lett.* **30** (1973) 1346.

[8] S. Bethke, *alphas 2016*, *Nuclear and Particle Physics Proceedings* **282-284** (2017) 149 .

[9] C. Gattringer and C. B. Lang, *Quantum chromodynamics on the lattice*, *Lect.Notes Phys.* **788** (2010) 1.

[10] P. de Forcrand, *Simulating QCD at finite density*, *PoS* **LAT2009** (2009) 010 [1005.0539].

[11] G. Aarts, *Complex Langevin dynamics and other approaches at finite chemical potential*, *PoS* **LATTICE2012** (2012) 017 [1302.3028].

[12] HotQCD collaboration, *The QCD crossover at zero and non-zero baryon densities from Lattice QCD*, *Nucl. Phys.* **A982** (2019) 847 [1807.05607].

[13] P. Braun-Munzinger and J. Wambach, *The Phase Diagram of Strongly-Interacting Matter*, *Rev.Mod.Phys.* **81** (2009) 1031 [0801.4256].

[14] M. A. Stephanov, *QCD phase diagram: An Overview*, *PoS* **LAT2006** (2006) 024 [hep-lat/0701002].

[15] K. Fukushima and T. Hatsuda, *The phase diagram of dense QCD*, *Rept. Prog. Phys.* **74** (2011) 014001 [1005.4814].

[16] M. Buballa and S. Carignano, *Inhomogeneous chiral condensates*, *Progress in Particle and Nuclear Physics* **81** (2015) 39 .

[17] B. C. Barrois, *Superconducting quark matter*, *Nuclear Physics B* **129** (1977) 390 .

[18] J. Berges and K. Rajagopal, *Color superconductivity and chiral symmetry restoration at nonzero baryon density and temperature*, *Nucl. Phys.* **B538** (1999) 215 [hep-ph/9804233].

[19] C. D. Roberts and A. G. Williams, *Dyson-Schwinger equations and their application to hadronic physics*, *Prog. Part. Nucl. Phys.* **33** (1994) 477 [hep-ph/9403224].

[20] R. Alkofer and L. von Smekal, *The Infrared behavior of QCD Green's functions: Confinement dynamical symmetry breaking, and hadrons as relativistic bound states*, *Phys.Rept.* **353** (2001) 281 [hep-ph/0007355].

[21] C. S. Fischer, *Infrared properties of QCD from Dyson-Schwinger equations*, *J. Phys.* **G32** (2006) R253 [hep-ph/0605173].

[22] C. S. Fischer and J. Luecker, *Propagators and phase structure of Nf=2 and Nf=2+1 QCD*, *Phys.Lett.* **B718** (2013) 1036 [1206.5191].

[23] J. Luecker, C. S. Fischer, L. Fister and J. M. Pawlowski, *Critical Point and Deconfinement from Dyson-Schwinger Equations*, *PoS* **CPOD2013** (2013) 057 [1308.4509].

[24] C. S. Fischer, J. Luecker and C. A. Welzbacher, *Locating the critical end point of QCD*, *Nucl. Phys.* **A931** (2014) 774 [1410.0124].

[25] C. S. Fischer, *Qcd at finite temperature and chemical potential from dyson-schwinger equations*, *Progress in Particle and Nuclear Physics* **105** (2019) 1 .

[26] M. Jarrell and J. Gubernatis, *Bayesian inference and the analytic continuation of imaginary-time quantum monte carlo data*, *Physics Reports* **269** (1996) 133 .

[27] M. Asakawa, T. Hatsuda and Y. Nakahara, *Maximum entropy analysis of the spectral functions in lattice QCD*, *Prog.Part.Nucl.Phys.* **46** (2001) 459 [hep-lat/0011040].

[28] R.-A. Tripolt, P. Gubler, M. Ulybyshev and L. Von Smekal, *Numerical analytic continuation of Euclidean data*, *Comput. Phys. Commun.* **237** (2019) 129 [1801.10348].

[29] H. J. Vidberg and J. W. Serene, *Solving the eliashberg equations by means ofn-point padé approximants*, *Journal of Low Temperature Physics* **29** (1977) 179.

[30] Y. Burnier and A. Rothkopf, *Bayesian Approach to Spectral Function Reconstruction for Euclidean Quantum Field Theories*, *Phys. Rev. Lett.* **111** (2013) 182003 [1307.6106].

[31] J. M. Pawlowski, *Aspects of the functional renormalisation group*, *Annals Phys.* **322** (2007) 2831 [hep-th/0512261].

[32] S. Floerchinger, *Analytic Continuation of Functional Renormalization Group Equations*, *JHEP* **1205** (2012) 021 [1112.4374].

[33] K. Kamikado, N. Strodthoff, L. von Smekal and J. Wambach, *Real-Time Correlation Functions in the O(N) Model from the Functional Renormalization Group*, *Eur.Phys.J.* **C74** (2014) 2806 [1302.6199].

[34] R.-A. Tripolt, N. Strodthoff, L. von Smekal and J. Wambach, *Spectral Functions for the Quark-Meson Model Phase Diagram from the Functional Renormalization Group*, *Phys.Rev.* **D89** (2014) 034010 [1311.0630].

[35] R.-A. Tripolt, L. von Smekal and J. Wambach, *Flow equations for spectral functions at finite external momenta*, *Phys.Rev.* **D90** (2014) 074031 [1408.3512].

[36] R.-A. Tripolt, L. von Smekal and J. Wambach, *Spectral functions and in-medium properties of hadrons*, 1605.00771.

[37] J. M. Pawlowski, N. Strodthoff and N. Wink, *Finite temperature spectral functions in the O(N)-model*, 1711.07444.

[38] R.-A. Tripolt, J. Weyrich, L. von Smekal and J. Wambach, *Fermionic spectral functions with the Functional Renormalization Group*, *Phys. Rev.* **D98** (2018) 094002 [1807.11708].

[39] Z. Wang and L. He, *Fermion spectral function in hot strongly interacting matter from the functional renormalization group*, *Phys. Rev.* **D98** (2018) 094031 [1808.08535].

[40] N. Strodthoff, *Self-consistent spectral functions in the O(N) model from the functional renormalization group*, *Phys. Rev.* **D95** (2017) 076002 [1611.05036].

[41] C. Jung, F. Rennecke, R.-A. Tripolt, L. von Smekal and J. Wambach, *In-Medium Spectral Functions of Vector- and Axial-Vector Mesons from the Functional Renormalization Group*, *Phys. Rev.* **D95** (2017) 036020 [1610.08754].

[42] J. Wambach, C. Jung, F. Rennecke, R.-A. Tripolt and L. von Smekal, *Spectral Functions from the Functional Renormalization Group*, *PoS* **CPOD2017** (2018) 077 [1712.02093].

[43] R.-A. Tripolt, C. Jung, N. Tanji, L. von Smekal and J. Wambach, *In-medium spectral functions and dilepton rates with the Functional Renormalization Group*, *Nucl. Phys.* **A982** (2019) 775 [1807.04952].

[44] J. Polonyi, *Lectures on the functional renormalization group method*, *Central Eur.J.Phys.* **1** (2003) 1 [hep-th/0110026].

[45] C. Bagnuls and C. Bervillier, *Exact renormalization group equations. an introductory review*, *Phys.Rept.* **348** (2001) 91 [hep-th/0002034].

[46] H. Gies, *Introduction to the functional RG and applications to gauge theories*, *Lect. Notes Phys.* **852** (2012) 287 [hep-ph/0611146].

[47] J. Berges, N. Tetradis and C. Wetterich, *Nonperturbative renormalization flow in quantum field theory and statistical physics*, *Phys.Rept.* **363** (2002) 223 [hep-ph/0005122].

[48] D. F. Litim and J. M. Pawlowski, *Non-perturbative thermal flows and resummations*, *JHEP* **11** (2006) 026 [hep-th/0609122].

[49] B. Delamotte, *An Introduction to the nonperturbative renormalization group*, *Lect. Notes Phys.* **852** (2012) 49 [cond-mat/0702365].

[50] O. J. Rosten, *Fundamentals of the Exact Renormalization Group*, *Phys. Rept.* **511** (2012) 177 [1003.1366].

[51] W. Metzner, M. Salmhofer, C. Honerkamp, V. Meden and K. Schönhammer, *Functional renormalization group approach to correlated fermion systems*, *Rev. Mod. Phys.* **84** (2012) 299.

[52] D. F. Litim, *Fixed Points of Quantum Gravity and the Renormalisation Group*, 0810.3675.

[53] M. Reuter and F. Saueressig, *Quantum Einstein Gravity*, *New J. Phys.* **14** (2012) 055022 [1202.2274].

[54] N. Christiansen, B. Knorr, J. M. Pawlowski and A. Rodigast, *Global Flows in Quantum Gravity*, *Phys. Rev.* **D93** (2016) 044036 [1403.1232].

[55] J. M. Pawlowski, M. Reichert, C. Wetterich and M. Yamada, *Higgs scalar potential in asymptotically safe quantum gravity*, 1811.11706.

[56] K. G. Falls, D. F. Litim and J. Schroeder, *Aspects of asymptotic safety for quantum gravity*, 1810.08550.

[57] J. M. Pawlowski, *The QCD phase diagram: Results and challenges*, *AIP Conf. Proc.* **1343** (2011) 75 [1012.5075].

[58] J. Braun, *Fermion interactions and universal behavior in strongly interacting theories*, *J.Phys.* **G39** (2012) 033001 [1108.4449].

[59] L. von Smekal, *Universal Aspects of QCD-like Theories*, *Nucl. Phys. Proc. Suppl.* **228** (2012) 179 [1205.4205].

[60] N. Strodthoff, *Phase Structure and Dynamics of QCD?A Functional Perspective*, *J. Phys. Conf. Ser.* **832** (2017) 012040 [1612.03807].

[61] C. Wetterich, *Exact evolution equation for the effective potential*, *Phys. Lett.* **B301** (1993) 90.

[62] M. Peskin and D. Schroeder, *An Introduction to Quantum Field Theory*. Westview Press, 1995.

[63] D. F. Litim, *Optimised renormalisation group flows*, *Phys. Rev.* **D64** (2001) 105007 [hep-th/0103195].

[64] H. Gies, *Introduction to the functional RG and applications to gauge theories*, *Lect. Notes Phys.* **852** (2012) 287 [hep-ph/0611146].

[65] E. Zeidler, *Quantum Field Theory I: Basics in Mathematics and Physics: A Bridge between Mathematicians and Physicists*. Springer Berlin Heidelberg, 2016.

[66] G. Baym and N. D. Mermin, *Determination of thermodynamic Green's functions*, *J. Math. Phys.* **2** (1961) 232.

[67] A. K. Das, *Finite temperature field theory*. World Scientific, 1997.

[68] J. Kapusta and C. Gale, *Finite-Temperature Field Theory: Principles and Applications*, Cambridge Monographs on Mathematical Physics. Cambridge University Press, 2006.

[69] G. Aarts and J. M. Martinez Resco, *Transport coefficients, spectral functions and the lattice*, *JHEP* **0204** (2002) 053 [hep-ph/0203177].

[70] R.-A. Tripolt, *Spectral Functions and Transport Coefficients from the Functional Renormalization Group*, Ph.D. thesis, TU Darmstadt, 2015.

[71] M. Mitter, J. M. Pawlowski and N. Strodthoff, *Chiral symmetry breaking in continuum QCD*, *Phys. Rev.* **D91** (2015) 054035 [1411.7978].

[72] A. K. Cyrol, M. Mitter, J. M. Pawlowski and N. Strodthoff, *Non-perturbative finite-temperature Yang-Mills theory*, 1708.03482.

[73] D. F. Litim, *Critical exponents from optimized renormalization group flows*, *Nucl. Phys.* **B631** (2002) 128 [hep-th/0203006].

[74] B.-J. Schaefer and J. Wambach, *The phase diagram of the quark meson model*, *Nucl. Phys.* **A757** (2005) 479 [nucl-th/0403039].

[75] B.-J. Schaefer, J. M. Pawlowski and J. Wambach, *The phase structure of the polyakov–quark-meson model*, *Phys. Rev.* **D76** (2007) 074023 [0704.3234].

[76] J.-P. Blaizot, R. Mendez-Galain and N. Wschebor, *Non perturbative renormalisation group and momentum dependence of n-point functions (I)*, *Phys.Rev.* **E74** (2006) 051116 [hep-th/0512317].

[77] J.-P. Blaizot, R. Mendez-Galain and N. Wschebor, *Non perturbative renormalization group and momentum dependence of n-point functions. II.*, *Phys.Rev.* **E74** (2006) 051117 [hep-th/0603163].

[78] A. J. Helmboldt, J. M. Pawlowski and N. Strodthoff, *Towards quantitative precision in the chiral crossover: masses and fluctuation scales*, *Phys. Rev.* **D91** (2015) 054010 [1409.8414].

[79] D. Jungnickel and C. Wetterich, *Effective action for the chiral quark-meson model*, *Phys.Rev.* **D53** (1996) 5142 [hep-ph/9505267].

[80] J. M. Pawlowski and F. Rennecke, *Higher order quark-mesonic scattering processes and the phase structure of QCD*, *Phys.Rev.* **D90** (2014) 076002 [1403.1179].

[81] R.-A. Tripolt, B.-J. Schaefer, L. von Smekal and J. Wambach, *Low-temperature behavior of the quark-meson model*, *Phys. Rev.* **D97** (2018) 034022 [1709.05991].

[82] K. Fukushima, *Chiral effective model with the polyakov loop*, *Phys.Lett.* **B591** (2004) 277.

[83] T. K. Herbst, J. M. Pawlowski and B.-J. Schaefer, *The phase structure of the Polyakov–quark-meson model beyond mean field*, *Phys. Lett.* **B696** (2011) 58 [1008.0081].

[84] D. Jido, M. Oka and A. Hosaka, *Chiral symmetry of baryons*, *Prog. Theor. Phys.* **106** (2001) 873 [hep-ph/0110005].

[85] J. Weyrich, N. Strodthoff and L. von Smekal, *Chiral mirror-baryon-meson model and nuclear matter beyond mean-field approximation*, *Phys. Rev.* **C92** (2015) 015214 [1504.02697].

[86] B. Friman, C. Hohne, J. Knoll, S. Leupold, J. Randrup et al., *The CBM physics book: Compressed baryonic matter in laboratory experiments*, *Lect.Notes Phys.* **814** (2011) 1.

[87] B. L. Ioffe, *Axial anomaly: The Modern status*, *Int. J. Mod. Phys.* **A21** (2006) 6249 [hep-ph/0611026].

[88] V. Koch, *Aspects of chiral symmetry*, *Int.J.Mod.Phys.* **E6** (1997) 203 [nucl-th/9706075].

[89] M. Gell-Mann, R. Oakes and B. Renner, *Behavior of current divergences under SU(3) x SU(3)*, *Phys.Rev.* **175** (1968) 2195.

[90] J. S. Schwinger, *A Theory of the Fundamental Interactions*, *Annals Phys.* **2** (1957) 407.

[91] M. Gell-Mann and M. Levy, *The axial vector current in beta decay*, *Nuovo Cim.* **16** (1960) 705.

[92] S. GASIOROWICZ and D. A. GEFFEN, *Effective lagrangians and field algebras with chiral symmetry*, *Rev. Mod. Phys.* **41** (1969) 531.

[93] R. D. Pisarski and F. Wilczek, *Remarks on the Chiral Phase Transition in Chromodynamics*, *Phys. Rev.* **D29** (1984) 338.

[94] K. Rajagopal and F. Wilczek, *Static and dynamic critical phenomena at a second order QCD phase transition*, *Nucl. Phys.* **B399** (1993) 395 [hep-ph/9210253].

[95] C. Jung, *Mesonic Spectral Functions of the Polyakov-Quark-Meson Model*, Master's thesis, TU Darmstadt, 2015.

[96] S. Carignano, M. Buballa and B.-J. Schaefer, *Inhomogeneous phases in the quark-meson model with vacuum fluctuations*, *Phys. Rev.* **D90** (2014) 014033 [1404.0057].

[97] J. Weyrich, *Quark and Nuclear Matter with Fluctuations*, Ph.D. thesis, JLU Giessen, 2018.

[98] T. K. Herbst, *Polyakov-loops and the QCD phase structure*, Ph.D. thesis, Graz U., 2012.

[99] C. Ratti, M. A. Thaler and W. Weise, *Phases of qcd: Lattice thermodynamics and a field theoretical model*, *Phys. Rev.* **D73** (2006) 014019 [hep-ph/0506234].

[100] T. K. Herbst, J. M. Pawlowski and B.-J. Schaefer, *On the phase structure and thermodynamics of qcd*, 1302.1426.

[101] K. Fukushima, *Phase diagrams in the three-flavor nambu-jona-lasinio model with the polyakov loop*, *Phys.Rev.* **D77** (2008) 114028 [0803.3318].

[102] J. Walecka, *A theory of highly condensed matter*, *Annals of Physics* **83** (1974) 491 .

[103] T. D. Lee and G. C. Wick, *Vacuum stability and vacuum excitation in a spin-0 field theory*, *Phys. Rev. D* **9** (1974) 2291.

[104] S. Weinberg, *Algebraic realizations of chiral symmetry*, *Phys. Rev.* **177** (1969) 2604.

[105] D. Jido, Y. Nemoto, M. Oka and A. Hosaka, *Chiral symmetry for positive and negative parity nucleons*, *Nucl. Phys.* **A671** (2000) 471 [hep-ph/9805306].

[106] T. D. Cohen and X. Ji, *Chiral multiplets of hadron currents*, *Phys. Rev. D* **55** (1997) 6870.

[107] B. Lee, *Chiral dynamics*, Documents on modern physics. Gordon and Breach Science Publishers, 1972.

[108] T. D. Cohen, R. J. Furnstahl and D. K. Griegel, *Quark and gluon condensates in nuclear matter*, *Phys. Rev. C* **45** (1992) 1881.

[109] S. Fiorilla, N. Kaiser and W. Weise, *Nuclear thermodynamics and the in-medium chiral condensate*, *Phys. Lett.* **B714** (2012) 251 [1204.4318].

[110] W. Weise, *Nuclear chiral dynamics and phases of QCD*, *Prog. Part. Nucl. Phys.* **67** (2012) 299 [1201.0950].

[111] J. J. Sakurai, *Theory of strong interactions*, *Annals of Physics* **11** (1960) 1.

[112] Y. Nambu, *Possible existence of a heavy neutral meson*, *Phys. Rev.* **106** (1957) 1366.

[113] W. R. Frazer and J. R. Fulco, *Effect of a pion-pion scattering resonance on nucleon structure*, *Phys. Rev. Lett.* **2** (1959) 365.

[114] U. G. Meissner, *Low-Energy Hadron Physics from Effective Chiral Lagrangians with Vector Mesons*, *Phys. Rept.* **161** (1988) 213.

[115] H. B. O'Connell, B. C. Pearce, A. W. Thomas and A. G. Williams, $\rho - \omega$ *mixing, vector meson dominance and the pion form-factor*, *Prog. Part. Nucl. Phys.* **39** (1997) 201 [hep-ph/9501251].

[116] R. Rapp and J. Wambach, *Chiral symmetry restoration and dileptons in relativistic heavy ion collisions*, *Adv. Nucl. Phys.* **25** (2000) 1 [hep-ph/9909229].

[117] J. Sakurai and G. Barry, *Currents and Mesons*, Chicago Lectures in Physics. University of Chicago Press, 1969.

[118] D. Schildknecht, *Vector meson dominance*, *Acta Phys. Polon.* **B37** (2006) 595 [hep-ph/0511090].

[119] B. W. Lee and H. T. Nieh, *Phenomenological Lagrangian for field algebra, hard pions, and radiative corrections*, *Phys. Rev.* **166** (1968) 1507.

[120] J. Eser, M. Grahl and D. H. Rischke, *Functional Renormalization Group Study of the Chiral Phase Transition Including Vector and Axial-vector Mesons*, *Phys. Rev.* **D92** (2015) 096008 [1508.06928].

[121] F. Rennecke, *Vacuum structure of vector mesons in qcd*, *Phys. Rev.* **D92** (2015) 076012 [1504.03585].

[122] N. Nakanishi and I. Ojima, *Covariant operator formalism of gauge theories and quantum gravity*, *World Sci. Lect. Notes Phys.* **27** (1990) 1.

[123] C. Itzykson and J. Zuber, *Quantum Field Theory*, Dover Books on Physics. Dover Publications, 2012.

[124] C. N. Yang and R. L. Mills, *Conservation of isotopic spin and isotopic gauge invariance*, *Phys. Rev.* **96** (1954) 191.

[125] G. Zweig, *An SU(3) model for strong interaction symmetry and its breaking. Version 2*, *Developments in the Quark Theory of Hadrons, Volume 1. Edited by D. Lichtenberg and S. Rosen. pp. 22-101* (1964) 22.

[126] V. E. Mouchrek-Santos, M. M. Ferreira and C. Miller, *Lorentz-violating nonminimal coupling in the Kroll-Lee-Zumino model and vector meson dominance*, 1808.02029.

[127] N. M. Kroll, T. D. Lee and B. Zumino, *Neutral vector mesons and the hadronic electromagnetic current*, *Phys. Rev.* **157** (1967) 1376.

[128] H. Gomm, O. Kaymakcalan and J. Schechter, *Anomalous spin-1-meson decays from the gauged wess-zumino term*, *Phys. Rev. D* **30** (1984) 2345.

[129] M. Bando, T. Kugo and K. Yamawaki, *Nonlinear realization and hidden local symmetries*, *Physics Reports* **164** (1988) 217 .

[130] M. Harada and K. Yamawaki, *Hidden local symmetry at loop: A New perspective of composite gauge boson and chiral phase transition*, *Phys. Rept.* **381** (2003) 1 [hep-ph/0302103].

[131] P. Ko and S. Rudaz, *Phenomenology of scalar and vector mesons in the linear σ model*, *Phys. Rev. D* **50** (1994) 6877.

[132] M. Urban, M. Buballa and J. Wambach, *Vector and axial vector correlators in a chirally symmetric model*, *Nucl. Phys.* **A697** (2002) 338 [hep-ph/0102260].

[133] J. Braun, L. Fister, J. M. Pawlowski and F. Rennecke, *From Quarks and Gluons to Hadrons: Chiral Symmetry Breaking in Dynamical QCD*, *Phys. Rev.* **D94** (2016) 034016 [1412.1045].

[134] D. Gross and R. Jackiw, *Construction of covariant and gauge invariant t? products*, *Nuclear Physics B* **14** (1969) 269 .

[135] T. Watanabe, *Covariant t* products and schwinger terms*, *Progress of Theoretical Physics* **47** (1972) 2077.

[136] J. Schwinger, *Field theory commutators*, *Phys. Rev. Lett.* **3** (1959) 296.

[137] S. G. Brown, *Covariance and the cancellation of schwinger and seagull terms in applications of current algebras*, *Physical Review* **158** (1967) 1444.

[138] D. F. Litim and J. M. Pawlowski, *On gauge invariant wilsonian flows*, *in The Exact Renormalization Group, Eds. Krasnitz et al., World Scientific* (1999) 168 [hep-th/9901063].

[139] A. Drees, *Dileptons and Photons at RHIC Energies*, *Nucl. Phys.* **A830** (2009) 435C [0909.4976].

[140] R. Rapp and H. van Hees, *Thermal Dileptons as Fireball Thermometer and Chronometer*, *Phys. Lett.* **B753** (2016) 586 [1411.4612].

[141] N. Collaboration, *Na60 results on thermal dimuons*, *The European Physical Journal C* **61** (2009) 711.

[142] H. J. Specht, *Thermal dileptons from hot and dense strongly interacting matter*, *AIP Conference Proceedings* **1322** (2010) 1 [https://aip.scitation.org/doi/pdf/10.1063/1.3541982].

[143] R. Vogt, *J / psi suppression in P + Pb collisions: A New look at hadrons versus plasma*, *Phys. Lett.* **B430** (1998) 15 [hep-ph/9708294].

[144] T. Matsui and H. Satz, *J/psi suppression by quark-gluon plasma formation*, *Physics Letters B* **178** (1986) 416 .

[145] R. D. Pisarski, *Phenomenology of the Chiral Phase Transition*, *Phys. Lett.* **B110** (1982) 155.

[146] R. D. Pisarski, *Where does the ρ go? chirally symmetric vector mesons in the quark-gluon plasma*, *Phys. Rev. D* **52** (1995) R3773.

[147] R. Rapp, J. Wambach and H. van Hees, *The Chiral Restoration Transition of QCD and Low Mass Dileptons*, *Landolt-Bornstein* **23** (2010) 134 [0901.3289].

[148] G. Brown and M. Rho, *Scaling effective Lagrangians in a dense medium*, *Phys.Rev.Lett.* **66** (1991) 2720.

[149] CERES Collaboration collaboration, *Enhanced production of low-mass electron pairs in 200 gev/nucleon s-au collisions at the cern super proton synchrotron*, *Phys. Rev. Lett.* **75** (1995) 1272.

[150] R. Rapp, G. Chanfray and J. Wambach, *Rho meson propagation and dilepton enhancement in hot hadronic matter*, *Nucl. Phys.* **A617** (1997) 472 [hep-ph/9702210].

[151] P. M. Hohler and R. Rapp, *Is ρ-Meson Melting Compatible with Chiral Restoration?*, *Phys. Lett.* **B731** (2014) 103 [1311.2921].

[152] L. D. McLerran and T. Toimela, *Photon and dilepton emission from the quark-gluon plasma: Some general considerations*, *Phys. Rev. D* **31** (1985) 545.

[153] H. A. Weldon, *Reformulation of finite-temperature dilepton production*, *Phys. Rev. D* **42** (1990) 2384.

[154] T. D. Cohen, *Functional integrals for QCD at nonzero chemical potential and zero density*, *Phys.Rev.Lett.* **91** (2003) 222001 [hep-ph/0307089].

[155] R. A. Tripolt, I. Haritan, J. Wambach and N. Moiseyev, *Threshold energies and poles for hadron physical problems by a model-independent universal algorithm*, *Phys. Lett.* **B774** (2017) 411 [1610.03252].

[156] R. Rapp, *Dilepton Spectroscopy of QCD Matter at Collider Energies*, *Adv. High Energy Phys.* **2013** (2013) 148253 [1304.2309].

[157] N. Tetradis and C. Wetterich, *Critical exponents from effective average action*, *Nucl. Phys.* **B422** (1994) 541 [hep-ph/9308214].

[158] T. R. Morris and M. D. Turner, *Derivative expansion of the renormalization group in O(N) scalar field theory*, *Nucl. Phys.* **B509** (1998) 637 [hep-th/9704202].

[159] S. Nagy, *Critical exponents of the O(N) model in the infrared limit from functional renormalization*, *Phys. Rev.* **D86** (2012) 085020 [1201.1625].

[160] A. Nieto, *Evaluating sums over the Matsubara frequencies*, *Comput. Phys. Commun.* **92** (1995) 54 [hep-ph/9311210].

[161] O. Espinosa, *On the evaluation of Matsubara sums*, *arXiv e-prints* (2009) arXiv:0905.3366 [0905.3366].

[162] M. Q. Huber and J. Braun, *Algorithmic derivation of functional renormalization group equations and Dyson-Schwinger equations*, *Comput. Phys. Commun.* **183** (2012) 1290 [1102.5307].

[163] A. K. Cyrol, M. Mitter and N. Strodthoff, *FormTracer - A Mathematica Tracing Package Using FORM*, *Comput. Phys. Commun.* **219** (2017) 346 [1610.09331].

Acknowledgments

Zuallererst möchte ich mich bei Prof. Dr. Lorenz von Smekal bedanken, der mir die Möglichkeit gab mich mit diesem interessanten Themenfeld zu befassen und der mir in all den Jahren immer wieder mit neuen Ideen und Lösungsansätzen zur Seite stand. An dieser Stelle danke ich auch Prof. Dr. Jochen Wambach für seine Unterstützung und für die spannende Zusammenarbeit, sowie Prof. Dr. Christian Fischer für die Übernahme des Zweitgutachtens dieser Arbeit. Für fruchtvolle Zusammenarbeit und viele hilfreiche Diskussionen danke ich außerdem Ralf-Arno Tripolt und Fabian Rennecke.

Dank gebührt auch Prof. Dr. Volker Koch für seine Gastfreundschaft und Nils Strodthoff für seine exzellente Betreuung während meines Aufenthalts am Berkeley National Laboratory.

Bei meinem Kollegen Lukas Holicki möchte ich mich für die schöne Zeit in Gießen und für viele spannende Diskussionen und Aktionen innerhalb sowie außerhalb der Uni bedanken.

Der größte Dank gebührt meinen Eltern und meiner Schwester, die immer an meiner Seite stehen und ohne die das Anfertigen dieser Arbeit undenkbar gewesen wäre. Hier ist außerdem meine geliebte Freundin Katja zu nennen, die mich in jeder Lebenslage unterstützt und mir unendlich viel Kraft gibt.

Erklärung zur Dissertation

Hiermit erkläre ich: Ich habe die vorgelegte Dissertation selbstständig und ohne unerlaubte fremde Hilfe und nur mit den Hilfen angefertigt, die ich in der Dissertation angegeben habe. Alle Textstellen, die wörtlich oder sinngemäß aus veröffentlichten Schriften entnommen sind, und alle Angaben, die auf mündlichen Auskünften beruhen, sind als solche kenntlich gemacht. Ich stimme einer evtl. Überprüfung meiner Dissertation durch eine Antiplagiat-Software zu. Bei den von mir durchgefürten und in der Dissertation erwähnten Untersuchungen habe ich die Grundsätze guter wissenschaftlicher Praxis, wie sie in der „Satzung der Justus-Liebig-Universität Gießen zur Sicherung guter wissenschaftlicher Praxis“ niedergelegt sind, eingehalten.

Ort, Datum

Christopher Jung